



Italian Chapter of the
European Society of Biomechanics
(ESB-ITA)

ESB-ITA 2015 Meeting

CNR IMATI, Milan – June 5, 2015

Organizing Committee: F Boschetti, M Conti, L Cristofolini, D Gallo, E Lanzarone

Book of Abstracts



PROGRAMMA DEL V MEETING DEL CAPITULO ITALIANO DELLA EUROPEAN SOCIETY OF BIOMECHANICS (ESB-ITA)

Milano, 5 Giugno 2015

9.00 – 9.45 *Workshop Mimics® Innovation Suite*
S Vanooteghem, Materialise Belgium

9.45 – 10.00 *Saluto e benvenuto*
Comitato Esecutivo ESB-ITA

Sessione I

10.00 – 10.15 *Can CT image deblurring improve strain and failure load predictions at the proximal femur?*
C Falcinelli, E Schileo, A Pakdel, C Whyne, F Taddei

10.15 – 10.30 *Decoupling the roles of stiffness and hydroxyapatite signalling in the osteo-differentiation of stem cells*
G Mattei, C Ferretti, M Mattioli-Belmonte, A Ahluwalia

10.30 – 10.45 *Evaluation of the accuracy and precision of a local DVC approach applied to natural and augmented vertebrae*
M Palanca, G Tozzi, V Danesi, E Dall'Ara, M Viceconti, L Cristofolini

10.45 – 11.00 *Fall risk monitoring: from laboratory to a portable device, influence of sampling frequency*
P Tamburini, R Stagni

11.00 – 11.15 *LIGHTarm: an exoskeleton for upper-limb neurorehabilitation*
A Scano, G Spagnuolo, M Caimmi, A Chiavenna, M Malosio, G Legnani, L Molinari Tosatti

11.15 – 11.45 Coffee Break

Sessione II

11.45 – 12.00 *Coronary bifurcation virtual bench testing: two patient-specific cases*
C Chiastra, W Wu, A Aleiou, H Otake, G Dubini, JF LaDisa Jr, F Migliavacca

12.00 – 12.15 *Patient-specific CFD of the aortic haemodynamics: Bringing cardiovascular virtual reality to clinical bedside practice*
L Antiga, F Auricchio, M Conti, A Lefieux, S Morganti, A Reali, RM Romanowski, F Secchi, C Trentin, S Trimarchi, A Veneziani

12.15 – 12.30 *The role of aortic shape and valve phenotype in the bicuspid aortopathy*
S Pasta, A Rinaudo, G Gentile, GM Raffa, A Luca, M Pilato, C Scardulla

12.30 – 12.45 *Shear-promoted drug encapsulation into red blood cells: a CFD model and μ -PIV analysis*
M Piergiovanni, G Casagrande, E Bianchi, ML Costantino

12.45 – 13.00 *Evaluation of fluid-dynamics and oxygen consumption in a porous scaffold stimulated by cyclic squeeze pressure*
M Ferroni, S Giusti, G Spatafora, F Boschetti, A Ahluwalia

13.00 – 14.45 Pranzo e sessione poster

- 14.45 – 15.00 *The Living Heart Project: A robust and integrative simulator for human heart function*
M Stevanella, Abaqus/Simulia Dassault Systèmes

Sessione III

- 15.00 – 15.15 *An automated adaptive bioreactor-based platform for culturing cardiac tissue models*
G Pisani, D Massai, A Rodriguez, G Cerino, R Galluzzi, G Falvo D'Urso Labate, C Bignardi, A Tonoli, A Audenino, A Marsano, U Morbiducci
- 15.15 – 15.30 *Multi-scale approach for the biomechanical characterization of human skin lesion*
E Cutrì, G Spatafora, G Franzetti, F Crippa, E Montin, L Mainardi, L Spadola, A Testori, G Pennati
- 15.30 – 15.45 *A refined yet simple shell finite element for soft biological tissues*
F Caselli, P Bisegna
- 15.45 – 16.00 *Fractional-order hereditariness of porcine hearth valves*
M Cammarata, AA Giglia, D Spadaro, M Zingales
- 16.00 – 16.15 Premiazioni, comunicazioni e saluti finali
- 16.15 – 17.00 Rinnovo Comitato Esecutivo ESB-ITA

Sessione Poster

- | | | |
|----|------------|--|
| 1 | Allegretti | <i>Measuring in vitro deformation of SFA stents with Digital Image Correlation</i> |
| 2 | Azizpour | <i>A dynamic model to compute torques generated by the shoulder and the elbow producing forces during hand cycling</i> |
| 3 | Bianchi | <i>CFD approach to study the efficiency of cell seeding on single scaffold fibres.</i> |
| 4 | Bianchini | <i>Evaluating uncertainty in finite element analysis via functional principal component analysis</i> |
| 5 | Corsini | <i>A morphometry-based lumped parameter model of the coronary circulation under resting and hyperemic conditions</i> |
| 6 | Danesi | <i>Digital Volume Correlation (DVC) to investigate the strain distribution and failure in prophylactic augmented vertebrae</i> |
| 7 | De Nisco | <i>A model-based study of the effect of intermittent pneumatic compression of limbs on the cardiovascular system</i> |
| 8 | Fedele | <i>A computational fluid dynamics study of the Carditis Multilayer Flow Modulator</i> |
| 9 | Ferraro | <i>Isogeometric-based tools for the evaluation of carotid artery stent performance</i> |
| 10 | La Barbera | <i>Preclinical evaluation of posterior spine stabilization devices: how close are we?</i> |
| 11 | Malosio | <i>A virtually-assisted variable-stiffness device for upper-limb rehabilitation</i> |
| 12 | Marino | <i>Homogenization methods for the multiscale constitutive description of soft connective tissues</i> |
| 13 | Mattei | <i>Smart enzymatically stiffenable hydrogels for 3D in-vitro models of tissue ageing and fibrosis</i> |
| 14 | Meoli | <i>Patient-specific multi-scale modelling of cardiac biomechanics in single ventricle circulation</i> |
| 15 | Ottardi | <i>A finite element study of the pedicle subtraction osteotomy (PSO)</i> |
| 16 | Pizzocaro | <i>A porous media foot model integrating gait analysis: proof of concept in a diabetic neuropathic subject</i> |
| 17 | Scano | <i>Kinect One-based biomechanical assessment of the upper limb during rehabilitation</i> |
| 18 | Serino | <i>Static mechanical characterization of cements for dental implantology through nanoindentation</i> |
| 19 | Spagnuolo | <i>LIGHTarm: a gravity-compensated exoskeleton for the upper-limb rehabilitation</i> |
| 20 | Tamburini | <i>Design with finite element method (FEM) of a modular small dimensions force platform for gait analysis</i> |
| 21 | Trentin | <i>From thoracic aorta segmentation to geometric parameters quantification: an automatic tool</i> |
| 22 | Zou | <i>In vitro tests of human femur before and after total hip arthroplasty with finite element analysis</i> |

Lista dei Contributi

Vanooteghem	Workshop Mimics® Innovation Suite
Allegretti <i>et al.</i>	Measuring in vitro deformation of SFA stents with Digital Image Correlation
Azizpour <i>et al.</i>	A dynamic model to compute torques generated by the shoulder and the elbow producing forces during hand cycling
Bianchi <i>et al.</i>	CFD approach to study the efficiency of cell seeding on single scaffold fibres
Bianchini <i>et al.</i>	Evaluating uncertainty in finite element analysis via functional principal component analysis
Caimmi <i>et al.</i>	The assessment of the upper-limb functionality: a method based on kinematic analysis
Camarata <i>et al.</i>	Fractional-order hereditariness of porcine heart valves
Caselli <i>et al.</i>	A refined yet simple shell finite element for soft biological tissues
Chiastra <i>et al.</i>	Coronary bifurcation virtual bench testing: two patient-specific cases
Corsini <i>et al.</i>	A morphometry-based lumped parameter model of the coronary circulation under resting and hyperemic conditions
Cutri <i>et al.</i>	Multi-scale approach for the biomechanical characterization of human skin lesion
Danesi <i>et al.</i>	Digital Volume Correlation (DVC) to investigate the strain distribution and failure in prophylactic augmented Vertebrae
De Nisco <i>et al.</i>	A model-based study of the effect of intermittent pneumatic compression of limbs on the cardiovascular system
Falcinelli <i>et al.</i>	Can CT image deblurring improve strain and failure load predictions at the proximal femur?
Fedele <i>et al.</i>	A computational fluid dynamics study of the Cardiac Multilayer Flow Modulator
Ferraro <i>et al.</i>	Isogeometric-based tools for the evaluation of carotid artery stent performance
Ferroni <i>et al.</i>	Evaluation of fluid-dynamics and oxygen consumption in a porous scaffold stimulated by cyclic squeeze pressure
La Barbera <i>et al.</i>	Preclinical evaluation of posterior spine stabilization devices: how close are we?
Malosio <i>et al.</i>	A virtually-assisted variable-stiffness device for upper-limb rehabilitation
Marino <i>et al.</i>	Homogenization methods for the multiscale constitutive description of soft connective tissues
Mattei <i>et al.</i>	Decoupling the roles of stiffness and hydroxyapatite signalling in the osteo-differentiation of stem cells
Mattei <i>et al.</i>	Smart enzymatically stiffenable hydrogels for 3D in-vitro models of tissue ageing and fibrosis
Meoli <i>et al.</i>	Patient-specific multi-scale modelling of cardiac biomechanics in single ventricle circulation
Ottardi <i>et al.</i>	A Finite Element Study of the pedicle subtraction osteotomy (PSO)
Palanca <i>et al.</i>	Evaluation of the accuracy and precision of a local DVC approach applied to natural and augmented vertebrae
Pasta <i>et al.</i>	The role of aortic shape and valve phenotype in the bicuspid aortopathy

Piergiovanni <i>et al.</i>	Shear-promoted drug encapsulation into red blood cells: a CFD model and μ -PIV analysis
Pisani <i>et al.</i>	An automated adaptive bioreactor – based platform for culturing cardiac tissue models
Pizzocaro <i>et al.</i>	A porous media foot model integrating gait analysis: proof of concept in a diabetic neuropathic subject
Romanowski <i>et al.</i>	Patient-specific CFD of the aortic haemodynamics: bringing cardiovascular virtual reality to clinical bedside practice
Scano <i>et al.</i>	LIGHTarm: an exoskeleton for upper-limb rehabilitation
Scano <i>et al.</i>	Kinect One-based biomechanical assessment of the upper limb during rehabilitation
Serino <i>et al.</i>	Static mechanical characterization of cements for dental implantology through nanoindentation
Spagnuolo <i>et al.</i>	LIGHTarm: a gravity-compensated exoskeleton for the upper-limb rehabilitation
Tamburini <i>et al.</i>	Design with finite element method (FEM) of a modular small dimensions force platform for gait analysis
Tamburini <i>et al.</i>	Fall risk monitoring: from laboratory to a portable device, influence of sampling frequency
Trentin <i>et al.</i>	From thoracic aorta segmentation to geometric parameters quantification: an automatic tool
Zou <i>et al.</i>	In vitro tests of human femur before and after total hip arthroplasty with finite element analysis

Milan, June 5th 2015

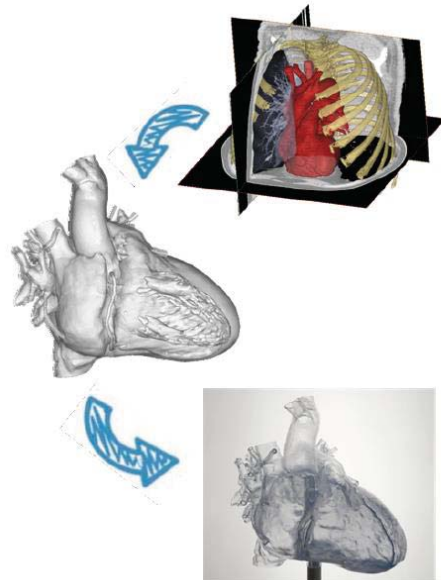
Workshop Mimics® Innovation Suite

Simon Vanooteghem, Materialise Belgium - simon.vanooteghem@materialise.be

The presentation of 3 case studies, each focused on a different biomedical field, gives an indication of how the Mimics Innovation Suite empowers biomedical professionals to improve quality of life through engineering on anatomy.

The first case study shows how a surgical team of the University Hospital of Maastricht used the Mimics Innovation Suite to design a patient-specific cranial implant that restored the symmetry of the forehead, covered the cranial defect, protected the brain and spared the patient unnecessary discomfort.

In a second case study, researchers from Ghent University compared corrosion casts of the aorta of sacrificed mice to 3D models obtained from live animals. In the future, these 3D models will allow follow-up studies to examine the process of aneurysm formation, ultimately benefitting clinical research.



In the final case study, researchers from Stellenbosch University looked into the possibility of creating custom knee implants. Every year more than 1 million arthritic patients worldwide undergo knee replacement surgery. Although this is one of the most complex joints, conventional knee implants only exist in standard sizes and shapes predetermined by their manufacturers. The wide range of tools in the Mimics Innovation Suite proved to be a key technology for the diverse aspects in this research.

For suggestions on the topic of the workshop and for specific research questions, do not hesitate in contacting the speaker at: simon.vanooteghem@materialise.be

Measuring in vitro deformation of SFA stents with Digital Image Correlation

D. Allegretti¹, K. Genovese², L. Petrini³, F. Migliavacca¹, G. Pennati¹

¹ LaBS, Dept. of Chemistry, Materials and Chemical Engineering 'Giulio Natta', Politecnico di Milano, Italy

² School of Engineering, University of Basilicata, Potenza, ITALY

³ Department of Civil and Environmental Engineering, Politecnico di Milano, Italy

Abstract — Nitinol peripheral stents are commonly used in the treatment of atherosclerosis in superficial femoral arteries. However, their success is still undermined by long-term fatigue failure due to the arterial deformations transmitted to the stent. In this paper we present an experimental investigation aimed to perform 360-deg in vitro measurement of shape and deformation of SFA stents with 3D digital image correlation (DIC). A custom constant-magnification lens system coupled with a 4° wedge prism allowed to obtain the two angled views needed for subsequent 3D reconstruction of multiple adjacent portions of a 8mm stent. The obtained 3D data patches were then merged in a common reference system through an optimization-based procedure. Preliminary results of shape and strain maps obtained for a stent under compressive load are presented to illustrate the metrological capabilities of the developed system.

Keywords—SFA stents, 3D Digital Image Correlation, shape and strain measurement.

I. INTRODUCTION

PERIPHERAL artery diseases (PAD) are commonly treated by stenting procedures. The particular biomechanical environment of lower limbs, characterized by hip and knee joint movements associated with patient's daily activities, exposes the superficial femoral artery, and therefore the implanted stents, to large and cyclic deformations [1]. Nickel-Titanium (NiTi) alloy stents are preferred for the treatment of PAD, because, thanks to the pseudo-elastic property, they are able to recover the original shape and the blood flow perfusion at every cycle [2]; however, their success is still undermined by long-term fatigue failure [3].

Nowadays finite element (FE) analyses are often used combined with or on behalf of in vitro tests for fatigue assessment [4]. The strong non-linearity of material behaviour suggests performing preliminary validation of the numerical stent model through comparison with experimental tests. Measuring deformations in a stent during in vitro test is a demanding problem, and the ability of the FE model to foresee the right strain distribution induced by different loading conditions has to be checked, considering that for NiTi a strain-based approach is used for fatigue analyses.

Digital Image Correlation [5] is a widespread technique for high resolution shape and deformation measurement that has been recently applied to investigate the mechanical behaviour of shape memory alloys (SMA) tubes [6]. Extending the application of this technique to the measurement of the deformation of a stent at the strut level poses a significant challenge due to the small scale of the area of interest that prevents from reaching a sufficient spatial resolution with

common video-optical systems. This study sought to develop a novel optical set-up for high magnification DIC measurement of stent deformation in vitro. Preliminary results for a portion of a SFA stent under compression are reported here to illustrate the potential metrological capabilities of the developed system.

II. MATERIALS AND METHODS

Figure 1 shows a picture of the developed optical set-up. A custom telecentric 2X lens magnification system [7] allowed to minimize the strain errors due to the change in magnification over the depth of field. A 4° wedge prism mounted on a rotation stage allowed to obtain multiple angled views of the sample for subsequent 3D reconstruction on the basis of Computer Vision principles [5]. A test device was designed and assembled using PMMA custom parts, a micro-translational mount and a goniometer to load a stent sample (8 mm diameter and 20 cm height) in axial tension, compression and torsion. The loading frame was then mounted on a four-axes stage allowing its precise positioning with respect to the imaging system. Due to the high magnification of the imaging system, in fact, only a portion of the stent is visible from the camera and the full surface of the sample can be spanned only by properly repositioning the stent (through stepwise rotations around the z-axis and translations in the z-direction) with respect to the fixed imaging system. Prior calibration testing allowed to choose the optimal magnification factor to obtain a sufficient spatial resolution (for high accuracy DIC measurement, [5]) at a ~3 mm depth of focus at constant magnification. Displacement fields corresponding to a set of pure translations were used to check the effect of lens aberration and to individuate a central region of the image where corresponding errors can be neglected.

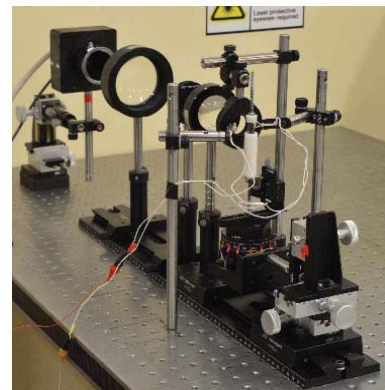


Fig.1. Picture of the experimental set-up.

At each step, a portion of about $3 \times 3 \text{ mm}^2$ can be reconstructed with 3D DIC. Fifteen positions in the circumferential direction and four positions in the axial direction were needed to cover the entire 360-deg surface of the stent before and after deformation. The set of 3D patches of data points so obtained were then merged in a common reference system by using an optimization-based procedure coded in Matlab. In particular, for each couple of 3D data points, the optimization algorithm sought the coordinate transformation (i.e. the components of the rotation matrix and translation vector) that minimized the distance between corresponding sets of homologous points in the two reconstructed patches. Figure 2 shows a reconstructed portion (made up of six patches) of the tested stent sample under an axial compression of -0.5 mm. By tracking the speckle pattern applied on the sample surface before and after deformation, it was possible to calculate the strain map of the stent at the strut level. If a triangular mesh is used to discretize the overall geometry, the components $E_{\xi\xi}$, $E_{\eta\eta}$ and $E_{\xi\eta}$ of the surface Green strain tensor \mathbf{E} can be obtained easily by assuming a homogenous strain field within each triangular domain of the mesh with respect to n local $\xi\eta$ coordinate systems by following the procedure described in detail elsewhere [8]. In particular, by solving the eigenvalue problem for \mathbf{E} , it is possible to compute the principal strains E_1 , E_2 'pointwise' over the entire surface of the sample. This allows one to capture the inhomogeneous deformations with a spatial density consistent with the resolution of the DIC measurement.

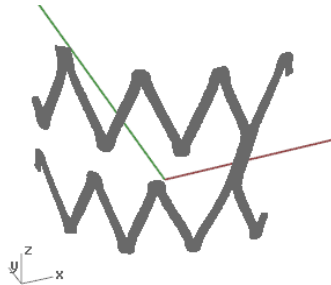


Fig.2. 3D reconstruction of a portion of a stent under an axial displacement of -0.5 mm.

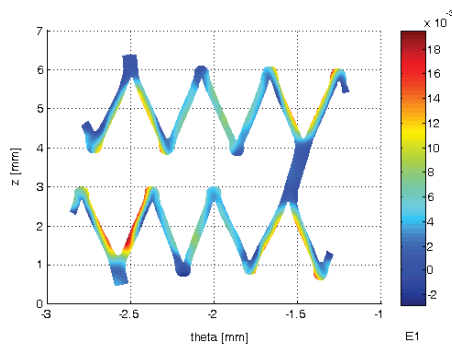


Fig.3. Experimental distribution for the first principal

Green strain for the stent portion of Figure 2.

III. CONCLUSION

The main objective of this experimental work was to verify the feasibility of 3D DIC measurement at small scale with a novel developed custom optical set-up consisting in a lens magnifying system coupled with a wedge prism. The imaging and data analysis procedure here developed allowed the reconstruction of a wide portion of a SFA stent before and after in vitro compression load. DIC allowed also to track deformation and to obtain the full-surface strain map of the investigated portion of the sample. The system is designed to perform full 360-deg measurement on SFA stents under tensile, compressive and torsion loads (and any combination of them). Although only results of the compression on a limited portion of the sample have been presented here and further calibration tests should be conducted to assess the accuracy and robustness of the experimental procedure, this approach promises to help in gaining a better insight into the deformation and failure behaviour of SFA stents.

REFERENCES

- [1] C.P. Cheng, N.M. Wilson, R.L. Hallett, R.J. Herfkens, C.A. Taylor. In Vivo MR Angiographic Quantification of Axial and Twisting Deformations of the Superficial Femoral Artery Resulting from Maximum Hip and Knee Flexion. *J. Vasc. Interv. Radiol.* 2006, 17, 979–987.
- [2] Y. Nakagawa, J. Yajima, Y. Oikawa, K. Ogasawara, H. Kirigaya, K. Nagashima, R. Funada, S. Matsuno, T. Inaba, M. Nakamura, H. Sawada, T. Aizawa. Clinical outcomes after percutaneous peripheral intervention for chronic total occlusion of superficial femoral arteries: comparison between self-expandable nitinol stent and stainless steel stent. *J. Cardiol* 2009, 53, 417-11 421.
- [3] D. Scheinert, S. Scheinert, J. Sax, C. Piorkowski, S. Bräunlich, M. Ulrich, G. Biamino, A. Schmidt. Prevalence and clinical impact of stent fracture after femoro-popliteal stenting. *J Am Coll Cardiol* 2005, 45, 312-315.
- [4] A. Meoli, E. Dordoni, L. Petrini, F. Migliavacca, G. Dubini, G. Pennati. Computational study of axial fatigue for peripheral Nitinol stents. *J. Of Materi Eng and Perform* 2014; 23(7):2606-2613.
- [5] M.A. Sutton, J.-J. Ortu, H. Schreier. Image correlation for shape, motion and deformation measurements. 2009 New York, NY: Springer.
- [6] B. Reedlunn, C.B. Churchill, E.E. Nelson, J.A. Shaw, S. H. Daly, Tension, compression, and bending of superelastic shape memory alloy tubes. *Journal of the Mechanics and Physics of Solids*, 36, p. 506-537, 1988.
- [7] M. Watanabe, S.K. Nayar, Telecentric optics for computational vision, ECCV '96, 4th European Conference on Computer Vision Cambridge, UK, April 15–18, 1996.
- [8] K. Genovese. A video-optical system for time-resolved whole-body measurement on vascular segments. *Optics and Lasers in Engineering*, vol. 47, p. 995-1008, 2009.

A Dynamic Model to Compute Torques Generated by the Shoulder and the Elbow Producing Forces During Handcycling

G. Azizpour¹, A. ousdad¹, M. Lancini¹, G. Incerti¹, and G. Legniani¹
¹ Dept. of Mechanical and Industrial Engineering University of Brescia, Brescia, Italy.

Abstract—A lot of effort has been dedicated to develop exercise equipment for the people who struggle with upper limb disabilities. The handbike is an upper body-powered device used for sports and rehabilitation purposes. The advantages include improving patients' physical activities and fitness level, as well as promoting an active lifestyle after rehabilitation duration.

In this research the torques in shoulder and elbow's joints have been determined during handbike motion from dynamic output and kinematics information. Therefore, a 2D model was presented. Data have been collected based on the output of experimental results obtained by sensors inserted on the handgrips and marker coordinates acquired by vision system. Finally, the force manipulability ellipse during handcycling has been obtained for some specific positions of the crank.

Keywords— Handbike, Dynamic Model, Joint Torques.

I. INTRODUCTION

Handbikes are three wheel vehicles used for transportation and recreation, but they are also widely used in rehabilitation programs for people with reduced mobility, and in sport fields for disabled people.

In the last decade, researches have showed interest in different aspects of synchronous handcycling. Literature analyzes physiological responses with oxygen uptake, ventilation and respiratory rate to identify the effects of cadency and work rate [1], [2]. Furthermore, some studies performed biomechanical and force analyses, which were conducted to identify two main efficiency indices. The first one is the fraction of effective force (FEF) [1], [3], associated with the effectiveness of the force application and the second one is the postural force production index (PFPI) [4], which evaluates the force generation capacity in all directions. However, these indices do not take into account gravity, inertia and the Coriolis effects, thus presenting a limitation in the efficiency evaluation. The aim of this study is to present a dynamic model that considers contributions of gravity, inertia and Coriolis effects in order to associate the forces measured on handles to the corresponding shoulder and elbow torques, and also determine the force manipulability ellipse during handcycling. This allows correction of definition of the mentioned indices to give them more relevance.

II. METHODS

In this study, a planar model of the upper-limb has been developed [5], considering one rotation for the shoulder and the elbow respectively, whilst the wrist joint is considered fixed to the handle (figure1).

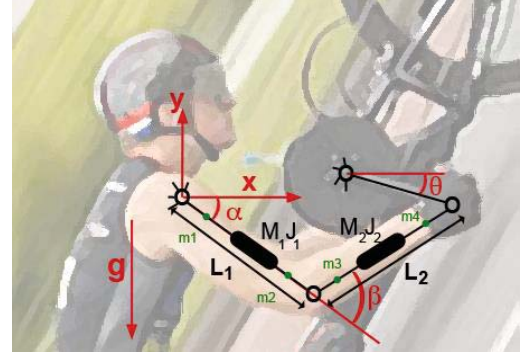


Figure 1. Details of the Planar Model of the Upper-Limb

The dynamic model describes the inertia, gravity and the Coriolis effects with the product of a matrix, which is composed of the kinematics terms, by a vector of dynamic parameters of arm and forearm (eq.1).

$$F_q = M_s \ddot{Q} + C \dot{Q} + G + J^T \cdot F_{se} = B \cdot P + J^T \cdot F_{se} \quad (\text{eq.1})$$

F_q : The joints torques.

M_s : The inertial matrix.

\ddot{Q}, \dot{Q} : The angular acceleration and angular velocity of the joints.

C : The Coriolis effects matrix.

G : The gravity matrix.

J^T : The transpose matrix of the Jacobian.

F_{se} : The external forces.

B : The kinematics term matrix.

P : the dynamic parameters matrix.

The algorithm to assess the value of torques is based on a two step procedure, and is described below:

The first step is to use the athlete height and weight, and the anthropometric data, which have been found in literature, in order to compute the length of arm and forearm, the center of masses and inertia moments.

These data were used to characterize the handcycling planar model. The mechanical behavior of the model is then simulated, assuming no torques applied to the joints and using a constant velocity in the crank. From results of kinematics and kinetics analysis, the dynamic parameters vector (P) is then estimated (eq.2).

$$P = -(B^T \cdot B)^{-1} \cdot B^T \cdot J^T \cdot F_{se} \quad (\text{eq.2})$$

The second step is to use the calculated dynamic parameter P so that the joint torque has been assessed.

On the other hand, wheelchair dependent subjects,

experienced in handcycling, are asked to perform the tests on an adjustable recumbent sport Handbike which is converted into an ergometer, designed and built by the university of Brescia. A control system is integrated into the device that guarantees a constant output power. It is also, equipped by two bi-axial load cells mounted on handles to measure radial and tangential components of the applied force and an encoder to measure the angular position of the crankshaft in order to relate the measured force to the crank position (figure2). During the test the subjects are asked to keep their shoulder and elbow joints passive and the movement is produced by external rotating of the crank. Sequentially, the dynamic parameters of the upper-limb is calculated using coordinates of the elbow and shoulder acquired by a vision system, and exerted forces on the handles measured by load cells during the handcycling.

Finally, based on this model and applying the calculated dynamic parameter, it is possible to estimate the torques exerted by the shoulder and the elbow, by using the coordinates of the markers and the forces applied on handles.

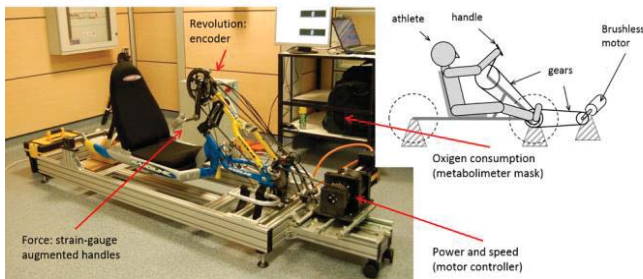


Figure 2. Details of the Ergometer Used for the Tests

III. RESULTS

The posture of the arms, the crank position and the force at the handle are measured with respect to the time, while velocities and accelerations are assessed by numerical differentiation. Thanks to simulation of the dynamic model based on experimental data it was possible to compute torques generated by the human joints. Applying the dynamic parameters vector obtained based on (eq2), the amounts of shoulder and elbow joints torques are calculated and the obtained results are shown in figure 3, which confirmed that the proposed model can estimate the torques with good accuracy.

Then, in order to determine the force manipulability ellipse, maximum joint torques were assessed by locking the crank in different angular positions and asking to the subjects to exert their maximum possible force into the handle.

At the end, the definitions of the mentioned indices (FEF and PFPI) were modified by including the effects of dynamic contributions, and force weight. The Fraction of Effective Torque (FET) index assesses the efficiency of torque generation in joints, and the Inertial and Postural Force Production (IPFP) index, evaluates the effect of inertia and posture on the generation of force.

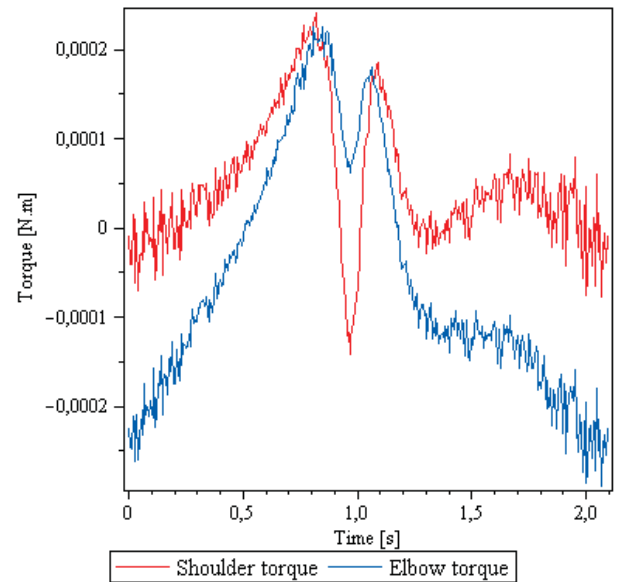


Figure 3. The Shoulder and Elbow Torques

IV. CONCLUSION

This study develops an analytic method to compute joints torques generated during handcycling. The method takes into account inertia, gravity and the Coriolis effects. Furthermore, it has identified two new indices that could be used to describe and understand the performance of handbike athletes.

REFERENCES

- [1] Powers S.K., Beadle R.E. and Mangum M., *Exercise efficiency during arm ergometry: effects of speed and work rate*, 1984. W.-K. Chen, *Linear Networks and Systems* (Book style). Belmont, CA: Wadsworth, 1993, pp. 123–135.
- [2] Price, M.J., Collins, L., Smith, P.M., Goss-Sampson, M., *The effects of cadence and power output upon physiological and biomechanical responses to incremental arm-crank ergometry*, 2007.
- [3] Van Drongelen S., Arnet U., Van Der Woude L.H.V., Veeger H.E.J., *Propulsion effectiveness of synchronous handcycling*, 2010.
- [4] Jacquier-Bret J., Faupin A., Rezzoug N., Gorce P.A., *New postural force production index to assess propulsion effectiveness during handcycling*, 2013.N.
- [5] Arnaud Faupin, Philippe Groce, *Effects of crank adjustment on handbike propulsion: a kinematic approach*, 2008.

CFD approach to study the efficiency of cell seeding on single scaffold fibres.

E. Bianchi¹, C. Arrigoni², C. Turrisi¹, M. Moretti³, S. Mantero¹, G. Dubini¹

¹Department of Chemistry, Materials, and Chemical Engineering "Giulio Natta", Politecnico di Milano, Milan, Italy

²Cell and Tissue Engineering Laboratory, Gruppo Ospedaliero San Donato Foundation, Milan, Italy

³Cell and Tissue Engineering Laboratory, IRCCS Galeazzi Orthopaedic Institute, Milan, Italy

Abstract—Cell seeding in a scaffold is one of the key steps in tissue engineering. By means of dynamic cell seeding cells are loaded on the scaffold by a perfusion flow delivering the cells inside the 3D matrix more homogeneously than how it is performed by means of a static procedure. The dynamic seeding on fibrous scaffolds is the most promising procedure: microstructure of 3D fibrous scaffolds, made up by layers of fibres is more homogeneous and reproducible than a random porous matrix. However fluid dynamic settings of the flow and geometrical features of fibres (shape/layout) can definitely affect the efficiency of cell seeding.

In this study CFD simulations have been performed on cylindrical based single and compound fibres, in order to deduce configurations of fibrous scaffold suitable to dynamic cell seeding in terms of stagnation/recirculation area and relative wall shear stress.

Keywords—Tissue engineering, dynamic seeding, CFD, fibrous scaffolds.

I. INTRODUCTION

THE aim of tissue engineering is the use of cells to develop, thanks to three-dimensional supports (scaffold), biological substitutes able to reactivate the functions of the damaged tissues.

A traditional approach to load cell into the scaffold is a static seeding, by the deposition of a drop of cells solution on the top surface of the 3D support, free to penetrate into the matrix led by gravity force only. Efficiency of static seeding is low, inhomogeneous, characterized by a weak adhesion due to the creation of cell clusters only partially anchored to the scaffold surface [1]. In order to improve the seeding efficiency a dynamic approach can be chosen, by means of fluid flow perfusion that carry the cells through the scaffold itself.

Porous scaffolds show a random distribution of pores, hard to be controlled. 3D fibrous scaffold, made up by layers of fibres, variously oriented in the space, are instead well-organized and reproducible. Dynamic cell seeding experiments on 3D fibrous scaffolds made of polylactic acid and produced by a 3D printing [2], have discovered a low efficiency, mainly due to the circular shape of the fibres: fluid streamlines go around them and cells have got no possibility of attachment. Unless external factors lead cells out of the streamlines, they follow the trajectories tangent to the surfaces [3] and seeding can not be efficiently performed. The CFD has been used by e.g. Olivares et al, 2012 [4] to study the dynamic cell seeding on a complete porous scaffold but efficiency was not related to the differences in the local microstructures of the porous matrix. The aim of this study is the research of patterns of

fibres fluid -dynamically suitable to create areas which the cells can be trapped: this would increase the probability of attachment to the surfaces.

II. MATERIALS AND METHODS

CFD simulations have been carried out by Comsol Multiphysics 4.2a.

Five different 2D units, representing cylindrical based compound fibres, perpendicular to the direction of flow have been considered [Fig. 1]

- 1: two cylindrical fibres (\varnothing 100 μ m, distance 10 μ m)
- 2: three cylindrical fibres (\varnothing 50 μ m, distance 10 μ m)
- 3: one main cylindrical fibre (\varnothing 50 μ m) and three lateral cylindrical fibres (\varnothing 100 μ m)
- 4: one main cylindrical fibre (\varnothing 100 μ m) and four lateral cylindrical fibres (\varnothing 500 μ m), 90° position
- 5: one main cylindrical fibre (\varnothing 100 μ m) and four lateral cylindrical fibres (\varnothing 500 μ m), 60° e 120° position

1 and 2 are designed to create a larger surface perpendicular to the flow: distance among the fibres do not break the flow but can act like a sieve for cells.

3, 4 and 5 are designed to create concavities where the fluid can slow and stagnate. Flow (water $\mu = 0,001$ [Pa·s], $\rho = 1001$ [kg/m³] through the scaffold with an average velocity $v = 75$ [μ m/s] (Laminar flow – $Re \ll 1$)

At the end it has been measured the ratio between the stagnation area (area around the fibre where the velocity is lower than an arbitrary value chose as 1.5×10^{-5} m/s and the 10% of the average velocity for each simulation) and the perimeter of the fibre. It has been shown the presence of small loops in the stagnation area, especially around fibres that creates concavities among the lateral fibres. The distribution of wall shear stress on the fibre surface has been evaluated to compare the detaching forces acting on cells, in the different geometrical configurations.



Fig.1 Sketch of the five different compound fibres

III. RESULTS

Concerning the “available surface” ($A/2p$ - StagnationArea/perimeter ratio) the fibres 2, 3 and 4 are those forming wider stagnation areas around them. The stagnation

area is mainly localized in the concavities but also upstream and downstream the fibres. Structures showing “concavities”, fibres 3-4-5, are subjected to form loops close to the walls and so they present the highest probability to trap cells and let them adhere. The same fibres show wall shear stress relatively low, low speed variations near the fibres. Anyway it has not been possible to calculate the direction and versus of the stresses which might prevent the arrival of nutritive substances and the adhesion of the cells themselves.

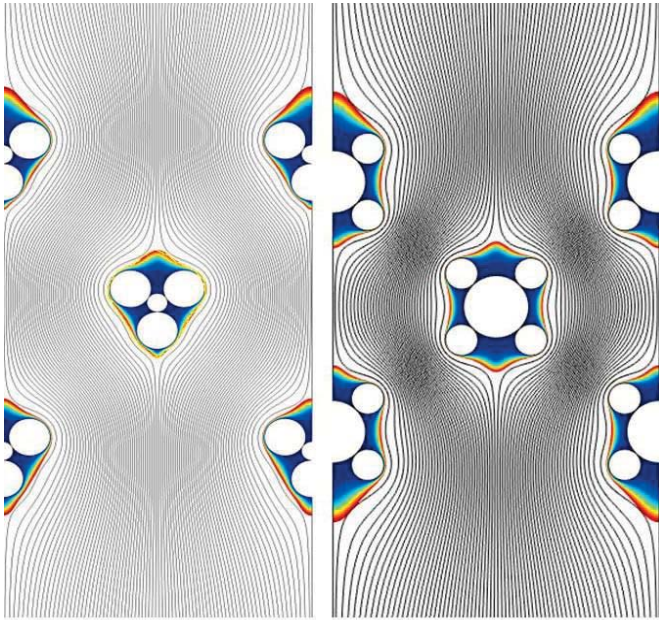


Fig.2 Stagnation area all around two different fibre models, 3 and 4. Blue; minimum value (zero velocity), Red: the maximum arbitrary velocity value.

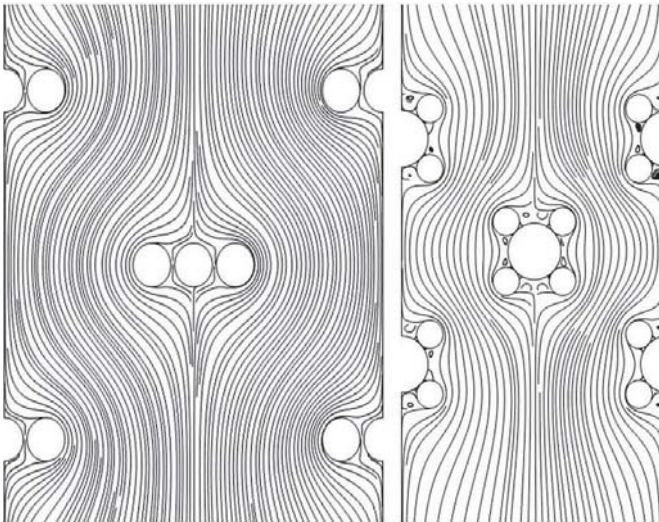


Fig.3 Streamlines of flow: loops around the fibres 4 but not around fibre 2. Concerning the geometry 1 and 2, streamlines pass around the obstacle without recirculation.

As shown in Fig.4 more spaced are the fibres, wider is the available surface around the fibres. Spaced fibres interact less one to each other in terms effect on the of flow. Increasing the distance among fibres means decreasing the total number of fibres in the volume of the scaffold: that means decreasing the seeding efficiency by decreasing the amount of surface available to the adhesion. However the values of “available

surface” have only a comparative role among the tested fibres.

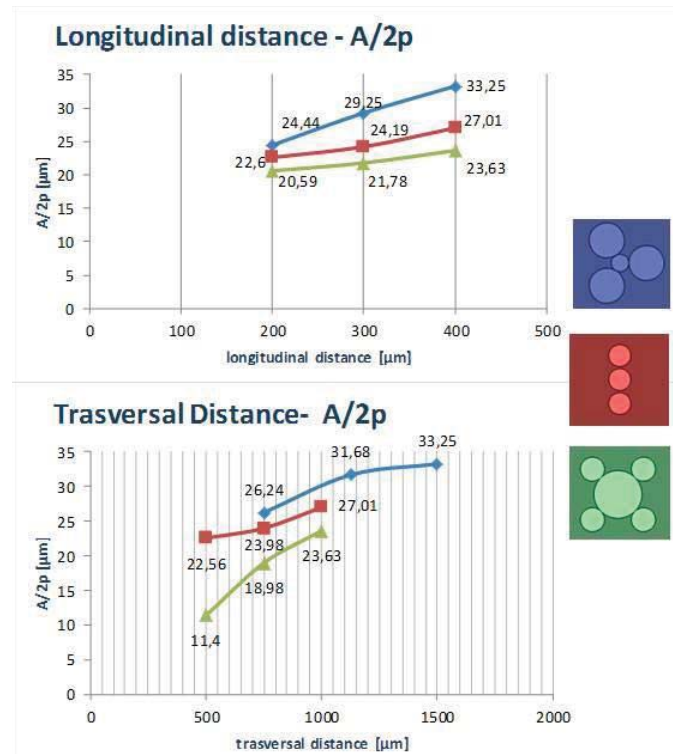


Fig.4 Relation between longitudinal and trasversal distance between fibres and $A/2p$ for fibres 2,3 and 4. In the plot the values of $A/2p$.

CONCLUSIONS

The introduction of compound fibres seems to be advantageous versus the single cylindrical fibre: the creation of closed loops in the concavities could improve the efficiency of cell seeding. Anyway, to prove the validity of this statement experimental test on fibres prototypes have to be performed.

CFD simulations at single fibre level, aiming at improving cell seeding tuning the geometry of the single fibres, proved to give advantage to the optimization of the entire and complex cell seeding process.

ACKNOWLEDGEMENT

Thanks to Daiana Mazzola, Francesca Salmistraro, Laura Sordini for the contribution to simulations and the prolific discussion.

REFERENCES

- [1] Jose F. Alvarez-Barreto, Shawna M. Linehan, Robert L. Shambaugh, and Vassilios I. Sikavitsas I, “Flow perfusion improves seeding of tissue engineering scaffolds with different architectures”, *Annals of Biomedical Engineering*, Volume 35, Number 3, pages 429–442, March 2007
- [2] M. Sciola “Sviluppo e validazione sperimentale di un modello computazionale per lo studio dell’influenza dei parametri geometrici dello scaffold nei processi di semina dinamica nell’ingegneria dei tessuti” Tesi di Laurea – Ottobre 2013 – Politecnico di Milano
- [3] James P. Smith Alexander C. Barbati, Steven M. Santana, Jason P. Gleghorn, Brian J. Kirby. “Microfluidic transport in microdevices for rare cell capture”, *Electrophoresis* 2012, pages 3133–3142, 2012
- [4] Andy L. Olivares, Damien Lacroix., “Simulation of cell seeding within a three-dimensional porous scaffold: affluid-particle analysis”, *Tissue Engineering, Part C* Volume 18, Number 8, 2012.

Evaluating uncertainty in finite element analysis via functional principal component analysis

I. Bianchini¹, R. Argiento², F. Auricchio³, and E. Lanzarone²

¹ Politecnico di Milano, Dept. of Mathematics, Milan, Italy

² CNR-IMATI, Milan, Italy

³ University of Pavia, Dept. of Civil Engineering and Architecture, Pavia, Italy

Abstract— When approaching a biomechanical system with the Finite Element (FE) analysis, its complexity points out the difficulty in performing accurate and standardized experimental investigations on the system, henceforth, resulting in difficulties not only in creating valid models but also in experimentally measuring the model parameters. As a consequence, each reliable analysis should approach the problem by considering the non-negligible fluctuations of model features and parameters, thus pursuing uncertainty quantification. In this paper, we propose a novel non-intrusive method to perform efficient uncertainty quantification for FE analysis, based on Monte Carlo sampling. Indeed, we collect a large number of samples of some random quantities of interest and, in order to reduce the large computational effort required by a Monte Carlo approach, we construct a reduced space spanned by the functional principal components, and we solve the FE problem in this subspace of lower dimensions. Numerical results on several test cases show the efficiency of the method and its applicability also in cases affected by high variability. Hence, the proposed method can be an efficient tool to support FE analysis in biomechanics.

Keywords— Finite Elements Analysis, Stochastic Input Parameters, Uncertainty Quantification, Reduced Basis.

I. INTRODUCTION

The complexity of several phenomena related to human physiology and biomechanical systems and the difficulties in measuring the system parameters point out the need for considering the variability of model features and parameters while performing Finite Element (FE) analyses. Mathematically, the uncertainty can be expressed by characterizing the random input parameters through a probabilistic distribution, which embodies all information available on the phenomenon. In this perspective, our aim is to propose an effective numerical method for estimating the probability density functions of the output quantities of interest in a FE simulation. Two main approaches exist in the literature to include randomness in a FE computational scheme, namely *intrusive* and *non-intrusive* techniques [1]. Intrusive approaches directly include randomness in the FE formulation, but they require rewriting the existing codes. On the contrary, non-intrusive methods are desirable from an applicative point of view since they allow using commercial deterministic codes as black boxes.

For these reasons, we work in the non-intrusive framework, and we propose an innovative approach with a reduced basis adaptively constructed, which is orthogonal and data-driven. The statistical technique at the basis of our approach, namely the Functional Principal Component Analysis (FPCA), is a quite recent methodology that results very appropriate in this

context [2].

The problem addressed is the following elastic problem:

$$\begin{cases} \operatorname{div} [\mathbb{K} \boldsymbol{\varepsilon}(\mathbf{u})] + \mathbf{f} = 0 & \text{in } \Omega \\ \mathbb{K} \boldsymbol{\varepsilon}(\mathbf{u}) \cdot \mathbf{n} = \mathbf{g}_d & \text{on } \partial_N \Omega \\ \mathbf{u} = \mathbf{u}_d & \text{on } \partial_D \Omega \end{cases}$$

where \mathbf{u} is the unknown displacement field compute, $\boldsymbol{\varepsilon}$ is the strain tensor, \mathbb{K} is the Hooke tensor, and \mathbf{f} , \mathbf{g}_d and \mathbf{u}_d are the boundary conditions on the domain Ω . The random input quantities associated to the problem are included in vector $\boldsymbol{\theta}$.

II. PROPOSED METHOD

Our procedure is based on that described in [3], where the authors create a reduced basis spanned by a number of solutions corresponding to different values of the random input quantities. The following solutions, related to other values of $\boldsymbol{\theta}$, are computed in the space generated by this basis. Moreover, the iterative procedure is also able to enrich the basis if a certain criterion on the error is not satisfied. Differently from [3], we propose a method which exploits FPCA (see [2] for a detailed review on this topic) to guarantee the orthogonality of the basis and improve efficiency. Our procedure is divided into two steps: a *training phase* and a *simulation and update phase*, as briefly described below.

A. Training phase

Sample N values $\{\boldsymbol{\theta}_i\}$ ($i=1, \dots, N$) of the random input vector according to its probabilistic law. Then, solve the N problems with the complete FE method, one for each sampled $\boldsymbol{\theta}_i$, and define the set of the obtained solutions $\mathbf{U}=\{\mathbf{u}_i\}$. Create the reduced basis \mathbf{B} of \mathbf{U} formed by the first k eigenfunctions obtained through FPCA. k can be chosen according to different criteria; the most popular is the *scree plot* (see, for instance, [4]). Note that the eigenfunctions are orthonormal.

B. Simulation and update phase

Perform $M \gg N$ new Monte Carlo iterations solving the problem not in the FE space but in the reduced space spanned by \mathbf{B} . This reduced space has a small dimension k , and the solution is therefore much less computationally demanding. At each iteration, in order to assess the goodness of the result in the reduced space, the error between the reduced solution and the complete one (the one we would obtain using the FE method) is evaluated. We underline that the error between the solutions is derived without computing the complete solution. If the error is lower than a tolerance value, the reduced

solution is added to the set of the solutions; otherwise, the basis is recomputed including the new complete solution. At the end of the process we obtain $N+M$ solutions $\mathbf{u}(\theta_i)$, i.e., a Monte Carlo sample of the random output. Finally, summary quantities of interest, e.g., the maximum and the average displacement along a given direction, can be easily computed from the solutions $\mathbf{u}(\theta_i)$, and their histograms can be plotted as an estimation of the probability distributions.

III. NUMERICAL TESTS

We apply the proposed method on some test cases, considering a rectangular domain of dimensions 5 and 1, respectively, with homogeneous body force \mathbf{f} and Dirichlet boundary conditions on one side. The only random parameter is the Young modulus E , while the Poisson parameter is constant. Here, we show the results for the case in which the field $E(x,y)$ presents two peaks with random locations (variances of both positions are 0.05 and 0.005 along the x and y axis, respectively).

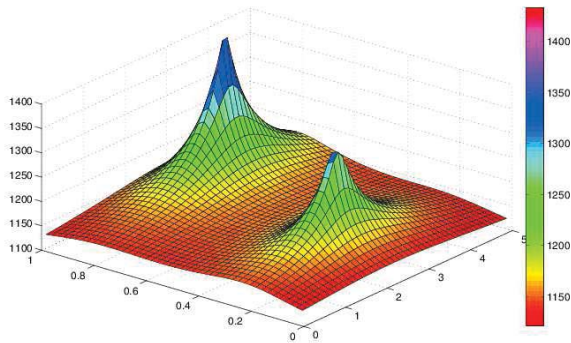


Fig.1: Example of realization of the elastic field.

We run the simulation with $N=100$, $M=3000$, and a tolerance value equal to 10^{-3} . We found that the algorithm only needs a basis of dimension 14 to describe the data, even if the uncertainty of the positions of the peaks is quite high. Thus, from a computational point of view, the method allows an efficient implementation of Monte Carlo sampling in a non-intrusive framework, since the computational effort is highly reduced with the above mentioned dimension. The resulting distribution of the average displacement along the horizontal direction is shown in Fig.2. Since the difference between the reduced solution and the complete one is checked at each iteration, the histogram in the figure is almost identical to the one we would obtain with a standard Monte Carlo approach on the complete FE problem.

Fig. 3 shows the first element of the basis \mathbf{B} , i.e., the first eigenfunctions along the horizontal direction and the vertical directions, i.e., the most important variations present in the computed solution.

IV. CONCLUSIONS

We propose a new method to account for uncertainty in FE analyses affected by randomness in model parameters, which is the typical case of biomechanical investigations. It is a non-intrusive method based on a Monte Carlo sampling coupled with a reduced basis approach, where the basis is created

according to the FPCA. Our proposal turned out to be a valid alternative to other non-intrusive methods present in the literature. We tested its behaviour in several bidimensional tests, obtaining satisfying results and low computational times. The procedure is general and can be applied easily in a wide variety of situations, and in particular in biological applications where a great uncertainty often affects the measurements of the input parameters. Our next step will be the application on real biomechanical cases, e.g., aortic deformation and bone compression.

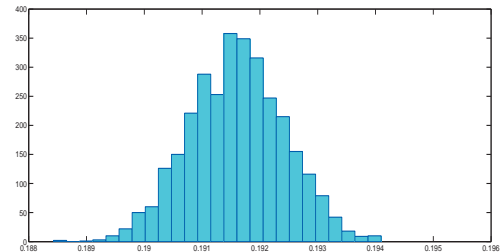


Fig. 2: Average displacement along the horizontal direction.

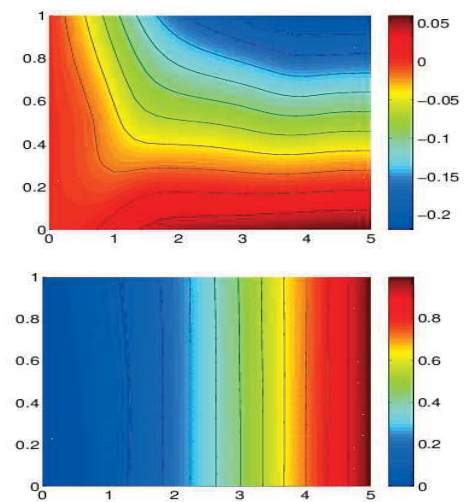


Fig.3: The first component of the basis.

ACKNOWLEDGEMENT

This work has been supported by Italian CNR and MIUR organizations through the Flagship Project *Factory of the Future – Fab@Hospital*.

REFERENCES

- [1] G. Schueller, “Developments in stochastic structural mechanics” *Archive of Applied Mathematics*, 2006, 75: 755-773.
- [2] J.O. Ramsay and B.W. Silverman, “Functional data analysis,” 2nd Ed., Springer Series in Statistics, 2005.
- [3] E. Florentin and P. Diez, “Adaptive reduced basis strategy based on goal oriented error assessment for stochastic problems” *Computer Methods in Applied Mechanics and Engineering*, 2012, 225-8: 116-27.
- [4] A. Nouy, “A generalized spectral decomposition technique to solve a class of linear stochastic partial differential equations” *Computer Methods in Applied Mechanics and Engineering*, 2007, 196: 4521-37.
- [5] S. Banerjee, A.E. Gelfand and B.P. Carlin, “Hierarchical modeling and analysis for spatial data”, 2nd Ed., Crc Press, 2004.

The assessment of the upper-limb functionality: a method based on kinematic analysis.

M. Caimmi^{1,2}, M. Malosio^{1,2}, N. Pedrocchi¹, F. Vicentini¹, L. Molinari Tosatti¹

¹ *Inst. of Industrial Technologies and Automation, National Research Council of Italy, Via Bassini 15, Milano, Italy*

² *University of Brescia, Via Branze 38, Brescia, Italy*

Abstract— This paper describes the Reaching and Hand-to-Mouth evaluation method, a fast procedure to assess the upper-limb motor control and functional ability, providing a set of normative data from forty-two healthy subjects. Data were clustered into three subgroups of different ages to test the method sensitivity to motor control differences. Data from older and younger subjects show significant differences in the measures related to the ability for coordination, thus showing a proper sensitivity of the method to motor control differences. The presented method appears to be a suitable and reliable tool for the upper-limb functional assessment in the clinical environment.

Keywords— Upper Extremity; Kinematics; Reaching; Normative Data; Stroke; Neurological Disorders.

I. INTRODUCTION

KINEMATIC ANALYSIS has widely been used in clinics for almost 20 years for assessing, planning and monitoring the results of therapies in the rehabilitation of the Lower Limb (LL) of neurological patients **Error. L'origine riferimento non è stata trovata.** Similarly, it is recognized that the success of the Upper-Limb (UL) rehabilitation treatments largely depends on the possibility of defining the patient's functional pathological profile through objective quantification of motor performances [2].

Actually, the transfer of knowledge and experience gained in the LL movement analysis to the UL domain is actually hindered by several sources of complexities, related to both the kinematic model and the evaluation protocol to be used.

Regarding the model, being the UL a kinematically redundant multi-joint system [3] performing spatial movements, sophisticated models for skeleton-markers matching should be used for movement analysis. Unfortunately, a complex model doesn't comply with clinical requirements such as limiting the tracking setup overhead and avoiding time-expensive calibration procedures. Consequently, notwithstanding different 3D-models and computational methods have been proposed in the last years [4][5][6], but how to practically apply these models into the clinical practice is still an open problem and their impact on clinical procedures is therefore still limited.

Regarding the evaluation protocol, the complexity derives from both the very nature of the arm, which is inherently multitasking, and the nature of the performed movements that are far from being restricted to cyclic periodical uniform patterns like the gait [7]. Consequently, appropriate methods and evaluation protocols have to be defined and standardized in order to define a set of normative data to be used as reference.

This work summarizes the Reaching and Hand-to-Mouth Evaluation Method, a fast procedure to assess the upper-limb motor control and functional ability, providing a set of normative data from forty-two healthy subjects of different ages.

II. THE REACHING AND HAND TO MOUTH METHOD

A short description of the method is hereafter presented. The full version of the work containing all tables and graphs with normality data is available on line [8].

A. Participants

Forty-two healthy (neurologically and orthopedically intact) subjects, distributed uniformly between 18 and 80 years-old, were included in the study.

B. Study design

All subjects were evaluated through kinematic analysis using the presented method. Sixteen of them were re-evaluated two weeks after the first testing session in order to estimate the test-retest reliability of the method. The sensitivity was tested comparing dominant and nondominant limb results and clustering all subjects into three groups, namely young (18 – 35 years), middle-aged (36 – 50 years) and elderly subjects (51 – 80 years).

C. Functional tasks and protocol description

Two tasks were selected for evaluation, namely the Reaching Movement (RM, Fig.1) against gravity and the Hand-to-Mouth Movement (HtMM, Fig.1). The tasks were defined with the purpose of assessing the residual functional capability of the patient at the shoulder and elbow levels. More specifically the objective was to assess the ability of the patient of 1) extending the elbow while flexing the shoulder and 2) flexing the elbow, both movements performed against gravity. These are key movements from a functional point of view because they allow, respectively, 1) to reach for objects placed in front of the subject up to the shoulder height and 2)

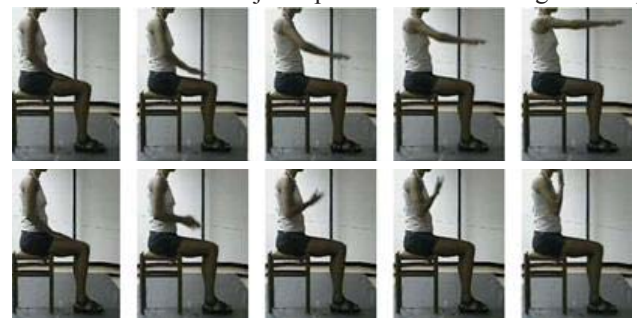


Fig.1 – The Reaching (upper panel) and Hand-to-Mouth (lower panel): frames at 0-33-50-66-100% of the movement

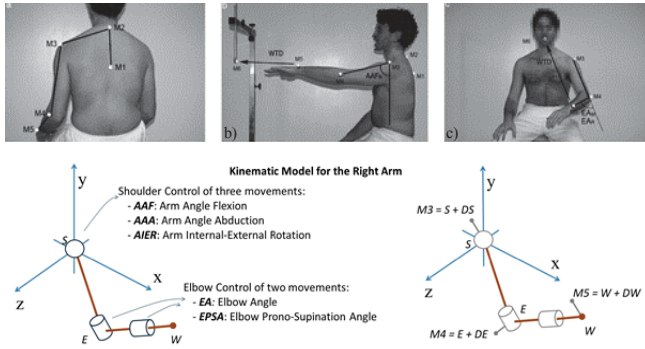


Fig.2 – Marker placement and kinematic model

to take objects towards the body and face. These patterns, in fact, allow the study of shoulder and elbow compound movements used in ADLs, such as reaching for objects and eating.

The subjects, sat on a chair adjustable for height, with the feet resting on the floor and the knees and hips bent at 90 degrees, performed two trials of at least 12 repetitions of the two movements (Fig.1) both with the dominant and nondominant arm.

D. The experimental setup and kinematic model

Data were collected with a 3-dimensional (3D) optoelectronic motion tracking system (8 TVc 100 Hz; Elite B[T]S, Italy) using the marker setup shown in Fig.2. In order to limit the overall set-up time, and facing the stringent requirements of the clinical practices, only 5 markers were used to track the arm kinematics. They were applied on: M1 spinous process of D5, M2 spinous process of C7, M3 acromion, M4 lateral epicondyle of the elbow and M5 styloid process of the ulna. A sixth marker, namely the target marker $M6 \equiv T$, was 1) for the RM, placed in front of the subject at exceeding reaching distance (Fig.2b), 2) for the HtMM, estimated on M2, a virtual target marker positioned inside the mouth (Fig.2c).

Neglecting the pronation and supination, the UL can be modelled as a 4 degrees-of-freedom kinematic serial chain (Fig.2). From marker placement description, the following assumption is made:

$$(S \approx M3, E \approx M4, W \approx M5) \quad (1)$$

Therefore, the flexion-extension Elbow Angle (EA) is calculated from markers {M3,M4,M5} positions, while the arm direction is identified with markers {M3,M4}, yielding the Arm Angle Flexion (AAF).

E. Dependent measures

Among the all-possible measurable and calculable variables, a meaningful set of measures was defined to assess the upper-limb functionality. The measures were selected aiming at answering these three following questions: 1) how fast, 2) how wide and 3) how well controlled are the two performed gestures. Therefore, the Movement Duration (MD), the shoulder and elbow angles at end movement (EA and AAF), a measure of repeatability, and a measure of smoothness were calculated for both movements.

Repeatability and smoothness were calculated on the M5 motion law, and are considered indirect measures of the subject motor control ability [8].

III. RESULTS

Numerical results, not reported for the sake of brevity, are deeply presented and commented in [8].

Results show no statistically significant differences between dominant and nondominant arm performances. The authors infer that tasks requiring more sensory feedback, greater force production and finer nervous control, like in the use of the hand, are probably better suited for this purpose.

The measures of the quality of movement (repeatability and smoothness) do highlight lower motor control ability in the elderly subjects, especially at lower executing velocity.

Besides the proper sensibility demonstrated by the method in clustering subjects of different groups of age, the method demonstrated high test-retest reliability for almost all investigated variables.

IV. CONCLUSION

The strength of the method is in its simplicity that regards both the model and the protocol used. It is fast and user friendly, both from the point of view of the patient and the operator. The method appears to be an adequate tool to be used for routine UL functional assessment in clinics equipped with a movement analysis laboratory. Future works will focus on testing more affordable and user-friendly acquisition solutions (such as the Microsoft Kinect sensor) in order to further extend the use of the method to smaller rehabilitation centres and clinical ambulatories.

ACKNOWLEDGEMENT

This work was partially supported by the Italian Lombardy region within the RIPRENDO@home project.

REFERENCES

- [1] DeLuca PA, Davis RB, and Ounpuu S "Alterations in surgical decision making in patients with cerebral palsy based on three-dimensional gait analysis". J Pediatr Orthop 1997, 17(5):608–614.
- [2] Alt Murphy M, Willen C, and Sunnerhagen KS, "Movement kinematics during a drinking task are associated with the activity capacity level after stroke", NNR 2012, 26(9):1106–1115.
- [3] Medendorp WP, Crawford JD, and Henriques DY, "Kinematic strategies for upper arm-forearm coordination in three dimensions", J. Neurophysiol. 2000, 84(5):2302–2316
- [4] Jaspers E, Feys H, and Bruyninckx H, "The reliability of upper limb kinematics in children with hemiplegic cerebral palsy". Gait Posture 2011, 33(4):568–575.
- [5] Rettig O, Fradet L, and Kasten P "A new kinematic model of the upper extremity based on functional joint parameter determination for shoulder and elbow" Gait Posture 2009, 30(4):469–476.
- [6] Cimolin V, Beretta E, and Piccinini L "Constraint-induced movement therapy for children with hemiplegia after traumatic brain injury: a quantitative study", J Head Trauma Rehabil 2012, 27(3):177–187.
- [7] Rau G, Disselhorst-Klug C, Schmidt R: Movement biomechanics goes upwards: from the leg to the arm. J Biomech 2000, 33(10):1207–1216.
- [8] Caimmi M., Guanziroli E., Malosio M., et al., "Normative Data for an Instrumental Assessment of the upper-limb functionality," BioMed Research International, In press, <http://www.hindawi.com/journals/bmri/aip/484131/>

Fractional-order hereditariness of porcine hearth valves

M. Cammarata^{1,3}, A.A. Giglia¹, D. Spadaro¹, and M. Zingales^{1,2}

¹ DICAM, UNIPA, viale delle Scienze Ed 8, 90128 Palermo, Italy, marcello.cammarata@unipa.it

² BNM²- LAB in MED-CHAB, Viale delle Scienze Ed.18, I-90128, Palermo, Italy, massimiliano.zingales@unipa.it

³ IEMEST via E. Amari 123, Palermo, Italy.

Abstract— The time-dependent behavior of cardiac valves leaflets is investigated in this paper from an experimental perspective. The results of mono and bi-axial tensile tests on sixteen samples of pulmonary and aortic porcine valves leaflets are reported in the paper. It is shown that performing a long-term creep/relaxation tests in physiological bath with the aid of BOSE bi-axial testing system, the time dependent creep (relaxation) obeys to a power-law of time with real exponent. In the context of linear viscoelasticity such a behavior permit to understand the way to the so-called fractional hereditary model of material behavior.

Keywords— Hearth valves, Relaxation , fractional viscoelasticity , biaxial tests.

I. INTRODUCTION

The mechanics of hearth valves represents an important issue of cardiac mechanics due to its strict correlation with the hemodynamic circulation. Indeed pathologies of the pulmonary and aortic valves is strongly correlated with thrombosis and/or to vessel atherosclerosis that are in turn causes of other pathologies of the cardio circulatory system. In this regard a proper mechanical characterization of the cardiac valve mechanics is very useful for a reliable evaluation of the stresses, and the strains of the cardiac muscles as well as for the correct numerical assessment of the hearth hemodynamics. Additionally, reliable model of cardiac valves materials is a guide to design more efficient artificial prosthesis replacing the pathological leaflets.

The analysis of hearth valves has been widely analyzed in scientific literature starting from the eighties of the last century [2] and several constitutive models for valve mechanics has been proposed [9]. One of the most accepted material behavior is represented by an orthotropic linear elastic model for the leaflet [3] and very little classical viscoelasticity has been found [4].

The lack for material viscoelasticity is, however, not justified from a mechanical perspective; indeed, as the material is modeled under the assumption of pure elasticity then, no damping of the material avoid membrane vibration. This pathological situation is only evidenced in presence of turbulence of the blood flux that is not present in homeostatic physiological condition.

II. MATERIAL AND METHODS

The paper focus on the time-dependent behavior of pulmonary as well as aortic porcine valves. Sixteenth pulmonary and aortic valves have been extracted from

sixteen porcine fresh hearths and saved in physiological isotonic solution 0.8% mol. Then the three leaflets composing the valves have been separated and three measures of the thickness with a digital caliber have been reported to evaluate the membrane stress during the tests. The leaflets have been grouped into three groups depending on their anatomical location in the valve.

Uniaxial mechanical tests on the valves is performed after placing a 2 mm by 1 mm sample from each leaflets in a hook grip for each side and are hold in isotonic solution 0.8% weight, at temperature of 37 °C during the entire duration of the test.

The mechanical test is provided by a four engines biaxial test bench BOSE LM250 (see fig.1).

Some preliminary results are shown in fig.2 in a stress-strain diagram. The uniaxial test is obtained with a constant load rate showing that, for the stress level applied, a slightly non-linear behavior may be observed in the measured results. In other tests, not reported here, it may be observed that the rate of load strongly influences the shape of the stress-strain curve that is a clear proof of the presence of material viscoelasticity. In this study we aim to explore further this behavior in terms of creep/relaxation showing, explicitly a time-dependence of the leaflet material [11]. From the preliminary results that we obtained so far the time dependence of the strain $\varepsilon(t)$ is of the form $\varepsilon(t) \propto t^\beta$ with $0 \leq \beta \leq 1$ and a statistical inference of the proper values of the proportionality coefficient as well as of the exponent β is provided in the study. Additionally, the anisotropic behavior [9,10] of the porcine leaflets will be investigated introducing biaxial tensile stresses with different levels of load between 0.5 N to 1.5N and different ratios among the load intensities along the two load directions.

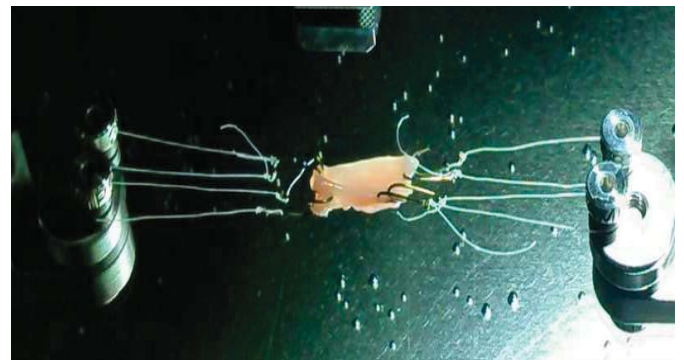


Fig. 1- Aortic leaflet in uniaxial test

The analytics fitting curve is then used to introduce a rheological mathematical model in terms of the so-called

fractional-order calculus. In this regard the time-dependent strain/stress of the material is provided by a Riemann-Liouville fractional-order integral/Caputo fractional derivative, of order β that is, mainly a convolution integral involving an hypersingular kernel [7,8]. Indeed, Riemann-Liouville fractional integral is defined as:

$$(I_{0+}^{\beta} f)(t) = \frac{1}{\Gamma(\beta)} \int_0^t (t-\tau)^{\beta-1} f(\tau) d\tau \quad (1)$$

and the Riemann-Liouville or Caputo fractional-order derivative, respectively, reads:

$$(D_{0+}^{\beta} f)(t) = \frac{1}{\Gamma(\beta-1)} \int_0^t (t-\tau)^{\beta-2} \dot{f}(\tau) d\tau + \frac{f(0)t^{-\beta}}{\Gamma(\beta)} \quad (2a)$$

$$({}^c D_{0+}^{\beta} f)(t) = \frac{1}{\Gamma(\beta-1)} \int_0^t (t-\tau)^{\beta-2} \dot{f}(\tau) d\tau \quad (2b)$$

and, in terms of fractional-order operators the rheological model of hearth valves may be defined, for uniaxial stress as:

$$\sigma(t) = C_{\beta} (D_{0+}^{\beta} \varepsilon)(t) \quad ; \quad \varepsilon(t) = \frac{1}{C_{\beta}} (I_{0+}^{\beta} \sigma)(t) \quad (3)$$

with the proportionality coefficient C_{β} obtained by best-fitting of the experimental curves in creep/relaxation.

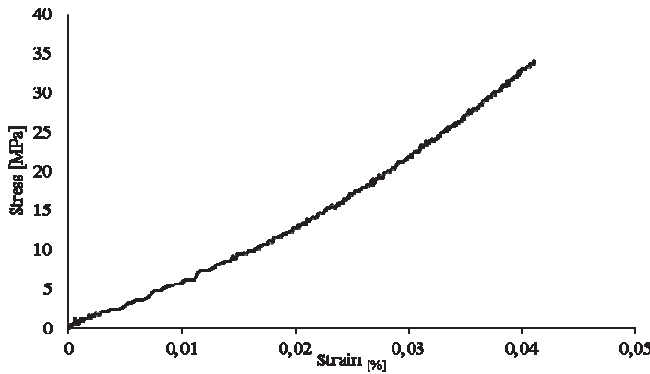


Fig.2- Stress strain diagram on a uniaxial test

III. CONCLUSIONS

The viscoelasticity of the hearth leaflets is investigated in the by creep and relaxation uniaxial and bi-axial tests in physiological environment. The curve of stress and/or strain are modeled using the fractional-order linear viscoelasticity already used by authors to model the long-term behavior of bones, tendons and lipid bilayer cell membranes. The model assumes isotropic fractional-order hereditariness providing the parameters of the material creep/relaxation as well as the description of the time-evolution of the Poisson ratio in terms of the Mittag-Leffler function that represents the fractional-order generalization of the well-known exponential function. The study aims to generalize the equations of anisotropic elasticity to the general case of anisotropic hereditariness that will be performed by additional, bi-axial, creep and relaxation tests. The troubles related to the non-instantaneous application of the load/displacement to the specimen is solved with the aid of the PDI filter of BOSE biaxial testing machine that provides optimization of the filter parameters with

respect to the mechanical behavior of the material. The obtained model of material viscoelasticity may be introduced in the numerical representation of hearth valves leaflets to yield a better simulation of the leaflets mechanics.

REFERENCES

- [1] M.M. Adamczyk, I. Vesely, "Characteristics of compressive strains in porcine aortic valves cusps." *J. Heart Valve Dis.* 11 (1), pp. 75–83, 2002.
- [2] N. Broom, G.W. Christie, "The structure/function relationship of fresh and glutaraldehyde-fixed aortic valve leaflets", In: Cohn, L.H., Gallucci, V. (Eds.), *Cardiac Bioprosthesis*. Yorke Medical Books, New York, pp. 477–491, 1982.
- [3] G. Burriesci, I.C. Howard, E.A. Patterson, "Influence of anisotropy on the mechanical behaviour of bioprosthetic heart valves", *Journal of Medical Engineering & Technology* 23 (6), pp. 203–215, 1999.
- [4] E.O. Carew, J.E. Barber, and I. Vesel, "Role of preconditioning and recovery time in repeated testing of aortic valve tissues: Validation through quasilinear viscoelastic theory", *Annals of Biomedical Engineering*, 28(9), pp.1093–1100, 2000.
- [5] G.W. Christie, "Anatomy of aortic heart valve leaflets: the influence of glutaraldehyde fixation on function", *Eur. J. Cardio-Thorac. Surg.* 6, pp. S25–S33, 1992.
- [6] K. Diethelm, A. D. Freed, "On the solution of non linear fractional-order differential equations used in the modeling of viscoplasticity," chapter in *Scientific Computing in Chemical Engineering II* – Springer, Hiedelberg, pp. 217 – 224, 1999.
- [7] L. Deseri, M. Di Paola, M. Zingales, P. Pollaci, "Power-law hereditariness of hierarchical fractal bones", *International Journal for Numerical Methods in Biomedical Engineering*, Vol 29, Issue 12, pp. 1338-1360, December 2013.
- [8] M. Di Paola, M. Zingales "Exact Mechanical Models for Fractional Viscoelastic Material", *Journal of Rheology*, Vol.58, pp. 988-1004, 2012.
- [9] J. Li, X.Y. Luo, Z.B. Kuang, "A nonlinear anisotropic model for porcine aortic heart valves", *Journal of Biomechanics* 34, pp. 1279–1289, 2001.
- [10] H. Mohammadi, Design and simulation of prosthetic heart valves. PhD thesis. Ontario: Biomedical Engineering, The University of Western Ontario, 2009.
- [11] M. Orosz, G. Molnarka, M. Toth, G.L. Nadasz, E. Monos. "Viscoelastic behavior of vascular wall simulated by generalized Maxwell models – a comparative study", *Medical Science Monitor*, 5(3) pp. 549–555, 1999.
- [12] M. S. Sacks, W.D. Merryman, D.E. Schmidt, "Review On the biomechanics of heart valve function", *Journal of Biomechanics* 42 1804–1824, 2009.
- [13] P. Ziopus, J.C. Barbenel, J. Fisher, "The mechanical properties of bovine pericardium", *Heart Valve Engineering*, London, pp. 99–102, 1986.

A refined yet simple shell finite element for soft biological tissues

F. Caselli, P. Bisegna

¹ *Department of Civil Engineering and Computer Science, University of Rome "Tor Vergata"*

Abstract—The main objective of this work is to develop a finite element procedure ideally suited for the simulation of thin-walled structures exhibiting a nonlinear material behaviour and undergoing large displacements, large rotations and large strains. Those kind of structures are typically encountered in biomedical applications involving soft biological tissues, such as e.g. the simulation of aneurisms or aortic valve biomechanics.

Keywords—Shell finite element, corotational approach, soft biological tissues.

I. INTRODUCTION

COMPUTATIONAL mechanics of thin biological structures is extremely challenging and demand for tailored finite element procedures. Consider, for instance, an aortic valve: the material behaviour is highly nonlinear due to the presence of unilateral collagen fibres; the valve leaflets undergo rotations of more than eighty degrees in each cardiac cycle; both membrane and bending dominated phases are present; snapping phenomena, contact and fluid-structure interactions are involved. As detailed in Section II, the finite element procedure here proposed to handle that interplay of complex features relies on two main ingredients: a polar decomposition based corotational framework [1] and an original core-element kinematic description [2].

II. METHODS

A. Corotational approach

The corotational approach is based on the idea of separating rigid body motions from strain producing ones. The fundamental idea is to find a transformation that operates like a filter on the global displacements, removing the rigid-body contribution before the finite element kernels use them (Figure 1). The main advantages are that the objectivity requirement is automatically fulfilled and most of the geometric nonlinearity of the problem is transferred to the transformation relating the filtered displacements to the total displacements. Therefore, for problems with arbitrarily large displacements and rotations but small strain response, existing high-performance linear elements can be reused as core elements without any modification.

Although the hypothesis of small strains is often suitable (e.g., SMA-based devices [3]), this is often not the case in applications involving thin sheets of rubber-like materials or soft biological tissues. As an example, during the diastolic phase the membrane strains in the aortic valve leaflets may reach values of 20% or even more in case of pathology. The restriction to small strains has represented a long-standing limitation for the corotational approach. One of the main

reason is that, in order to allow the extension to large strain problems, the correct identification of the element rigid motion plays a crucial role. As pointed out by Crisfield [4], a polar decomposition based corotational approach is required. In this work, a polar decomposition based corotational framework has been exploited, which enjoys the following features: i) closed-form formulas for the transformation operators and their variation are adopted, leading to simple algorithms for the computation of the residual vector and of the consistent tangent stiffness tensor; ii) a rigorous treatment of distributed dead and follower loads is performed.

B. Core-element kinematics

Once a corotational framework suited to large strains has been established, the challenge of developing an effective core-element remains. In this work, a novel method to develop corotational flat triangular shell elements for large strain problems is proposed. It is based on an original kinematic description of the core-element displacement field, based on the multiplicative (instead of additive) superposition of membrane and bending actions (Figure 2). In particular, the bending deformation is superimposed to an arbitrarily large membrane deformation accounting for thickness extensibility. Moreover, a simple approach to take into account the initial curvature of the shell mid-surface, suitable for the analysis of thin shells, is adopted.

III. RESULTS AND CONCLUSION

The resulting shell element is a three-node displacement-based triangle with performances comparable to refined mixed quadrilateral elements available in the literature. It is characterized by simple geometry and node configuration, which makes it attractive for applications involving complex features such as contact and fluid-structure interaction. In addition, it is objective, straightforwardly accounts for thickness extensibility, can take into account initial shell curvature at the element level, is equipped with a consistent tangent stiffness tensor, and works very well with fibred transversely isotropic biological materials under large strains and unilateral behaviour resulting from collagen fibre activation/deactivation.

The efficacy of the proposed approach is demonstrated by means of an extensive numerical campaign. As an example, the analysis of a fibre-reinforced cylindrical arch subjected to a compressive pressure load is reported in Figure 3. The numerical results show the soundness of the methodology and its capability to be effective in the simulation of complex problems such as, e.g., the biomechanics of the aortic valve.

REFERENCES

- [1] F. Caselli and P. Bisegna, "Polar decomposition based corotational framework for triangular shell elements with distributed loads", *Int. J. Numer. Methods Eng.*, vol. 95(6), pp. 499–528, 2013.
- [2] F. Caselli and P. Bisegna, "A corotational flat triangular element for large strain analysis of thin shells with applications to soft biological tissues", *Comput. Mech.*, vol. 54(3), pp. 847–864, 2014.
- [3] P. Bisegna, F. Caselli, S. Marfia and E. Sacco, "A new SMA shell element based on the corotational formulation", *Comput. Mech.*, vol. 54(5), pp. 1315–1329, 2014.
- [4] G. F. Moita and M. A. Crisfield, "A finite element formulation for 3-D continua using the co-rotational technique", *Int. J. Numer. Methods Eng.*, vol. 39(22), pp. 3775–3792, 1996.

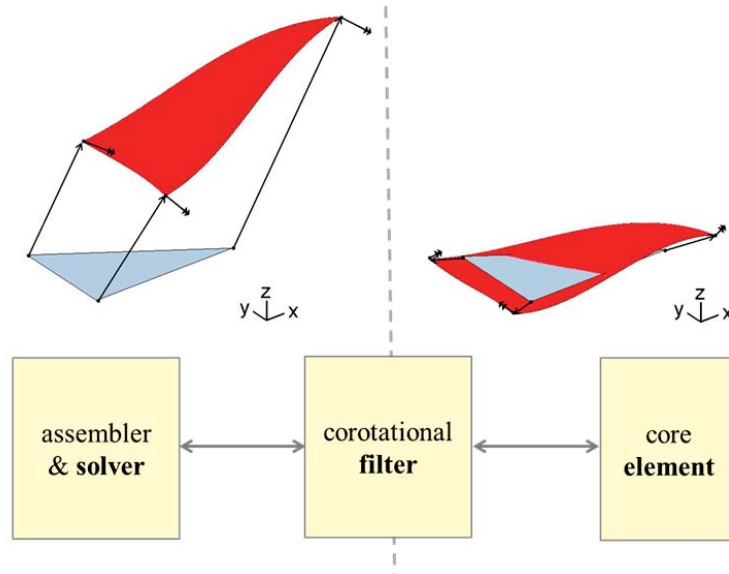


Figure 1: The corotational approach can be visualized like a filter, placed between the solver and the element routine, which purges out the rigid-body motion from the element transformation.

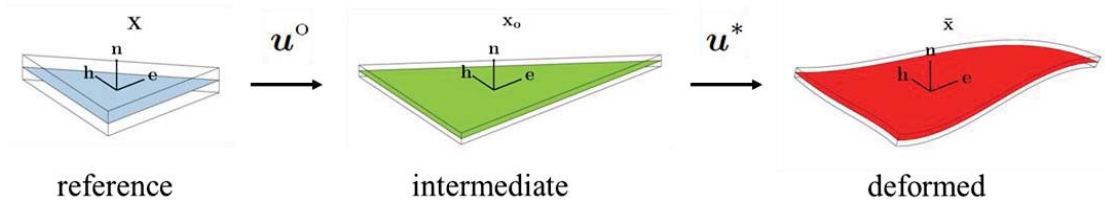


Figure 2: The core-element kinematics is regarded as the composition of an arbitrarily large membrane field u^O with thickness extensibility, mapping the reference configuration into an intermediate configuration, and a superimposed plate field u^* which keeps the element node fixed, mapping the intermediate configuration into the deformed configuration.

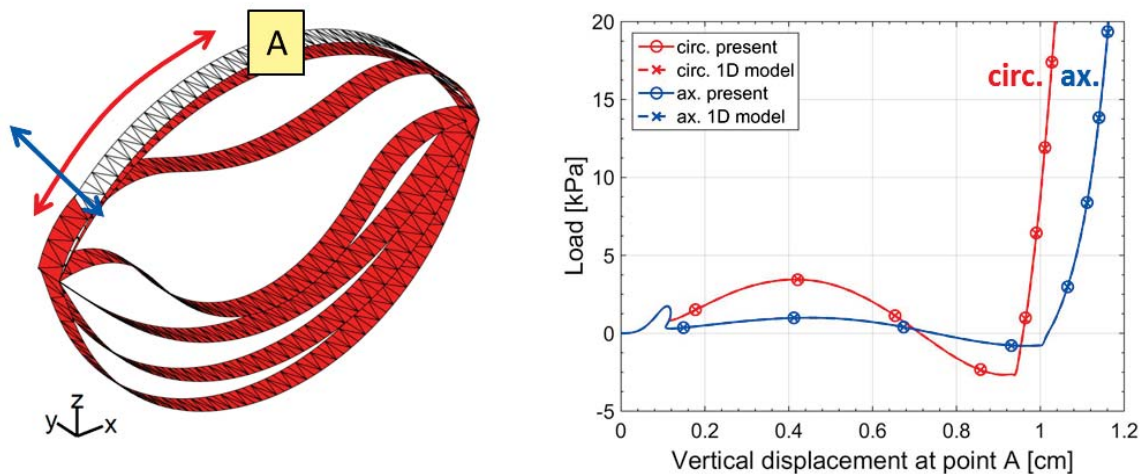


Figure 3: Fibre-reinforced cylindrical arch subjected to a compressive pressure load. On the left, reference configuration (in white) and some deformed configurations (in red). On the right, load-deflection curves relevant to circular (circ.) and axial (ax.) fibre orientation.

Coronary bifurcation virtual bench testing: two patient-specific cases

C. Chiastra^{1,2}, W. Wu¹, A. Aleiou³, H. Otake⁴, G. Dubini¹, J.F. LaDisa Jr.^{3,5} and F. Migliavacca¹

¹ Laboratory of Biological Structure Mechanics (LaBS), Department of Chemistry, Materials and Chemical Engineering "Giulio Natta", Politecnico di Milano, Milan, Italy

² Department of Biomedical Engineering, Thoraxcenter, Erasmus University Medical Center, Rotterdam, The Netherlands

³ Department of Biomedical Engineering, Marquette University, Milwaukee, WI, USA

⁴ Kobe University Graduate School of Medicine, Kobe, Japan

⁵ Department of Medicine, Division of Cardiovascular Medicine, Medical College of Wisconsin, Milwaukee, WI, USA

Abstract— The optimal stenting technique for treating diseased coronary artery bifurcations is still debated without a consensus among specialists. Patient-specific virtual simulations of coronary bifurcation stenting can be used by interventional cardiologists to compare the effect of different stent designs or stenting strategies on structural and fluid dynamic results in order to identify the optimal solution for each individual's anatomy. In this study, patient-specific simulations of stent deployment are performed to replicate the complete procedure followed by clinicians to treat coronary bifurcations. Subsequent fluid dynamics analyses are conducted to quantify the influence of hemodynamics quantities. The study shows the feasibility of performing virtual stenting simulations starting from patient-specific pre-operative coronary bifurcation models, and that this approach may be useful in determining an optimal choice in terms of stent type for each patient.

Keywords— stent, coronary bifurcation, finite element analysis, computational fluid dynamics.

I. INTRODUCTION

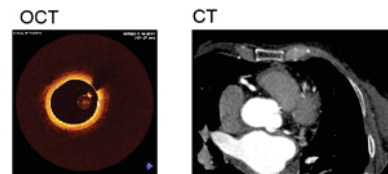
THE treatment of coronary bifurcations remains a challenge in interventional cardiology because of lower success rates and higher restenosis rates as compared to non-bifurcated lesions [1]. The optimal stenting technique for treating diseased coronary artery bifurcations is still debated without a consensus among interventional cardiologists [1]. Indeed, the post-operative follow-up is influenced by different factors such as stent design, the use of one or two stents, plaque morphology and composition, damage caused to the arterial wall, and adverse hemodynamics induced by the stent struts protruding inside the lumen. In this context, virtual simulations of patient-specific coronary bifurcation stenting can be used by cardiologists to compare the effect of different stent designs or stenting strategies on structural and fluid dynamics results in order to identify the optimal solution for each individual's anatomy [2].

In this work, patient-specific simulations of stent deployment are performed to replicate the complete procedure followed by clinicians to treat coronary bifurcations. The reliability of finite-element simulations in predicting post-operative geometric outcomes is investigated. Subsequent fluid dynamics analyses are also conducted to quantify the influence of hemodynamics variables such as wall shear stress (WSS) from two different commercial coronary stents (i.e. Xience Prime by Abbott Vascular, USA and Nobori by Terumo, Japan).

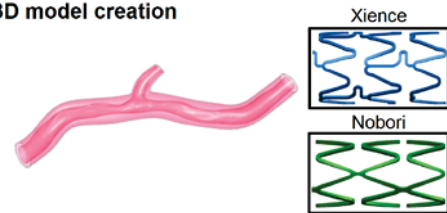
II. MATERIALS AND METHODS

TWO patient-specific pre-operative models of coronary bifurcations were reconstructed from CT angiography and optical coherence tomography (OCT) images (Fig. 1a-b) [3]. Plaque location and composition were determined from OCT and assigned to the model. Structural simulations of stent deployment were then performed by means of the

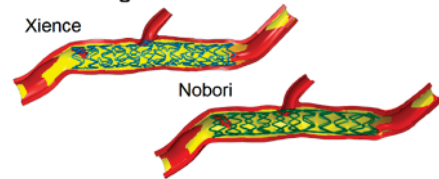
A) Patient-specific imaging



B) 3D model creation



C) Virtual stenting



D) CFD analysis

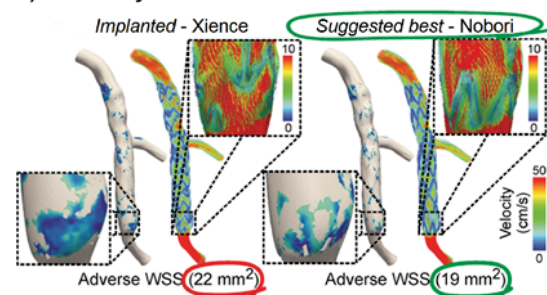


Figure 1 - Example of workflow that was followed for a patient-specific case, from the clinical images to the structural and fluid dynamic simulations.

commercial finite-element solver ABAQUS/Explicit (Dassault Systemes, USA) (Fig. 1c). Detailed information on the methods used can be found in Morlacchi et al. [4]. The final geometric configurations obtained through virtual stent expansion were used to conduct computational fluid dynamics (CFD) simulations using the open-source software Simvascular (simtk.org) (Fig. 1d). This sequential structural and fluid dynamic approach allows taking into account the vessel deformation caused by stent expansion which has a major impact on the haemodynamic environment [5-7]. Inflow boundary conditions were based on body surface area. Downstream vascular resistances and capacitances were applied at the outlets to obtain physiological flow-splits [3].

III. RESULTS AND DISCUSSION

THE deformed lumen geometry after virtual stenting expansion was compared against the corresponding post-operative geometry created from patient-specific OCT data. Figure 2 shows the superimposition between the two geometries for one example case. The match between the two superimposed geometries is qualitatively good in the stented region. Quantitatively, more than 70% of this region in the simulation has an acceptable distance ($< 90 \mu\text{m}$) from the correspondent post-operative reconstruction.

Prior idealized CFD stenting results suggested lower stent-to-artery area ratios and thin struts were most favorable. Our findings to date indicated geometric perturbations for a given patient influencing near-wall velocity patterns also factor importantly into the results. For instance, our findings suggest that some patients would have benefited from a stent other than that truly implanted in the patient coronary bifurcation (Fig. 1d). These results were due to the strut thickness of the implanted stent, the geometric stent pattern, and the amount of malapposition from local plaque features.

IV. CONCLUSION

THIS study demonstrates the feasibility of performing coronary bifurcation virtual stenting simulations starting from patient-specific pre-operative data, and that the proposed methodology is reliable taking into account intrinsic errors and assumptions due to image reconstruction and numerical modeling. Furthermore, the proposed

workflow, from structural to fluid dynamic simulations, might provide useful information for pre-interventional planning by choosing the best stenting strategy for each patient.

ACKNOWLEDGEMENT

C. Chiastra is partially supported by the ERC starting grant (310457, BioCCora).

REFERENCES

- [1] J.F. Lassen, N.R. Holm, G. Stankovic, T. Lefevre, A. Chieffo, D. Hildick-Smith, M. Pan, O. Darremont, R. Albiero, M. Ferenc and Y. Louvard, "Percutaneous coronary intervention for coronary bifurcation disease: consensus from the first 10 years of the European Bifurcation Club meetings," *EuroIntervention*, vol. 10, pp. 545-560, September 2014.
- [2] P. Mortier, M. De Beule, G. Dubini, Y. Hikichi, Y. Murasato and J.A. Ormiston, "Coronary bifurcation stenting: insights from in vitro and virtual bench testing," *EuroIntervention*, vol. 6 Suppl., pp. J53-J60, December 2010.
- [3] L.M. Ellwein, H. Otake, T.J. Gundert, B.-K. Koo, T. Shinke, Y. Honda, J. Shite and J.F. LaDisa Jr., "Optical Coherence Tomography for Patient-specific 3D Artery Reconstruction and Evaluation of Wall Shear Stress in a Left Circumflex Coronary Artery," *Cardiovasc. Eng. Technol.*, vol. 2, pp. 212-227, September 2011.
- [4] S. Morlacchi, S.G. Colleoni, R. Cárdenes, C. Chiastra, J.L. Diez, I. Larrabide and F. Migliavacca, "Patient-specific simulations of stenting procedures in coronary bifurcations: two clinical cases," *Med. Eng. Phys.*, vol. 35, pp. 1272-1281, September 2013.
- [5] S. Morlacchi, C. Chiastra, D. Gastaldi, G. Pennati, G. Dubini and F. Migliavacca, "Sequential structural and fluid dynamic numerical simulations of a stented bifurcated coronary artery," *J. Biomech. Eng.*, vol. 133, pp. 121010, December 2011.
- [6] C. Chiastra, S. Morlacchi, S. Pereira, G. Dubini and F. Migliavacca, "Computational fluid dynamics of stented coronary bifurcations studied with a hybrid discretization method," *Eu. J. Mech., B/Fluids*, vol. 35, pp. 76-84, September 2012.
- [7] Martin, E.A. Murphy, and F.J. Boyle, "Computational fluid dynamics analysis of balloon-expandable coronary stents: influence of stent and vessel deformation," *Med. Eng. Phys.*, vol. 36, pp. 1047-1056, August 2014.

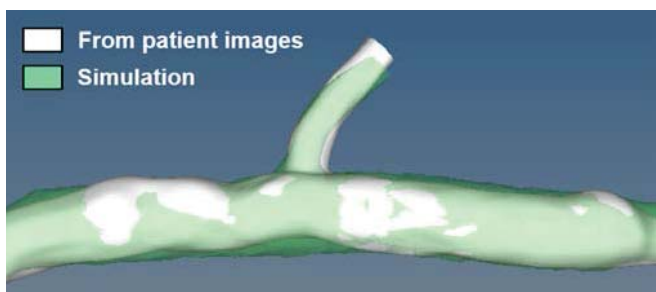


Figure 2 - Comparison between the post-operative geometry reconstructed from patient images and the geometry obtained after virtual stent deployment.

A morphometry-based lumped parameter model of the coronary circulation under resting and hyperemic conditions

C. Corsini¹, C. Chiastra^{1,2}, S. Brianni¹, G. Cardillo¹, and G. Pennati¹

¹ Department of Chemistry, Materials and Chemical Engineering "Giulio Natta", Politecnico di Milano, Milan, Italy.

² Department of Biomedical Engineering, Thoraxcenter, Erasmus MC, Rotterdam, The Netherlands.

Abstract—Coronary flow reserve (CFR) and fractional flow reserve (FFR) are two indexes currently used in interventional cardiology to quantify the severity of coronary lesions. Although providing important information about coronary physiology, these indexes are derived from invasive measurements performed on the patient. The aim of this study is to develop a pure lumped parameter model of the entire coronary circulation, based on morphometric data, which can provide hemodynamic information at varying stenosis degree and location. The developed model included the epicardial arteries, microcirculation and veins. Epicardial arteries were represented by a linear resistance (R), a non-linear term reproducing the potential stenosis contribution, an inductance and a compliance (C). Downstream vessels were represented by RC blocks derived from the epicardial branches through morphometric laws. Both resting and hyperemic conditions were simulated with varying stenosis degree and location. The model showed good matching of the flow curves and mean values with data reported in the literature. From the CFR and FFR values obtained from the model, it was possible to quantify the contribution of the single stenosis for different degrees of the lesion itself, as well as of other sequential stenoses. This model may find an application in the clinical environment, since it can provide, in a rapid and non-invasive way, a valuable metric to quantify patient-specific coronary lesions severity.

Keywords—Coronary artery disease, mathematical model, coronary flow reserve, fractional flow reserve.

I. INTRODUCTION

CARDIOVASCULAR diseases are the leading cause of death in the world today, with about 13% of all deaths being due to coronary artery disease [1]. The development of reliable diagnostic tools is extremely important to assess myocardial ischemia, thus preventing fatal events such as myocardial infarction. In the last decades two different measurements have been introduced to quantify coronary physiology: coronary flow reserve (CFR) and fractional flow reserve (FFR). CFR is defined as the ratio between the coronary blood flow under maximum hyperemic conditions and the flow at resting conditions (Q_c). Physiologically it ranges between 3 and 4 [2]–[3], while it decreases below 2, which is commonly taken as a threshold, in the presence of one (or multiple) epicardial stenosis [3]. FFR is defined as the ratio between the coronary flow supplied by a stenotic artery and that supplied by the same artery in the hypothetical absence of the stenosis, with both flows measured at maximum hyperemia [4]. Assuming that the microvascular resistance, at maximum vasodilation, does not depend on the presence of epicardial stenoses, the FFR flow ratio can be approximated by the ratio of distal (P_d) to proximal (P_p) pressures over the stenosis. In interventional cardiology, FFR

is calculated by measuring P_d and, simultaneously, the aortic pressure P_{AO} with an invasive catheter-based procedure. The index is close to 1 in normal conditions, whereas values below 0.8 indicate lesions potentially responsible for myocardial ischemia, therefore eligible for a medical treatment [5]. When sequential stenoses are present in the same coronary artery, the value of FFR, as measured by cardiologists, does not discriminate the effects of the single lesions [5]. This study presents a pure lumped parameter model of the coronary circulation based on morphometric data. The aim is to investigate the relationship between CFR and FFR at varying stenosis degree and location, considering the contributions of the single lesions if placed sequentially along the artery.

II. MATERIALS AND METHODS

A. Lumped-parameter model

A lumped-parameter model of the entire coronary vasculature was developed, including the epicardial arteries, the microcirculation (i.e. arterioles, capillaries and venules) and the venous circulation (Fig. 1).

Each epicardial vessel, namely the left main (LM) and right (RCA) coronary arteries with their branches, down to those with 0.5 mm diameter, was represented by: *i*) a linear resistance responsible for the viscous pressure drops; *ii*) a non-linear resistance reflecting the fluid-dynamic behaviour of a stenosis (if present); *iii*) an inductance accounting for blood flow inertial effects; *iv*) a compliance reproducing vessel wall deformability (Fig. 1). These lumped parameters were based on morphometric data collected from cadavers or *in vivo* by means of imaging tools, and reported in the literature.

Resistances and compliances of the vascular beds originating from the epicardial terminal branches were derived using morphometric relationships and subdividing into endocardial arteries, arterial and venous sides of the microcirculation, and coronary veins (Fig. 1). The effect of the intra-myocardial pressure acting on the vascular bed compliances was reproduced as different fractions of the time-varying left ventricular pressure $P_{LV}(t)$, depending on the compliance location (Fig. 1) [6].

The model was implemented in Matlab (MathWorks, Inc., Natick, MA, USA), requiring few minutes to simulate 10 cardiac cycles, necessary to assure solution stability.

B. Boundary conditions

A time-varying aortic pressure $P_{AO}(t)$ was imposed as the

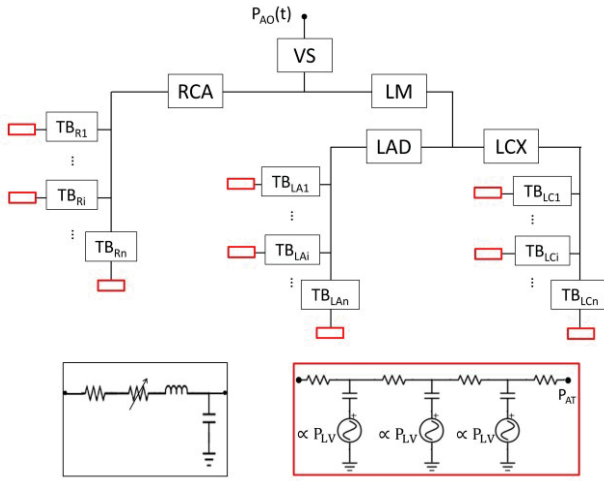


FIGURE I: Lumped parameter model including the epicardial coronary arteries (black boxes) and downstream vascular beds (red boxes). VS=Vasalva sinus; RCA=right coronary artery; LM = left main – LAD = left anterior descending – LCX = left circumflex coronary arteries; $TB_{R/Li}$ =right/left i^{th} terminal branch ranging from 1 to n . $P_{AO}(t)$ = time-varying aortic pressure; P_{AT} = atrial pressure; P_{LV} = left ventricular pressure.

inlet boundary condition of the model. The pressure tracing was fitted with a 8-order Fourier series, and could be modulated according to the arbitrarily chosen maximum and minimum values, as well as the heart rate.

A constant atrial pressure was prescribed as the outlet boundary condition of the model, whereas $P_{LV}(t)$ (Section A) was based on $P_{AO}(t)$ and fitted with a 8-order Fourier series.

C. Simulation of hyperemia and stenosis

Hyperemic conditions were simulated by reducing the resistances associated to each vascular bed, to 21% of its resting value [2]. $P_{AO}(t)$ was not changed during maximal vasodilation, based on the assumption that FFR is independent of the systemic hemodynamics variations [5].

The effect of potential coronary lesions were simulated by varying the stenosis degree, calculated as the percentage reduction of the vessel lumen, from 0 to 80%, and by varying the stenosis location (e.g. left anterior descending coronary artery – LAD – only, or combined with LM) both under resting and hyperemic conditions. From each simulation, CFR and FFR values were obtained. In particular, the latter was calculated both as measured by cardiologists (FFR_c) and specific to the single stenosis (FFR_s), i.e. P_d normalized to P_{AO} or P_p , respectively.

III. RESULTS AND DISCUSSION

The model showed good matching of the flow curves and mean values obtained in the major epicardial vessels under resting and physiological conditions, compared with the velocity tracings reported in the literature. Namely, the ratios of systolic to diastolic flow peaks were equal to 0.37 and 0.8 for the LM and RCA, respectively, in accordance with [7].

Mean flow rates resulting from simulations at varying stenosis degree and location were reasonable and the trend was comparable with that found in the literature [3].

Results in terms of CFR and FFR_s , referred to LAD lesions, are shown in Fig. II, for sequential LM and LAD stenoses varying from 0 to 80%. From this figure it is possible to better quantify the contribution of the LAD

stenosis for different LM lesion severities. Furthermore, one can observe that, while CFR is considerably influenced by stenoses degrees, FFR_s is not affected by the upstream narrowing, when considering the same downstream stenosis.

IV. CONCLUSION

This study presents a pure lumped parameter model of the coronary circulation, based on morphometric data, which can rapidly provide reliable results describing the coronary hemodynamics in physiological and pathological conditions. Although further investigations and improvements are required, this model may find an application in the clinical environment, since it can provide, in a rapid and non-invasive way, a valuable metric to quantify patient-specific coronary lesions severity.

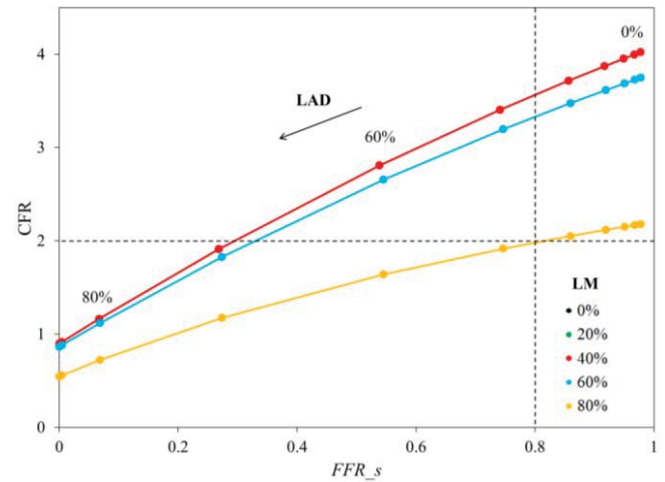


FIGURE II: Values of FFR_s vs. CFR resulting from the model for varying LAD stenoses (circles joined with solid lines) at different LM stenoses (different colors).

ACKNOWLEDGEMENT

C. Chiastra is partially supported by the ERC starting grant (310457, BioCCora).

REFERENCES

- [1] World Health Organization website: <http://www.who.int/mediacentre/factsheets/fs317/en/>
- [2] W. M. Chilian, S. M. Layne, E. C. Klausner, C. L. Eastham, and M. L. Marcus, "Redistribution of coronary microvascular resistance produced by dipyridamole", *Am. J. Physiol.*, vol. 256, pp. H383-90, Feb. 1989.
- [3] K. L. Gould, K. Lipscomb, and G. W. Hamilton, "Physiologic basis for assessing critical coronary stenosis. Instantaneous flow response and regional distribution during coronary hyperemia as measures of coronary flow reserve", *Am. J. Cardiol.*, vol. 33, pp. 87-94, Jan. 1974.
- [4] N. H. Pijls, J. A. van Son, R. L. Kirkeeide, B. De Bruyne, and K. L. Gould, "Experimental basis of determining maximum coronary, myocardial, and collateral blood flow by pressure measurements for assessing functional stenosis severity before and after percutaneous transluminal coronary angioplasty", *Circulation*, vol. 87, pp. 1354-1367, Apr. 1993.
- [5] B. De Bruyne, and J. Sarma, "Fractional flow reserve: a review", *Heart*, vol. 94, pp. 949-59, Jul. 2008.
- [6] A. van der Horst, F. L. Boogaard, M. van't Veer, M. C. M. Rutten, N. H. J. Pijls, and F. N. van de Vosse, "Towards patient-specific modeling of coronary hemodynamics in healthy and diseased state", *Comput. Math. Methods Med.*, vol. 2013:393792, doi: 10.1155/2013/393792.
- [7] S. Matsuo, M. Tsuruta, M. Hayano, Y. Imamura, Y. Eguchi, *et al.*, "Phasic coronary artery flow velocity determined by Doppler flowmeter catheter in aortic stenosis and aortic regurgitation", *Am. J. Cardiol.*, vol. 62, pp. 917-22, Nov. 1988.

Multi-scale approach for the biomechanical characterization of human skin lesion

E. Cutri¹, G. Spatafora¹, G. Franzetti¹, F. Crippa¹, E. Montin², L. Mainardi², L. Spadola³, A. Testori³ and G. Pennati¹

¹*LaBS-Depart. of Chemistry, Materials and Chemical Engineering, 'Giulio Natta', Politecnico di Milano, Milan, Italy.*

²*Depart. of Electronics, Information and Bioengineering, Politecnico di Milano, Milan, Italy.*

³*Dermatological Surgery Division, Istituto Europeo di Oncologia, Milan, Italy.*

Abstract— Cutaneous malignant melanoma is an aggressive tumour whose rate of survival dramatically increases if early diagnosis is provided to the patients. Alteration on the mechanical properties of the nevus under pathological conditions has been assessed. In this context, we aim at developing a multi-scale approach ranging from the cellular level to the tissue level to describe the mechanical behaviour of the skin and skin lesion. Such models will be validated against confocal laser scanning microscopy data to estimate the mechanical properties of the different layers of the skin and skin lesions. In such a way, possible alteration of the local mechanical properties in case of a pathological condition will be evaluated.

Keywords— skin lesion, multiscale, biomechanics.

I. INTRODUCTION

CUTANEOUS melanoma represents an aggressive malignant tumour whose incidence rate has risen faster than those for any other malignancy in Caucasian populations over the last 30 years [1]. Despite cutaneous melanoma is less common than other skin cancers, the mortality is higher, causing approximately the 90 % of deaths related to skin cancer [2]. Up to date, the most common method for detecting melanoma is visual diagnosis based on the so called ABCD or ABCDE rules [3]. Suspicious melanoma undergo to excision biopsy and subsequent histological analysis. Novel imaging techniques such as confocal laser scanning microscopy (CLSM) improved diagnostic accuracy but a definite and final diagnosis without the need of excision biopsy and histological analysis has not been achieved. Several studies assessed an alteration in the local mechanical properties of biological tissues under pathological conditions such as carcinoma [4]-[5] or melanoma [6]-[8]. In this view, the characterization of the skin and the skin lesion properties may serve to provide further understanding of the alteration occurring under pathological condition. To this aim, we propose a multi-scale approach ranging from the cellular scale to the tissue scale to describe the biomechanical behavior of the skin and skin lesion paying attention to the alteration of the biomechanical properties of the skin layers under pathological conditions. The developed models will be then validated against clinical measurement obtained from confocal laser scanning microscopy (CLSM), a technique able to provide non-invasive histomorphological analysis of skin *in vivo*.

II. METHODS

In order to fully represent both the skin and the skin lesion, two different models accounting for two different spatial scales are developed: i) cellular scale model, whose aim is to describe the local mechanical properties of different types of cell (i.e., melanocytes and keratinocytes); ii) tissue scale model accounting for the contributions of the different skin layers (i.e., epidermis, dermis, etc.). Once the models are set-up, the response of either the cells either the tissue upon a mechanical stimuli (e.g., displacement) will be evaluated and compared to the data obtained from the confocal images to estimate the two models parameters.

A. Experimental set-up

Once the nevus to be analysed is chosen, a stack (in plane resolution 500µm×500µm, depth 150µm) is acquired for three different regions: skin lesion, skin and the border in between. All these acquisitions are repeated for the undeformed and the deformed (traction force applied to the skin) configurations. The displacement field is then reconstructed by means of a registration strategy which estimates the best alignment of the deformed image and the undeformed one. The strategy is based on the classical global plus local approach which concerned two transformations: a rototraslation and a non-rigid one. The global registration accounts both for patients movement during the scan and the large tissues deformations due to the applied stress, the non-rigid one accounts for the different deformability of the tissues composing the nevus.

B. Cellular scale model

The cellular model is developed by means of the open source code **Chaste** (Cancer, Heart And Soft Tissue Environment, University of Oxford) [9] which allows the modelling of the interactions among different types of cells. Two different families of cells are simulated, each having different mechanical properties (fig.1a). The modelling of skin and the skin lesions is achieved by properly assign the ratio of melanocytes and keratinocytes. A displacement field is applied to the upper boundary to replicate the experimental condition.

C. Tissue scale model

The 3D tissue scale model is developed using Abaqus 6.13

® (SIMULIA, Dassault Systèmes, France). An anatomy-based geometry is developed whose parameters can be varied to model different geometrical configurations (fig.1b). To account for the different biomechanical properties of the different skin layers, proper constitutive laws are assigned to each layer according to literature data [10]. The material parameters of the different layers are initially assigned according to [10]. The model is complemented with adequate boundary conditions to reproduce the *in vivo* condition. A displacement field is then applied to the upper layer to reproduce the experimental stimuli.

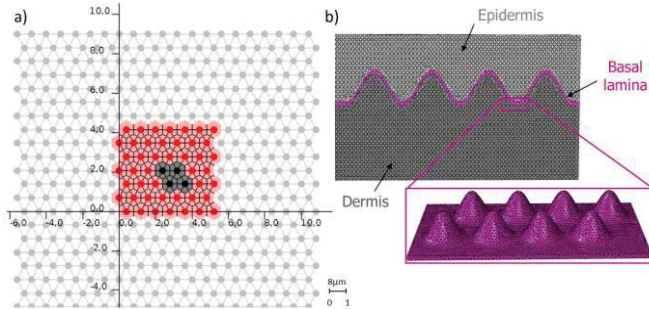


Figure 1: Multi-scale modelling approach: a) scale level model accounting for different families of cells; b) tissue level model accounting for the different skin layers.

D. Parameter estimation

Cellular scale model. The displacement field of sets of cells located in different layers of the skin and skin lesion are reconstructed from CLSM images. The parameters of the cellular scale model describing the cells interaction and the cells stiffness are then optimized to reproduce the displacement field from the images.

Tissue scale model. The results provided by the tissue level model are compared to the displacement field reconstructed from the images. The material parameters of each layer are then selectively tuned until the experimental displacement is reproduced.

III. RESULTS

Preliminary results obtained using material parameters from literature show a discrepancy of the displacements provided by both the cell scale model and the tissue scale model and the ones from the images reconstruction. This result can be due to the wide variety of literature data [10]-[12], which is strongly dependent from the different site locations, age and race as well as from the measurement technique. After the tuning of the parameters is performed more compatible results are found.

IV. CONCLUSION

Malignant melanoma presents a high mortality rate if early diagnosis is not provided. The 5-year survival rate if melanoma is detected at an early stage is equal to 99% [2]. Despite the improvement in the diagnostic technique, a definite diagnosis still requires excision biopsy and subsequent histological analysis. Alteration in the local mechanical properties under such a pathological condition are assessed by literature study. In this context, we proposed a

multi-scale approach combining information from a cell scale model and a tissue level model. The integration of this information together with the data from the CLSM reconstruction allows the estimation of the material parameters under both physiological and pathological information. In this way, further understanding of such pathology can be achieved as well as interesting indication to support clinical diagnosis.

ACKNOWLEDGEMENT

This study was supported by Istituto Europeo di Oncologia.

REFERENCES

- [1] A. V. Giblin and J.M. Thomas "Incidence, mortality and survival in cutaneous melanoma," *Journal of Plastic, Reconstructive & Aesthetic Surgery* vol. 60 pp. 32-40, 2007.
- [2] Skin Cancer Foundation. Skin Cancer Facts. 2012. Available from: <http://www.skincancer.org/Skin-Cancer-Facts>. Accessed August 3, 2012.
- [3] R.J. Friedman, D.S. Rigel and A.W. Kopf "Early detection of malignant melanoma: The role of physician examination and self-examination of the skin," *Ca-A Cancer Journal for Clinicians* vol. 35 pp. 130-151, 1985.
- [4] M.J. Paszek, N. Zahir, K.R. Johnson, J.N. Lakins, G.I. Rozenberg, A. Gefen, C. A. Reinhart-King, S. S. Margulies, M. Dembo, D. Boettiger, D. A. Hammer, V. M. Weaver, "Tensional homeostasis and the malignant phenotype," *Cancer Cell* vol. 8(3) pp.241-54, 2005
- [5] M. Plodinec, M. Loparic, C.A. Monnier, E.C. Obermann, R. Zanetti Dallenbach, P. Oertle, J.T. Hyotyla, U. Aebi, M. Bentières-Alj, R.Y. Lim and C.A. Schoenenberger, "The nanomechanical signature of breast cancer," *Nat Nanotechnol* vol. 7(11) pp.757-65, 2012.
- [6] M.I. Miga, M.P. Rothney and J.J. Ou, "Modality independent elastography (MIE): potential applications in dermoscopy," *Med Phys* vol. 32(5) pp.1308-20, 2005
- [7] S.J. Kirkpatrick, R.K. Wang, D.D. Duncan, M. Kulesz-Martin and K., Lee, "Imaging the mechanical stiffness of skin lesions by in vivo acousto-optical elastography," *Optics express* vol. 14(21) pp. 9770-9, 2006
- [8] G. Weder, M. C. Hendriks-Balk, R. Smajda, D. Rimoldi, M. Liley, H. Heinzelmann, A. Meister, and A. Mariotti. "Increased plasticity of the stiffness of melanoma cells correlates with their acquisition of metastatic properties," *Nanomedicine: Nanotechnology, Biology, and Medicine* vol. 10 pp. 141:148, 2014
- [9] G.R. Mirams, C.J. Arthurs, M.O. Bernabeu, R. Bordas, J. Cooper, A. Corrias, Y. Davit, S.J. Dunn, A.G. Fletcher, D.G. Harvey, M.E. Marsh, J.M. Osborne, P. Pathmanathan, J. Pitt-Francis, J. Southern, N. Zemzemi and D.J. Gavaghan, "Chaste: An open source C++ library for computational physiology and biology," *PLoS Comput. Biol.* vol. 9(3), 2013.
- [10] O. Kuwazuru, J. Saotthong and N. Yoshikawa "Mechanical approach to aging and wrinkling of human facial skin based on the multistage buckling theory," *Medical Engineering and Physics* vol. 30 pp. 516-522, 2008.
- [11] C. Pailler-Mattei, S. Bec and H. Zahouani "In vivo measurements of the elastic mechanical properties of human skin by indentation tests," *Medical Engineering and Physics* vol. 30 pp. 599-606, 2008.
- [12] M. Sarna, A. Zadlo, A. Pilat, M. Olchawa, P. Gkogkolou, K. Burda, M. Böhm and T. Sarna, "Nanomechanical analysis of pigmented human melanoma cells," *Pigment Cell and Melanoma Research* vol. 26 pp.727-730, 2013.

Digital Volume Correlation (DVC) to investigate the strain distribution and failure in Prophylactic augmented Vertebrae

Valentina Danesi¹, Gianluca Tozzi², Marco Palanca¹, Renzo Soffiatti³, Luca Cristofolini¹

¹ Department of Industrial Engineering, University of Bologna, Italy;

² School of Engineering, University of Portsmouth, UK;

³ Tecres SpA, Sommacampagna, Verona, Italy

Abstract— There is a need to investigate the strength of the vertebral body after reinforcement treatments such as augmentation. The aim of the present study was to investigate the biomechanical efficacy of prophylactic augmentation in preventing fracture of non-fractured vertebral bodies. In conjunction with high-resolution μ CT imaging, this study applied DVC to investigate the strain distribution of augmented porcine vertebrae during compression testing, to assess the effect of different types of augmentation materials. The force and work to ultimate failure in prophylactic augmented vertebrae was consistently larger than in the control. However, in some case the first-failure force and work were lower than the control. The strain pattern investigated suggested that the most critical region was the bone-cement interface, where the onset of the fracture was recognizable. The failure mechanism did not seem to depend on the cement type.

Keywords—Biomechanics, augmentation, *in vitro* testing, digital volume correlation (DVC), vertebral body, strain measurement.

I. INTRODUCTION

Trauma, osteoporosis and bone metastases are the most common causes of vertebral fractures, which can lead to severe consequences and mortality [1]. Surgical procedures involving fixation or augmentation can be jeopardized by a limited understanding of the spine biomechanics [2]. In-depth knowledge of the stress distribution in the vertebral body is fundamental to improve the understanding of spine biomechanics in health and disease subjects, during ageing [3], and to improve surgical treatment [4]. Because of the difficulty of accessing the *in vivo* loads, *in vitro* measurements of the stress-strain relationship in the vertebral body can provide valuable indirect information about spine biomechanics. However, traditional experimental techniques such as strain gauges are restricted to the surface of specimens where no internal strain distribution could be interrogated. With the recent and rapid progress of micro-focus computed tomography (μ CT) in conjunction with *in situ* mechanical testing [5, 6], DVC has become a powerful tool to examine full-field deformations in trabecular bone [7], whole bones [8], cellular scaffolds [9] and recently bone-

cement composites [10]. The aim of this study is the application of Digital Volume Correlation (DVC) in conjunction with high-resolution micro-CT imaging, to investigate the strain distribution coupled with local and global failure mechanism of augmented vertebrae during compression. Furthermore, the effect of different types of augmentation materials was assessed.

II. MATERIALS AND METHODS

Twelve single thoracic porcine vertebrae (T1, T2 and T3) were divided in three groups:

- Augmentation with Cal-CEMEX (Tecres, IT) was performed on 4 vertebrae.
- Augmentation with Mendec Spine (Tecres, IT) was performed on 4 vertebrae.
- The remaining 4 specimens act as a control group.

Destructive tests were carried out. The specimens were compressed axially in a step-wise fashion (0% with 50 N of preload, 5%, 10%, 15% and 20%). Micro-CT imaging was carried out at each step. DVC analysis (LaVision, UK) was performed on the reconstructed volumes to obtain the full-field displacement and strain distribution, in order to identify the onset and progression of bone-biomaterial failure in the augmented vertebral body.

III. RESULTS

The force and work to ultimate failure in prophylactic augmented vertebrae was consistently larger than in the controls (Fig.1). However, in some cases the first-failure force and work were lower than for the control (Fig.1). The strain distribution was investigated to elucidate the internal failure mechanism. Failure seemed to start at trabecular-cement interface, propagating throughout trabecular bone within the vertebral body (Fig.2).

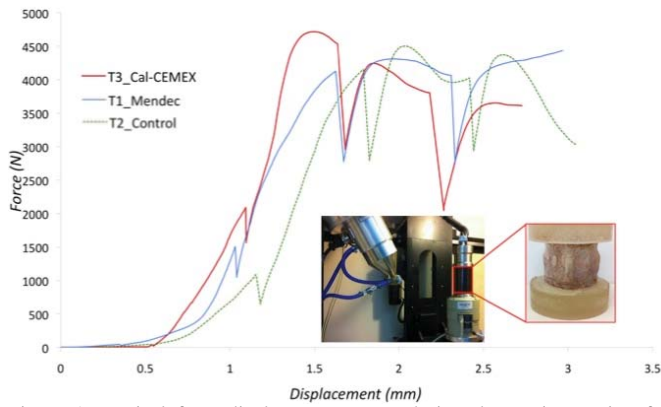


Figure 1: Typical force-displacement curve during destructive testing for augmented and control vertebrae. Each compression step is followed by a relaxation period of ~15min before imaging.

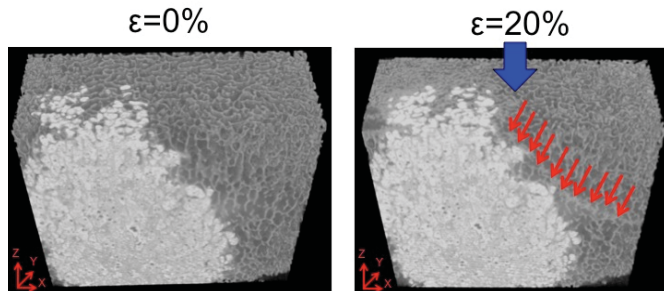


Figure 2: Internal 3D view of augmented specimen in the pre-load (0% strain) and final (20% strain) compression stages. A progressive microdamage developed from bone-cement interface and then spread across the trabecular bone. Conversely the cement region appeared to be unaffected even at the final stage. Both type of cements showed a similar trend.

IV. DISCUSSION

This study allowed a better understanding of the failure process in augmented vertebrae with different biomaterials. While in all specimens prophylactic augmentation reduced the risk of reaching ultimate failure, in some cases it increased the risk of partial failure. The variability of the mechanical performance of the treatment seems to confirm a recent study [11], in which has been hypothesized that the effect of augmentation depends on the quality of augmentation itself. Our finding suggests that the most critical region is the bone-cement interface where the onset of fracture is recognizable, consistently with [10, 12]. The failure mechanism did not seem to depend on the cement type.

ACKNOWLEDGEMENTS

The authors would like to thank the European Society of Biomechanics (ESB mobility award 2014) and the Royal Society Research Grant (RG130831).

REFERENCES

[1] WHO, *Assessment of fracture risk and its application to screening for postmenopausal osteoporosis*. Report of a WHO study group. WHO Technical Report Series, World Health Organization, Geneva, Switzerland, 843: 1-130. 1994.

[2] R.K. Wilcox, *The biomechanics of vertebroplasty: a review*. Proc Inst Mech Eng H., 218(1): p. 1-10, 2004.

[3] Pollintine, P., et al., *Time-dependent compressive deformation of the ageing spine: relevance to spinal stenosis*. Spine (Phila Pa 1976), 35(4): p. 386-94, 2010.

[4] Goel, V.K., et al., *Test Protocols for Evaluation of Spinal Implants*. Journal of Bone and Joint Surgery, 2006. 88 (suppl_2): p. 103-109.

[5] Nazarian, A. and R. Muller, *Time-lapsed microstructural imaging of bone failure behavior*. J Biomech, 2004. 37(1): p. 55-65.

[6] Buffière, J.Y., et al., *In Situ Experiments with X ray Tomography: an Attractive Tool for Experimental Mechanics*. Experimental Mechanics, 50(3): p. 289-95, 2010.

[7] Liu, L. and E.F. Morgan, *Accuracy and precision of digital volume correlation in quantifying displacements and strains in trabecular bone*. J Biomech, 2007. 40(15): p. 3516-20.

[8] A.I. Hussein, P.E. Barbone, and E.F. Morgan, *Digital Volume Correlation for Study of the Mechanics of Whole Bones*. Procedia IUTAM, 2012. 4: p. 116-125.

[9] Madi, K., et al., *Computation of full-field displacements in a scaffold implant using digital volume correlation and finite element analysis*. Med Eng Phys, 2013. 35(9): p. 1298-312.

[10] G. Tozzi, Q.-H. Zhang, J. Tong "Microdamage assessment of bone-cement interfaces under monotonic and cyclic compression", J. Biomech, vol. 47 (14): pp. 3466-3474.

[11] L. Cristofolini, N. Brandolini, V. Danesi, P. Erani, M. Viceconti, S.J. Ferguson, "Biomechanical effectiveness of prophylactic augmentation: on in vitro study" JJMB under review.

[12] G. Tozzi, Q.-H. Zhang, J. Tong, "3D real-time micromechanical compressive behaviour of bone-cement interface: experimental and finite element studies", J Biomech, vol.45: pp. 356-63.

A model-based study of the effect of intermittent pneumatic compression of limbs on the cardiovascular system

G. De Nisco¹, D. Maffiodo¹, D. Gallo¹, A. L. Audenino¹, C. Ferraresi¹, U. Morbiducci¹

¹ *Department of Mechanical and Aerospace Engineering – Politecnico di Torino, ITALY*

Abstract— In this study we use a lumped parameter model of the cardiovascular system to probe deeper into the capability of an intermittent pneumatic compression (IPC) of the lower limbs strategy, as realized by a specific device designed to support venous circulation, to improve blood circulation. The device investigated is an in-house prototype whose effect is also modelled and coupled to the lumped model of the cardiovascular system. Findings from simulations clearly show that by applying ad hoc compression strategies to the venous network of lower limbs produces an increase of venous pressures and overall, an increased cardiac output in those subject suffering from compromised venous circulation of the lower body.

Keywords— lumped parameter model, intermittent pneumatic compression, muscular pump, venous return.

I. INTRODUCTION

DURING any physical activity, the intermittent contraction of the lower limb muscles exerts an important pumping action supporting the venous return. When the muscular pump efficiency is compromised for some reason, like an injury or a specific pathology, its functionality can be restored by using intermittent pneumatic compression (IPC) devices. Fig. 1 shows an example of IPC device, it includes a given number of inflatable bladders, housed into a flexible shell, to exert a defined pressure pattern on calf and foot. The control of bladders' inflation/deflation is performed by a group of electro-pneumatic valves and a programmable controller.



Fig. 1 Prototype of IPC device

However the effectiveness of IPC devices in restoring (1) venous return and (2) the cardiac output are difficult to be assessed [1]. In this study we propose a low order model of the cardiovascular system, coupled to a model of a custom made IPC device [1] to investigate in depth its impact on the overall cardiovascular system and to identify the IPC device's effective working conditions.

II. MATERIALS AND METHODS

Here the lumped model of the entire cardiovascular system proposed by Shi and Korakianitis [2], was properly modified and *coupled* with a lumped model of the IPC device. In detail, the venous compartment of the lower body was detailed and the circulation of both legs was incorporated. More in detail, as shown in Fig. 2, the model is made of three main portions dedicated to describe heart, pulmonary and systemic loop. As for the heart, ventricles behaviour is modelled by two controlled pressure sources. The input signals, which represent intra-ventricular pressure, is related to the ventricular volume through the famous relationship

$$P(t) = P_0 + E(t) \cdot (V(t) - V_0) \quad (1)$$

where $E(t)$ is the ventricular elastance, $V(t)$ describes the ventricular volume and the values P_0 and V_0 represents the reference amounts of pressure and volume for each ventricle, respectively. The other two main compartments of the model represent pulmonary and systemic loops, where blood vessels are modelled by circuital elements: resistance (R) considers loss effects due to friction at the vessel wall; compliance (C) resembles the distensibility of the vessels; inertance (L) accounts for blood flow inertia; [3]. The pulmonary circuit of the model consists of five compartments: two RLC blocks describing pulmonary artery and medium arteries characteristics, which are distensible vessels. Two resistances model the behaviors of arterioles and capillaries, where frictional losses dominate. One RC element is used for venous vessels (in veins inertial effects are often neglected and an RC combination is sufficient to define them). The systemic loop is defined using a similar approach. As mentioned before, this part of the model needs a more detailed description, because of the need to model the interaction between the IPC device and the venous network of the lower limbs (Fig. 2). The aortic compartment is divided in ascending and descending aorta described by two RLC blocks. The model branch identifying the upper body vessels is connected downstream of the ascending aorta block. Distal to the descending aorta block, the model exhibits two branches, each one modelling the vascular network of one lower limb. These branches consist of four blocks describing medium arteries, arterioles, capillaries and veins. Venous comparts are described by RLC blocks placed between two diodes roughly mimicking the venous valves behavior. The model was implemented in Matlab-Simulink using available blocks of the *SimPowerSystem* library.

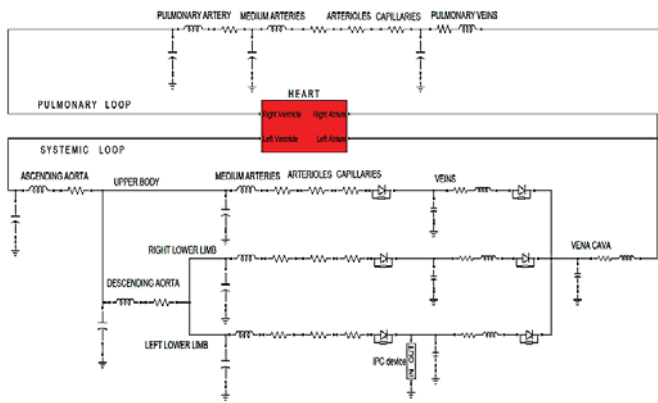


Fig. 2 Lumped model of the cardiovascular system for a subject assisted by the IPC device.

In order to properly identify the model the Simulink parameter estimation toolbox was used. In detail, by applying the nonlinear least squares optimization method using the *Trust-Region-Reflective* algorithm, a combination of parameter values was obtained which allows to replicate physiological waveform of pressure and blood flow in all the compartments of the cardiovascular system. As for the IPC device, its operating mechanism is described by a controlled voltage source, which is introduced in the branch describing left lower limb veins. The device bladders are inflated with a specific sequence: from the most distal, positioned in correspondence of the foot, to the most proximal one, on the calf. The opening of the valve controlling the pressure in a specific bladder is triggered by the achievement of the maximum pressure value in the previous one. The period of the stimulation is thirty seconds: during the first fifteen seconds, each bladder is inflated and deflated; then the stimulation is switched off for fifteen seconds. In the reduced order model the applied pressure waveform is expressed as the sum, in time, of the pressure waveforms relative to each bladder.

III. RESULTS AND DISCUSSIONS

The physiological response at rest is preliminarily evaluated with model parameters representing healthy state. This allows to check for the reliability of the overall model. Then, the systemic venous blocks of lower limbs is modified with the insertions of dissipative resistances to imitate pathological conditions of paraplegics. The effect of the device on circulation is investigated for these two simulated cases. The obtained results show that during the IPC stimulation there is an increase of venous pressure and flow rate values in the assisted lower limb. In particular, the induced rise of pressure in assisted venous network of the modeled pathological subject leads to an increase of the of the venous flow to healthy values, as shown in Fig. 3. The induced increase in venous flow rate as the obvious consequence of increasing the volume of blood flowing back to the heart. This effect is accentuated by increasing the magnitude of stimulation contact pressures. Simulation results for a stimulation of peak pressure value equal to 30kPa show that an increase of ventricular volumes,

during subject assistance, to healthy values (Fig. 4). The simulations also show that these positive effects can be kept also using two IPC devices, alternately applied to the left and to the right legs (data not shown).

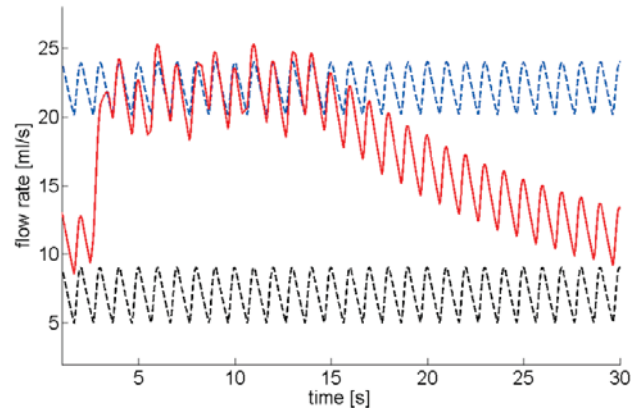


Fig. 3 Venous flow rates of the lower limb assisted by device, during the entire stimulation cycle, for healthy subject not assisted (blue dotted line), pathological subject not assisted (black dotted line) and assisted (red line).

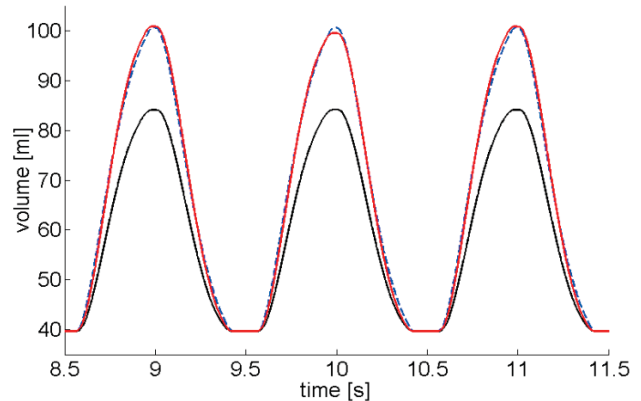


Fig. 4 Right ventricular volume waveforms: healthy subject not assisted by the device (blue dotted line); pathological subject not assisted (black line); pathological subject assisted by the device (red line).

IV. CONCLUSIONS

The herein proposed low order model of the overall circulation, adapted to simulate the action of IPC devices is a promising tool to properly set devices supporting venous circulation, being suitable for the insertion of accurate models of IPC devices. The model enriches the arsenal of tool available to (1) properly design/optimize devices for venous assistance and (2) set working conditions to supply appropriate assistance to venous return in pathologic subjects.

REFERENCES

- [1] C. Ferraresi, D. Maffiolo, and H. Hajimirzaalian, "A model-based method for the design of intermittent pneumatic compression systems acting on humans", *P I Mech Eng H*, vol.228 no.2, pp. 118-126, 2014.
- [2] Y. Shi, T. Korakianitis, "Numerical Simulation of Cardiovascular Dynamics With Left Heart Failure and In-series Pulsatile Ventricular Assist Device", *Artif Organs*, vol.30, pp.928-948, Nov. 2006.
- [3] Y. Shi, P. Lawford, and R. Hose, "Review of Zero-D and 1-D Models of Blood Flow in the Cardiovascular System", *BioMed Eng OnLine*, 2011, 10:33.

Can CT image deblurring improve strain and failure load predictions at the proximal femur?

C. Falcinelli¹, E. Schileo¹, A. Pakdel², C. Whyne² and F. Taddei¹

¹ Istituto Ortopedico Rizzoli, Bologna, Italy

² Sunnybrook Research Institute, Toronto, Canada

Abstract—The partial volume effects (PVE), that appear in the CT images as blurred edges, can lead to errors in geometry reconstruction and mechanical property assignment in CT-derived FE models and, consequently, some errors in FE predictions. The inclusion of CT image deblurring algorithm, designed to restore the pixel intensity values, in CT-based FE modelling can improve the FE predictions accuracy compared to experimental measurements.

Keywords—Subject-specific finite element models, validation, CT image deblurring, point spread function measurement.

I. INTRODUCTION

FE bone strength, derived from FE procedures validated in-vitro, has been proposed to classify osteoporotic fractures in-vivo. Our subject-specific FE modelling procedure allowed us to obtain good results not only in-vitro [1]-[2], but also in-vivo [3]. However, some limitations in our FE results remain: i) high peak errors in FE-predicted vs. experimental strain values, particularly where the cortical bone is very thin (i.e. femoral neck); ii) differences of up to 37% between experimental and FE-predicted failure loads despite high correlation between experimental and FE-predicted values ($R^2=0.89$ on 14 femurs). These discrepancies may be at least partly explained by the presence of CT artefacts, e.g. partial volume effect (PVE), which can lead to errors in both bone surface geometry and intensity.

Recently, a CT image deblurring algorithm [4], designed to restore geometry and intensity of thin bone structure, has been developed in the Orthopaedic Biomechanics Laboratory (Sunnybrook Research Institute, Toronto). The aim of the present study was to verify if the inclusion of this deblurring algorithm in the FE workflow can improve prediction accuracy of strains and failure loads at the proximal femur.

II. METHODS

Eleven fresh-frozen cadaver femora were CT scanned and tested non destructively to measure strains (7 femora tested in stance loading configuration, and 4 tested in fall loading configuration). Twelve strain gauges located on the proximal femur were used to measure the strains experimentally. Moreover, the femora, 7 in stance and 4 in fall, were also tested destructively to measure the failure loads. All experimental tests followed published procedures [5].

To employ the deblurring algorithm, first an estimate of the 3D Point Spread Function (PSF) was made for all the cadaveric femoral CT images. The PSF was then used within a deconvolution solver to minimize blurring in the digital images and restore the geometry and intensity values in the

CT image stacks. Using the deblurred CT images, FE models of proximal femur were generated as reported in [1].

The deblurred FE-predicted strains and failure loads were compared with experimental measurements and FE predicted values derived from the original CT datasets.

III. RESULTS

A. Strains

The strains results (pooled data) are reported in Table I. Strong agreement between the FE-predicted strains derived from the deblurred data and experimental strains were found, with slight improvements over the FE models derived from original CT.

TABLE I
STRAIN RESULTS

<i>Stance (7 femora)</i>	<i>Deblurred model</i>	<i>Reference model</i>
R^2	0.92	0.90
<i>Slope</i>	1.11	1.12
<i>Intercept ($\mu\epsilon$)</i>	1	5
<i>RMSE ($\mu\epsilon$)</i>	128	144
<i>RMSE %</i>	9.2	10.3
<i>Max. err. ($\mu\epsilon$)</i>	598	715
<i>Max. err. %</i>	42.8	51.2
<i>Fall (4 femora)</i>	<i>Deblurred model</i>	<i>Reference model</i>
R^2	0.92	0.91
<i>Slope</i>	1.07	1.17
<i>Intercept ($\mu\epsilon$)</i>	6	2
<i>RMSE ($\mu\epsilon$)</i>	199	241
<i>RMSE %</i>	9.0	10.9
<i>Max. err. ($\mu\epsilon$)</i>	1136	1209
<i>Max. err. %</i>	51.6	54.9

Accuracy indicators on pooled data for FE models tested in stance and fall loading configurations.

Comparing the accuracy indicators obtained in the present study and those obtained using FE models derived from original images (labeled as “reference model”), it was found that: i) the correlation slightly improved; ii) the slope was

closer to 1, particularly for fall; iii) RMSE and peak errors were also slightly reduced.

B. Failure loads

FE predictions of failure load derived from deblurred data were highly correlated with the experimental measurements (Fig. 1), with a slightly improvement in terms of R^2 over the FE models derived from original CT images. However, the standard error of the estimate (SEE) increased (1112 N in the deblurred models vs. 987 N in the reference models).

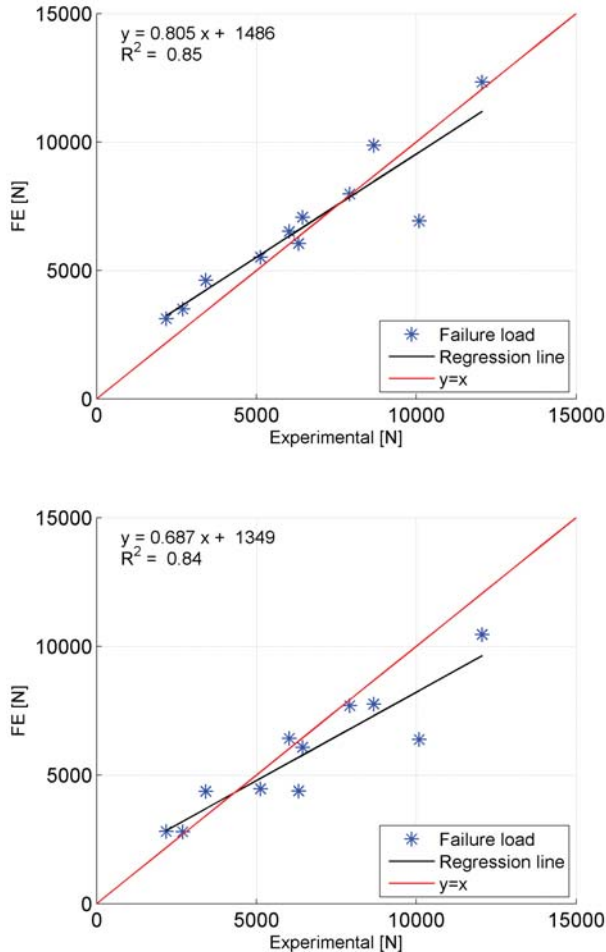


Fig. 1: Linear regression of FE predicted vs. experimentally measured failure loads for deblurred models (above) and reference models (below)

IV. CONCLUSION

Starting from deblurred CT images in which thin cortical features are better captured leads to an improvement in the FE prediction accuracy of CT based FE modelling. Incorporating other PVE reduction algorithms in addition to deblurring may extend further the benefits realized by image deblurring.

REFERENCES

- [1] E. Schileo, F. Taddei, A. Malandrino, L. Cristofolini, and M. Viceconti, "Subject-specific finite element models can accurately

- predict strain levels in long bones," *Journal of Biomechanics*, 40, 2982-2989, 2007
- [2] E. Schileo, L. Balistreri, L. Grassi, L. Cristofolini, and F. Taddei, "To what extent can linear finite element models of human femora predict failure under stance and fall loading configurations?," *Journal of Biomechanics*, 47, 3531-3538, 2014
- [3] C. Falcinelli *et al.*, "Multiple loading conditions analysis can improve the association between finite element bone strength estimates and proximal femur fractures: a preliminary study in elderly women," *Bone*, 67, 71-80, 2014
- [4] A. Pakdel, N. Robert, J. Fialkov, A. Maloul, and C. Whyne, "Generalized method for computation of true thickness and x-ray intensity information in highly blurred sub-millimeter bone features in clinical CT images," *Physics in Medicine and Biology*, 57, 8099-8116, 2012
- [5] F. Taddei, L. Cristofolini, S. Martelli, H.S. Gill, and M. Viceconti, "Subject-specific finite element models of long bones: An in vitro evaluation of the overall accuracy," *Journal of Biomechanics*, 39, 2457-2467, 2006

A computational fluid dynamics study of the Cardiatis Multilayer Flow Modulator

M. Fedele, G. Alaimo, F. Auricchio, M. Conti, E. Faggiano, S. Morganti, A. Reali.

1. DICAr, University of Pavia

Abstract. - The aim of the present work is to perform numerical simulation of the hemodynamics inside an aneurysm in presence of the Cardiatis Multilayer Flow Modulator. The results are exploited to show the benefits of the stent implantation.

I Introduction

The Cardiatis Multilayer Flow Modulator (MFM) is an uncovered, self-expanding stent made of braided cobalt-alloy wire (Phynox). Its main feature is to change the blood flow within the aneurysm, modifying turbulent to laminar flow and supporting the formation of organized, stable thrombus inside the aneurysm sac. As a consequence, the wall shear stress (WSS) is reduced protecting against the rupture. Thanks to device porosity of about 65%, another important feature consists of the ability of maintaining perfused the side branches.

The aim of the work is to quantify the benefits of this stent exploiting computational fluid dynamics (CFD). The study is divided in three tasks: medical image processing, in-vitro experiments and numerical simulations. The first two tasks are used to set the parameters of the numerical simulations. In particular, we perform a finite element analysis (FEA) in a phantom of an aneurysm and we include the stent in the fluid domain as an immersed porous surface [2].

II Methods

A. Medical Image Processing.

The dataset is composed by computed tomographies (CT) images of two patients. For each patients one CT before and one after the surgical implantation of the stent were collected. International Review Broad approval was obtained for the conduct of this study, and the board waived the need for patient consent. The images are segmented using semi-automatic method in order to extract the lumen, the stent and the aneurysm region [1]. In particular, we measure the variation of the diameter of the stent in

the region of the implantation. Indeed, this measure is related to the porosity of the stent.

B. In-vitro Experiments.

We perform in-vitro experiments to analyze the variation of pressure drop through the stent, varying its radius in the range obtained by the in-vivo analysis. This allows to quantify the porosity of the stent.

C. Numerical Method.

The stent surface is inserted in the classic Navier-Stokes equations adding a dissipative term with a resistance that can be interpreted as a penalization parameter enforcing the desired porosity. We describe the immersed surface of the stent as the zero level of a level set function defined analytically and we include it in the three-dimensional domain exploiting a smooth Dirac function. From a numerical point of view, this strategy avoids the problem of having bi-dimensional finite elements immersed in the three-dimensional domain consistent with the stent surface.

III Results

Preliminary results on WSS and on streamlines are presented. In particular, we focus on the difference between the hemodynamics with and without the stent and we prove the laminarization of the blood flow inside the aneurysm when it is employed.

IV Acknowledgement

We acknowledge doctor Giovanni Spinella of University of Genova for providing us the medical data.

References

- [1] L. Antiga, M. Piccinelli, L. Botti, B. Ene-Iordache, A. Remuzzi, and D. A. Steinman. An image-based modeling framework for patient-specific computational hemodynamics. *Medical & biological engineering & computing*, 46(11):1097–1112, 2008.
- [2] M. A. Fernández, J. F. Gerbeau, and V. Martin. Numerical simulation of blood flows through a porous interface. *ESAIM: Mathematical Modelling and Numerical Analysis*, 42(06):961–990, 2008.

Isogeometric-based Tools for the Evaluation of Carotid Artery Stent Performance

M. Ferraro ^{1,*} F. Auricchio ¹ M. Conti ¹ L. De Lorenzis ² S. Morganti ³ A. Reali ¹ R.L. Taylor ⁴

¹ DICAR Department of Civil Engineering and Architecture, Università di Pavia, 27100 Pavia, Italy

² Institute of Applied Mechanics, Braunschweig University of Technology, 38106 Braunschweig, Germany

³ DIII Department of Electrical, Computer and Biomedical Engineering, Università di Pavia, 27100 Pavia, Italy

⁴ Department of Civil and Environmental Engineering, University of California Berkeley, Berkeley, CA 94720-1710, USA

* mauro.ferraro@iusspavia.it

Abstract— Isogeometric Analysis (IgA) has recently emerged as a cost-effective alternative to classical Finite Element Analysis (FEA). Vascular biomechanics can take advantage of IgA highly accurate geometric description for both biomedical devices and biological structures. Moreover, IgA can provide a smooth description of complex phenomena, such as contact and buckling phenomena. This work aims at developing a novel computational framework based on IgA to evaluate the performance of carotid artery stents. Analyses involving large deformations, inelastic material models and frictionless contact formulation are performed within the numerical solver FEAP and its additional package for IgA. The obtained results are discussed, showing in particular the advantages of IgA in terms of accuracy and cost-effectiveness.

Keywords— Isogeometric analysis, Shape memory alloys, Carotid artery stents, surface mapping, stent implant.

I. INTRODUCTION

Computer-based procedures based on finite element analyses (FEA) are nowadays widely adopted for biomechanical analyses. The major benefit of the employment of FEA in biomechanics is the possibility to test different combinations of materials, geometries and working conditions or when the traditional experimental approach is too expensive or difficult to implement. Within this context, isogeometric analysis (IgA) [1] is rapidly emerging as a novel promising alternative in this field [2,3]. The main feature of the method consists of using typical CAD basis functions for both geometric description and variable approximation. This approach implies the ability to describe exactly the computational domain geometry throughout the analysis process, thus simplifying the mesh refinement process, and to include, at the same time, the capability to control the basis function regularity. This work is aimed at developing a novel computational framework based on IgA to evaluate the mechanical performance of commercially available carotid artery stents. In particular, analyses involving large deformations, inelastic material models and frictionless contact are performed within the numerical solver FEAP and its additional package for IgA.

II. MATERIALS AND METHODS

In this section the computational framework to obtain both IgA-suitable vessel and stent models is described. Subsequently, the constitutive models used in our study are described. Such geometrical models and constitutive laws are then integrated within an analysis setup simulating the stent

ringt implant test within a patient-specific carotid artery portion.

A. Vessel model

In order to obtain a IgA-suitable NURBS structure starting from a set of points representing the vascular geometry (Fig.1-a-b), we implemented the mapping procedure proposed by Morganti et al. [2]. A generic NURBS surface defined in \mathbb{R}^3 can be described with the following relation:

$$S(\psi, \eta) = \frac{\sum_i \sum_j N_{i,p}(\psi) M_{j,q}(\eta) B_{ij} w_{ij}}{\sum_i \sum_j N_{i,p}(\psi) M_{j,q}(\eta) w_{ij}} \quad (1)$$

where B_{ij} and w_{ij} represent the i,j -th control point coordinates and weight, respectively, and $N_{i,p}$ and $M_{j,q}$ are the i -th j -th shape functions of order p and q respectively, related to each parametric direction. Assuming constant weights, after some simple algebraic manipulations, eq. 1 can be rearranged in order to get the following matricial form

$$S_T^r = C * B_{vec}^r \quad (2)$$

where S_T^r represents the r -th cartesian nodal component of the sampling points belonging to the reference surface, B_{vec}^r is the r -th cartesian component of the control points order in vectorial form and C roughly contains the products between shape functions values in both parametric directions. It is immediate to observe that eq.2 represents a linear system which can be solved (in the least-square sense) in order to obtain the r -th component of the mapped control points.

The proposed approach is used to map a primitive cylinder with a predefined parametrization (Fig. 1-c) onto the carotid portion object of this study (Fig. 1-d).

B. Stent model

In this study we exploited a novel computational framework to interface the CAD software Rhinoceros v. 4.0 SR8 with the general purpose solver FEAP. Since no data are available from the manufacturer, the main geometrical features of such devices are derived from high-resolution micro-CT scans of the stent in the delivery system. Starting from a planar CAD geometry corresponding to the unfolding of stent, a 2D CAD surface is generated for each NURBS patch. The final stent configuration is obtained by mean of an in-house code in

Matlab and subsequently exported in a format suitable for the solver FEAP.

C. Constitutive model

The mechanical response of the shape memory alloy (SMA) needs to be considered in this study. The model proposed by Souza et al. [4] are implemented in a large displacement-small strain regime. For the vessel model we consider a Neo-Hookean model for the stenotic artery ($E=1$ MPa, $\nu=0.3$).

D. Analysis setup

This numerical test aims at investigating the interaction between a carotid stent ring and a patient-specific carotid artery portion. The knot-to-surface contact driver proposed by Dimitri et al. [5] has been employed. We perform a two-step simulation procedure; The first step corresponds to the crimping simulation, i.e., the diameter of the stent is decreased simulating the loading phase of the stent into the delivery system. Subsequently, the catheter expands again in order to place the stent into the target lesion.

III. RESULTS AND DISCUSSION

The contour plots of displacement and Von Mises distributions for both vessel and stent are depicted in Fig. 2. This preliminary analysis confirms the results obtained by Auricchio et al. [6]. The benefits of IgA arise both in computational time and geometrical accuracy.

As example, the crimping phase for the stent ring employed only 2 minutes to be completed while the FEA counterpart employed more than 8 minutes with the same hardware and software architecture.

Moreover, the high-order and high-regularity of NURBS functions allows to represent the vessel geometry, for a given geometrical accuracy, with a reduced number of degrees of freedom with respect to classical FEA (over one order of magnitude in this simple example).

ACKNOWLEDGEMENT

This work is supported by the European Research Council through the FP7 Ideas Starting Grant project no. 259229, by the Cariplo Foundation through the Project iCardio- Cloud no. 2013-1179, by Regione Lombardia through the Project no. E18F13000030007, and by the Ministero dell' Istruzione, dell' Università e della Ricerca through the Project no. 2010BFXRHS.

REFERENCES

- [1] Cottrell, J.A., Hughes, T.J.R., Bazilevs, Y. *Isogeometric Analysis. Towards integration of CAD and FEA*. Wiley, 2009.
- [2] Morganti, S., Auricchio, F., Benson, D. J., Gambarin, F. I., Hartmann, S., Hughes, T. J. R., & Reali, A. Patient-specific isogeometric structural analysis of aortic valve closure. *Computer Methods in Applied Mechanics and Engineering*, 284, 508-520, 2015.
- [3] Auricchio, F., Conti, M., Ferraro, M., Morganti, S., Reali, A., Taylor, R.L. Innovative and efficient stent flexibility simulations based on Isogeometric Analysis, submitted, 2015.
- [4] Souza, A. C., Mamiya, E. N., & Zouain, N. (1998). Three-dimensional model for solids undergoing stress-induced phase transformations. *European Journal of Mechanics-A/Solids*, 17(5), 789-806.
- [5] Dimitri, R., De Lorenzis, L., Scott, M. A., Wriggers, P., Taylor, R. L., & Zavarise, G. (2014). Isogeometric large deformation frictionless contact using T-splines. *Computer methods in applied mechanics and engineering*, 269, 394-414.
- [6] Auricchio, F., Conti, M., Morganti, S., & Reali, A. Shape memory alloy: from constitutive modeling to finite element analysis of stent deployment. *Computer Modeling in Engineering and Sciences* 57(3), 225, 2011.

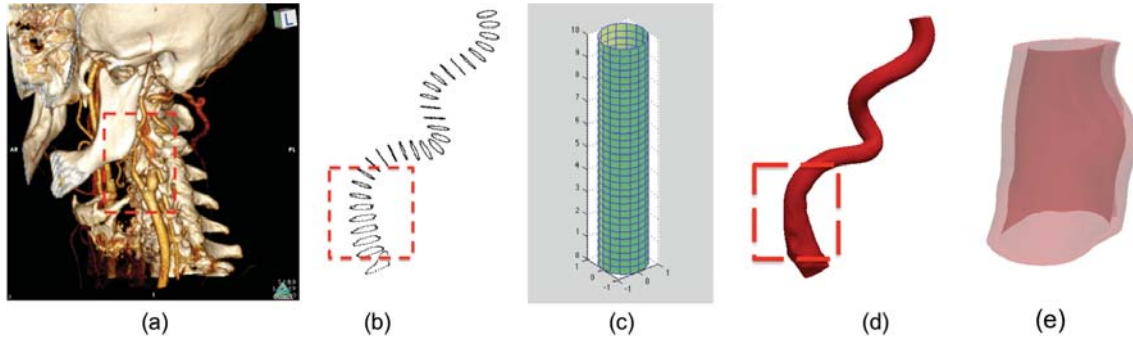


Figure 1. NURBS-based surface mapping: 3D volumetric reconstruction from CTA images (a); sampled sections (b); primitive surface (c); mapped IgA surface (d); IgA solid model of the carotid artery portion object of the present study (e).

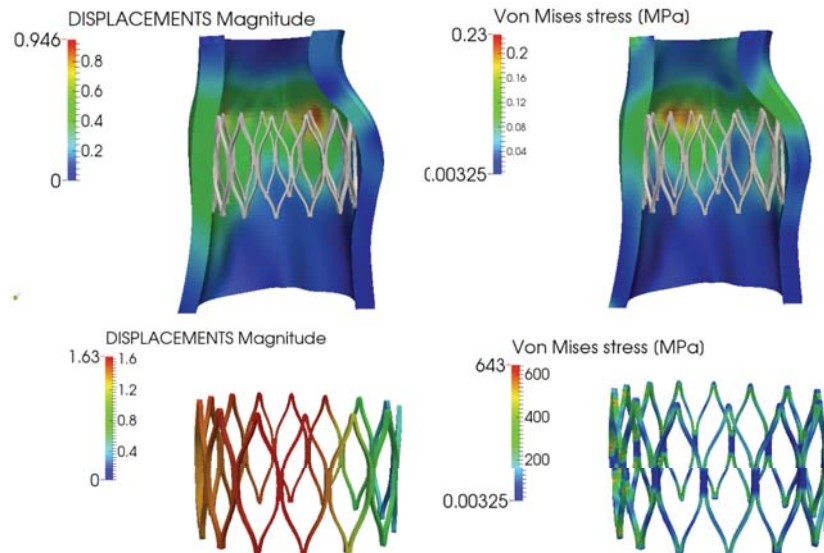


Figure 2. Stent ring implant contour plot: vessel (up) and stent (down) displacement and Von Mises stress contour plots.

Evaluation of fluid-dynamics and oxygen consumption in a porous scaffold stimulated by cyclic squeeze pressure

M. Ferroni¹, S. Giusti², G. Spatafora¹, F. Boschetti¹ and A. Ahluwalia²

¹ LaBS, Chemistry Materials and Chemical Engineering Department "Giulio Natta", Politecnico di Milano, Italy

² Research Center E. Piaggio, University of Pisa, Italy

Abstract—In tissue engineering, the architecture and dynamic physical environment of tissues is recreated by combining 3D scaffolds and bioreactors able to apply controlled mechanical stimuli on the cells. In this work, we present a new approach for optimizing Computational Fluid-Dynamic (CFD) models for the study of the fluid-induced forces generated by a Sensorized Squeeze Pressure bioreactor (S²PR) within a porous cryogel, coupled with oxygen consumption of cardiac cells. Results reported a general improvement of tissue growth stimulated by S²PR if compared to static culture conditions.

Keywords—CFD models, bioreactor, cardiac tissue engineering, fluid-structure interaction.

I. INTRODUCTION

CURRENT tissue engineering strategies are aimed at in-vitro recapitulation of the mechanical and the biochemical context of the physiological environment, in term of both tissue architecture and physical stimuli [1]. In this context, the use of bioreactors in combination to 3D constructs is fundamental for recreating the physiological milieu with exchange of nutrients and metabolites [2], [3]. Several studies have demonstrated the role of mechanical forces and fluid motion on the organization and function of cardiomyocytes, improving the nutrient transport and inducing cytoskeletal re-organization [4]. Previous studies have shown that a fluid-dynamic environment can be represented using time-invariant CFD models, in order to quantify the fluid-structure interactions applied to the cells or the transport of nutrients promoted by fluid motions [5]-[8].

In this work, we present a new approach for implementing time-dependent CFD models of the hydrodynamic stimulus generated by the Sensorized Squeeze Pressure bioreactor (S²PR). The entire model, consisting in a 2D macro-scaled model and 3D micro-scaled models of gelatin porous cryogel, was implemented to evaluate the oxygen transport and consumption and the shear stresses acting on the seeded cardiomyocytes. [9].

II. MATERIALS & METHODS

A. The S²PR bioreactor

The S²PR is an innovative stimulation chamber, provided with a force and position sensor, which imposes a cyclic and contactless overpressure on cell cultures, using a vertical piston movement [9]. It assures high precision and control of the piston movement with an accuracy of 5 μm . The force

sensor (Flexiforce A201, Tekscan, Inc. MA, USA) is placed under the sample brace in order to detect any contact between the piston and the scaffold (Figure 1.A).

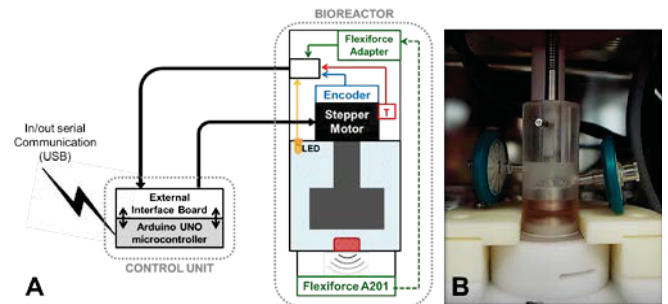


Figure 1: A) Block diagram of the architecture of the S²PR. B) A detail of the S²PR bioreactor chamber and support base.

B. Gelatin Cryogel

Porous cryogels were fabricated using the freeze-dry method from gelatin 5% w/v in deionized water, chemically cross-linked with glutaraldehyde 100 mM. Gelatin cryogels have been characterized in an aqueous environment, pointing out average values of porosity (90%), permeability ($13 \times 10^{-12} \text{ m}^2$) and elastic modulus (12 kPa). MicroCT images of the material have been used to estimate the average fiber thickness (50 μm) and the average pore diameter (150 μm). Cell cultures show high viability of cells after 24 h in the S²PR, with results comparable to static control.

C. Computational Model

Computational models were implemented using Comsol Multiphysics (COMSOL Inc., Burlington, MA, USA). Fluid-dynamics of the entire system is evaluated using the same conditions as in [9]. Time-dependent 2D models of the transverse section of the bioreactor chamber were first realized to evaluate pressure and velocity profiles around the construct due to the piston motion. In order to reproduce the fluid-dynamic conditions of the S²PR stimulus, three different physics modes were implemented: i) Navier-Stokes equations for an incompressible fluid to describe the laminar fluid flow in the bioreactor chamber, ii) Brinkman equations to characterize the flow in the porous scaffold, iii) the Arbitrary Lagrangian-Eulerian (ALE) method to model the piston motion. The scaffold domain was defined using the porosity and permeability previously reported for gelatin cryogels.

Fluid-dynamic results from the 2D models were applied to an idealized 3D geometry of the porous scaffold [7] to evaluate: i) the oxygen consumption and transport within the construct, ii) shear stresses inside the 3D structure considering the fluid-structure interaction. We implemented the diffusion and convection of the gas as well as the cell consumption, comparing both the static (3D-OCS model) and dynamic (3D-OCD model) conditions during the stimulation. Oxygen consumption follows a Michaelis-Menten kinetics and is referred to cells with surface density of 3×10^4 cells/cm². The importance of the fluid-structure interaction on the evaluation of the effective shear stress, acting on the seeded cells, was investigated implementing a fluid-structure interaction model (3D-FSI), compared to an identical 3D model in terms of geometry with the only characterization of the fluid environment (3D-LF).

III. RESULTS

The results of 2D model permit the analysis of flow around the scaffold at specific time-points and the evaluation of pressure and flow velocity at specific time-points. Pressure profiles were exported from the 2D model and used as inlet boundary conditions for the 3D models. Figure 6 reports the oxygen concentration after 200 seconds of simulation both in the absence and in the presence of the hydrodynamic stimulus and underlines the difference in oxygen concentration between the dynamic and static case.

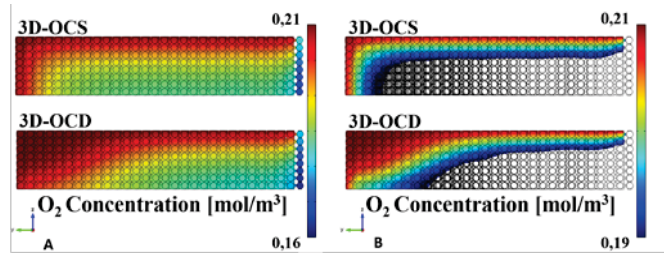


Figure 2: A) Oxygen concentration distribution after 200 seconds of simulation in 3D-OCS (on the top) and 3D-OCD (on the bottom) models. B) Underlining of the higher oxygen concentration area in the 3D-OCD model.

The 3D-FSI model confirms the accuracy of the cyclic stimulation induced by the S²PR bioreactor in terms of shear stress evaluated at the solid-fluid interface, demonstrating that stimuli are able to develop an engineered tissue without compromising cell vitality (0.1 Pa).

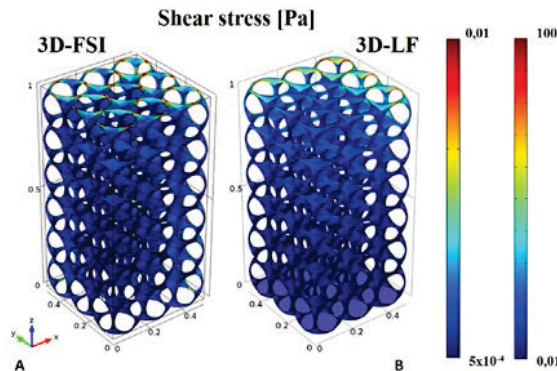


Figure 2: Shear stresses exported from 3D-FSI (A) and 3D-LF (B) models.

IV. CONCLUSION

The results of the 2D axial symmetric models highlighted the importance of characterizing fluid-dynamics and time-dependent movement of the piston in the presence of porous cryogel, even considering just the macro-properties of the scaffold, underlining that the fluid changes its direction and velocity according to the piston motion. Model in static condition (3D-OCS) was developed to confirm that the hydrodynamic stimuli used as inlet in 3D-OCD model permit a higher viability of cells after 24 hours in the S²PR bioreactor and a better transport of nutrients, in particular in the external part of the structure (Figure 2.A). The oxygen concentration increases in the dynamic case but only where the porous structure is adequately perfused by the culture medium. These results are confirmed by the 3D-FSI model, so the highest shear stress values are in the upper area of the scaffold, where the medium is forced to enter inside the scaffold. They are under the harmful value of cell vitality of about 0.1 Pa [10] and demonstrate the need to implement a fluid-structure interaction model (Figure 3). Computational models confirm the experimental results, obtained by cell cultures, and could be used as further feedback to improve S²PR bioreactor functioning.

ACKNOWLEDGEMENT

The study was co-funded by the Italian Ministry of Education, University & Research (MIUR) (Project PRIN 2010, MIND).

REFERENCES

- [1] W. L. Grayson, T. P. Martens, G. M. Eng, M. Radisic, and G. Vunjak-Novakovic, "Biomimetic approach to tissue engineering," *Seminars in cell & developmental biology*, vol. 20(6), pp. 665–673, August 2009.
- [2] I. Martin, D. Wendt, and M. Heberer, "The role of bioreactors in tissue engineering," *Trends in Biotechnology*, vol. 22(2), pp. 80–86, 2004.
- [3] G. Mattei, S. Giusti, and A. Ahluwalia, "Design Criteria for Generating Physiologically Relevant In Vitro Models in Bioreactors," *Processes*, vol. 2(3), pp. 548–569, July 2014.
- [4] M. Shachar, N. Benishti, and S. Cohen, "Effects of mechanical stimulation induced by compression and medium perfusion on cardiac tissue engineering," *Biotechnology progress*, vol. 28(6), pp. 1551–1559, October 2012.
- [5] M. Cioffi, F. Boschetti, M. T. Raimondi, and G. Dubini, "Modeling evaluation of the fluid-dynamic microenvironment in tissue-engineered constructs: a micro-CT based model," *Biotechnology and bioengineering*, vol. 93(3), pp. 500–510, March 2006.
- [6] M. Cioffi *et al.*, "Computational evaluation of oxygen and shear stress distributions in 3D perfusion culture systems: macro-scale and micro-structured models," *Journal of biomechanics*, vol. 41(14), pp. 2918–2925, October 2008.
- [7] F. Boschetti, M. T. Raimondi, F. Migliavacca, and G. Dubini, "Prediction of the micro-fluid dynamic environment imposed to three-dimensional engineered cell systems in bioreactors," *Journal of biomechanics*, vol. 39(3), pp. 418–425, January 2006.
- [8] A. Lesman, Y. Blinder, and S. Levenberg, "Modeling of flow-induced shear stress applied on 3D cellular scaffolds: Implications for vascular tissue engineering," *Biotechnology and bioengineering*, 105(3), pp. 645–654, February 2010.
- [9] C. De Maria, S. Giusti, D. Mazzei, A. Crawford, and A. Ahluwalia, "Squeeze pressure bioreactor: a hydrodynamic bioreactor for noncontact stimulation of cartilage constructs," *Tissue engineering. Part C, Methods*, 17(7), pp. 757–764, July 2011.
- [10] M. A. Brown, "Pulsatile Perfusion Bioreactor for Cardiac Tissue Engineering," *Biotechnol. Prog.*, 24(4), pp. 907–920, 2008.

Preclinical evaluation of posterior spine stabilization devices: how close are we?

Luigi La Barbera^{1,2}, Fabio Galbusera² and Tomaso Villa^{1,2}

¹ LaBS, Department of Chemistry, Materials and Chemical Engineering "G. Natta", Politecnico di Milano, Milano, Italy

² IRCCS Istituto Ortopedico Galeazzi, 20161, Milano, Italy.

Abstract—Few standards are currently available to assess the mechanical reliability of posterior spine stabilization implants. Despite their overall features and the loading mechanism is similar, they differ both in terms of the load to be applied and on the anterior support stiffness, making difficult to compare the results obtained with different procedures. The aim of this study is to compare the internal loads arising in a posterior stabilization device tested according to the current standard, with those arising on an instrumented lumbar segment during simple everyday life activities. Attention should be paid in adjusting the force applied on constructs based on different anterior support stiffnesses, this would make results comparable and easy to interpret with respect to *in vivo* loads.

Keywords— Spine stabilization, standard, ASTM F1717, ISO 12189.

I. INTRODUCTION

THE current international standards useful for the preclinical evaluation of the mechanical reliability of posterior spine stabilization devices are based on many simplifications. ASTM F1717 [1] proposes a *worst case* vertebrectomy model, where the user has to determine the maximum load to reach the run out number of cycles (5 Mcycles). ISO 12189 recommends an instrumented physiological condition [2], where three calibrated springs mimic the compressive behaviour of the intervertebral disc, and a maximum load of 2 kN has to be applied up to run out. These configurations should catch the most important loading mechanism and values occurring during clinical use, ensuring the comparability of the test results. However, issues arise when comparing the results of different spinal implants tested according to different procedures. In fact, the available scenarios differ both in terms of the load to be applied and the anterior support stiffness, obviously affecting the internal load shared by the implant and finally the outcome.

In order to guarantee the comparability of the result, any variation in the anterior support stiffness would require a variation of the load to be applied during testing. Moreover, the internal loads applied to the implant during testing should reproduce *in vivo* clinical use.

The aim of this study is: to investigate the internal loads arising in a posterior stabilization device tested according to the current standards; to study the same internal loads arising during simple everyday life activities in a more realistic L2-L4 instrumented spinal segment. The results will be discussed both in terms of comparability of the testing conditions (i.e. same internal loads), as well as their significance with respect to the effective clinical use of the implant.

II. MATERIAL AND METHODS

A. FE of ASTM F1717 and ISO 12189

FE models representing ASTM F1717 [1] and ISO 12189 [2] experimental setups were built assuming a simplified implant design [3]. The anterior support stiffness (K_A) was varied simulating different calibrated springs among the values allowed by ISO (Figure 1). A “bridge” stabilization model was also considered for ISO model. A vertical load up to 2 kN was applied. The simulations were validated by comparing the strains calculated on the rods with those measured through strain gauges rosettes during experimental tests in the same conditions.

B. Simulated clinical scenarios

The same spinal implant was virtually mounted in an intact L2-L4 FE model already validated [4]. Different clinical scenarios were considered (Figure 1): bilevel posterior stabilization, bilevel “bridge” stabilization, vertebrectomy of L3, anterior cage support (following vertebrectomy at L3). Simple everyday life activities were considered, reproducing standing (Follower Load: 500 N), and upper body flexion (FL: 1125 N, bending moment in flexion: -7.5 Nm) according to Rohlmann and colleagues [5]. A preliminary validation of these models was achieved by comparison of the internal loads measured on the rod *in vitro* and *in vivo* [6]-[7].

All simulations were run in Abaqus 6.11. For each model reproducing both the standards and the clinical scenarios, the internal loads arising in the implant were calculated.

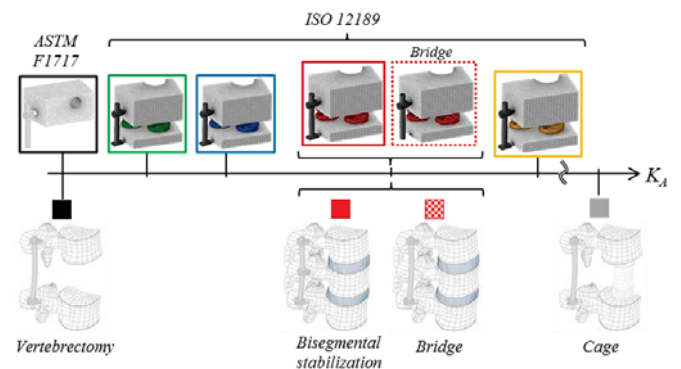


Figure 1: FE models representative of the current standards (top). Simulated clinical scenarios coupled to posterior spinal stabilization of a L2-L4 spine segment (bottom). Notice that the anterior support stiffness (K_A) increases moving from the left to the right.

III. RESULTS AND DISCUSSION

The experimental strain measurements validated the simulations reproducing ASTM F1717 and ISO 12189 standards set-up conditions [8]. Moreover, results in terms of the internal loads on the spinal rod for each simulated clinical scenario are in good agreement both with *in vitro* and *in vivo* data (Figure 2).

Some key points can be highlighted:

- (i) The anterior support stiffness detrimentally affects the internal loads, and thus the stress values on the spinal implant.
- (ii) Upper body flexion is the activity leading to the highest stress, with values 3 times higher than during standing.
- (iii) The experimental procedure recommended by ISO reproduces quite well a physiological scenario during flexion of the upper body, while it leads to values more than 2.5 higher than those predicted in standing.
- (iv) Vertebroectomy assumption leads to the highest stress values.

Obviously, as the anterior support stiffness used during testing is changed, a modification in the applied force is needed in order to achieve comparable conditions. In this light, when using the vertebroectomy model proposed by ASTM F1717, a vertical force of 220 N would allow to have the same internal loads arising in an ISO 12189 experimental construct loaded at 2 kN.

Moreover, the graphs here reported allow for determining a direct comparison between the loading condition applied to any construct (e.g. different anterior support stiffness) and the actual loads arising *in vivo* for different everyday life activities (Figure 2). For instance, when using ASTM F1717 set-up, a vertical load of about 105 N would be enough to reproduce standing in a more realistic clinical scenario, while 220 N allows to represent upper-body flexion.

IV. CONCLUSION

The current international standards allow to test posterior spine stabilization devices in controlled testing conditions, which may potentially represent clinically relevant scenarios. When testing whatever posterior spinal implant, care should be taken in selecting the proper anterior support stiffness and to adjust consequently the vertical applied load.

Any designer should be aware of this aspects, in order to ensure the comparability of the results, as well as to interpret it against available *in vivo* measurements.

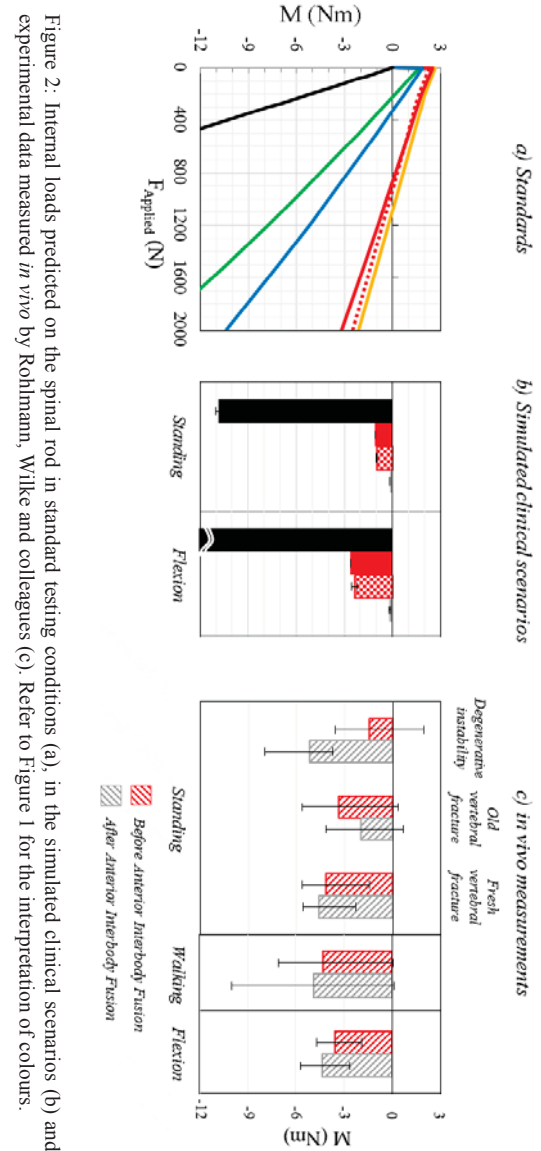


Figure 2: Internal loads predicted on the spinal rod in standard testing conditions (a), in the simulated clinical scenarios (b) and experimental data measured *in vivo* by Rohmann, Wilke and colleagues (c). Refer to Figure 1 for the interpretation of colours.

REFERENCES

- [1] ASTM Standard. F1717: Standard test methods for spinal implant constructs in a vertebroectomy model. 1st edition in 1997 (updated on 2014).
- [2] ISO Standard 12189: Implants for surgery - Mechanical testing of implantable spinal devices - Fatigue test method for spinal implant assemblies using an anterior support. 2008.
- [3] L. La Barbera, F. Galbusera, T. Villa, H.J. Wilke, ASTM F1717 standard for the preclinical evaluation of posterior spinal fixators: Can we improve it? Proc Inst Mech Eng H, 228(10):1014-26. 2015.
- [4] F. Galbusera, C. Bellini, F. Anasetti, C. Ciavarro, A. Lovi, M. Brayda-Bruno. Rigid and flexible spinal stabilization devices: a biomechanical comparison. Med Eng Phys, 33(4):490-6. 2011.
- [5] A. Rohlmann, T. Zander, G. Bergmann, H. Boustani. (2012). Optimal stiffness of a pedicle-screw-based motion preservation implant for the lumbar spine. Europ Spine J, 21:666-73. 2012.
- [6] A. Rohlmann, G. Bergmann, F. Graichen, U. Weber. Comparison of loads on internal spinal fixation devices measured *in vitro* and *in vivo*. Med Eng Phys, 19(6):539-46. 1997.
- [7] H.J. Wilke, A. Rohlmann, S. Neller, M. Schultheiss, G. Bergmann, F. Graichen, L. Claes. Is it possible to simulate physiologic loading conditions by applying pure moments? a comparison of In Vivo and In Vitro load components in an internal fixator. Spine, 26(6):636-642. 2001.
- [8] L. La Barbera. Preclinical evaluation of posterior spinal fixators - Critical assessment of the current international standards and suggestions for improvement. PhD Thesis. 2015.

A virtually-assisted variable-stiffness device for upper-limb rehabilitation

M. Malosio^{1,2}, S. Arlati¹, M. Caimmi^{1,2}, T. Dinon¹, L. Fontana¹, A. Prini¹, S. Mottura¹, C. Redaelli¹,
A. Zangiacomi¹, M. Sacco¹, L. Molinari Tosatti¹

¹ *Inst. of Industrial Technologies and Automation, National Research Council of Italy, Via Bassini 15, Milano, Italy*

² *University of Brescia, Via Branze 38, Brescia, Italy*

Abstract—This paper presents VA-LINarm, a virtually-assisted variable-stiffness device for at-home robotic upper-limb neurorehabilitation. By exploiting peculiar aspects of variable-stiffness actuators, it features functionalities widely addressed by devices specifically designed for assisted rehabilitation as controlled motion, force feedback and safety, together with the low-cost requirement for a widespread installation at patients' home. The device is interfaced to a software application in charge of supporting the patient in performing rehabilitation exercises through a virtual assistant, who emphasizes the parts of the body that have wrong posture, communicating warning, motivation, acknowledgement or congratulation to the patient.

Keywords— Upper-limb neurorehabilitation, Low-cost robotic device, Virtual reality, Rehabilitation at home.

I. INTRODUCTION

NEUROREHABILITATION can take advantage of robotic devices coupled with interactive virtual reality environments designed to assist the patient and the medical personnel during the recovery. Specifically designed robots can partially relieve therapists' physical effort during therapies, make patients independent during exercises, optimize therapist's availability during parallel rehabilitation sessions and make motor function assessments objective, while the virtual reality application can address the patient's attention, engagement and focus on the self. Neurological patients typically benefit of a period of hospitalization in the first weeks after the event, during the acute and part of the sub-acute period, in which neuroplasticity allows the best rehabilitation recovery results. However, experimental studies show that the rehabilitation training is relevant even in the chronic phase, after the discharge [1][2][3]. Some clinics can afford the purchase of expensive and complex devices, but these same aspects make them unsuitable for installation and use in the majority of rehabilitation centers and at patients' homes. The development of widely affordable devices and systems represents a breakthrough solution to increase the quality of recovery for a number of neurologically impaired people. Different upper-limb home rehabilitation devices are currently available, but they are typically passive or passively gravity-balanced [4]. Within this framework the VA-LINarm is being developed (Fig. 1), a system made up of a low-cost robotic variable-stiffness device for the rehabilitation of the upper limb, namely LINarm [5], interfaced to digital environment, provided with a virtual assistant (VA), aimed at correcting, motivating and increasing the patient's engagement [6].

II. SYSTEM DESCRIPTION

A. LINarm mechatronic device

The LINarm device [5] has been designed taking into account both functional and low-cost requirements, in order to actually realize an affordable device, both from the mechanical and the electrical point of view, minimizing material, production and assembly costs. It is based on a Variable Stiffness Actuation (VSA) scheme [7] leading to obtain a set of precious features for an affordable robotic system to execute neurorehabilitation at the patient's home:

- adjustable stiffness requiring neither force sensors nor transmission backdrivability;
- force estimation by position sensors (e.g. potentiometers), typically cheaper than force sensors, being known the spring characteristic;
- suitability for a direct interaction with human beings since intrinsic mechanical compliance avoids high impulsive forces in case of malfunctioning or undesired movements.

The end effector is equipped by interchangeable ergonomic handles to guarantee a firm and comfortable grasp by the patient. Some mechanical components are specifically designed to be fabricated in plastic and 3D-printed. Printing techniques will in fact facilitate the production and distribution of small-medium production lots of the LINarm during its multicenter evaluation and initial commercialization phase, making also possible the auto-production of the device.

The control system is implemented in an Arduino-Due microcontroller board in charge of closing control loops in real time realizing an affordable control solution.

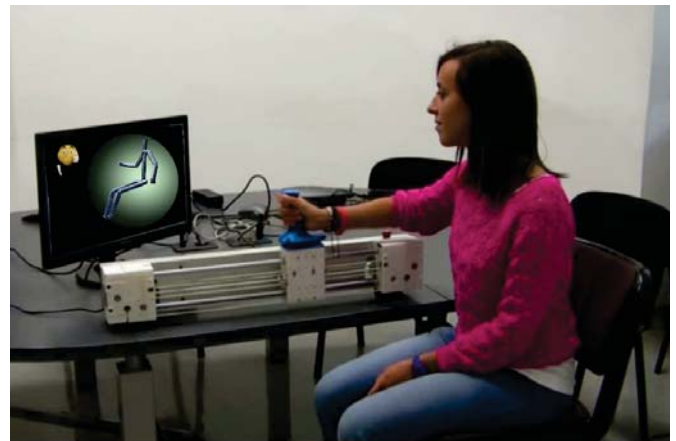


Fig. 1 – VA-LINarm, the virtually-assisted variable-stiffness device for upper-limb rehabilitation



Fig. 2 – The LINarm device

In conclusion, it is a low-cost device to perform linear rehabilitation exercises of the human arm, hence the name, exploiting peculiar features of VSA, allowing linear rehabilitation movements along different directions, as reaching and hand-to-mouth [8], according to its installation setup.

B. Virtual clinical assistant

The virtual part of the system consists in a software application, called ReAPP, that provides a graphical user interface (GUI) designed according to the needs that post-stroke patients undergoing a robotic therapy highlighted when inquired with an appropriate questionnaire [9]. The system is composed by a screen placed in front of the patients, audio-speakers and a low-cost sensor for real-time tracking of body segments position (Microsoft Kinect v2).

As already said, the main goal of ReAPP application is to motivate and engage the patients and correct their wrong behaviours [10]. To this aim, the ReAPP is interfaced in realtime with the sensing devices (Kinect and LINarm) and estimates the performance of the patient during the exercises. A set of audio and visual elements, that are meaningful for the patients' understanding of performance, is used as communication channel with the patient.

A 3D avatar reproduces in real time all the patients' movements, allowing them to know their body segments positions in each instant of the rehabilitation session. The avatar can also be set up to provide a simple visual feedback when a patient commits a postural error. The interested area on the avatar, in fact, may be highlighted to communicate that a specific body part is currently out of the optimal trajectory pre-defined by the physical therapist. ReAPP also provides the possibility to record and replay the avatar movements during the session (or a part of it) allowing the patients to see what kind of errors they made and thus increase the possibility of correcting them [11].

Another important element of ReAPP is the virtual assistant. It is an animated and expressive character, which partially replaces the real physical therapist interventions. During the exercise, it intervenes either to signal a repeated error, giving a precise suggestion about how to correct it, or to motivate and encourage the patients after a successful repetition series of the task. The VA also inquires the patients before and after the therapy to collect some information about their mood, their feelings toward the therapy and their self-evaluation of the performance [12].

Finally, since the LINarm device provides an estimation of the force that the patients exert on the handle, an indicator,

similar to a gauge indicator, is shown on the GUI to communicate this information to the patient. Depending on the chosen exercise, it signals to the patients if they are doing well, or pushing too much, if they are passive or if they are making an unconscious resistance to the handle movement.

III. CONCLUSION

VA-LINarm is a device for upper-limb rehabilitation featuring force-feedback and variable-stiffness actuation, interfaced to virtual assistant enabling the patient to execute rehabilitation therapies partially independently at home. An improved and refined version of the mechatronic device will soon be developed in the LINarm++ European project, integrating additional sensors to constantly monitor the physiological state of the patient, integrating the possibility to adapt interactively the rehabilitation therapy to the actual capabilities of the patient.

ACKNOWLEDGEMENT

This work was partially supported by the Italian Lombardy region within the RIPRENDO@home project.

REFERENCES

- [1] N. Hogan and H. I. Krebs, "Interactive robots for neuro-rehabilitation," *Restor. Neurol. Neurosci.*, vol. 22, no. 3-5, pp. 349–358, 2004.
- [2] S. Mazzoleni, P. Sale, M. Tiboni, M. Franceschini, M. C. Carrozza, and F. Posteraro, "Upper limb robot-assisted therapy in chronic and subacute stroke patients: a kinematic analysis," *Am J Phys Med Rehabil*, vol. 92, pp. 26–37, Oct 2013.
- [3] R. Colombo, I. Sterpi, A. Mazzone, C. Delconte, and F. Pisano, "Robot-aided neurorehabilitation in sub-acute and chronic stroke: does spontaneous recovery have a limited impact on outcome?," *NeuroRehabilitation*, vol. 33, pp. 621–629, Jan 2013.
- [4] A. Prochazka, "Passive devices for upper limb training," in *Neurorehabilitation Technology*, pp. 159–171, Springer, 2012.
- [5] Malosio, M.; Caimmi, M.; Legnani, G.; Tosatti, L.M., "LINarm: a low-cost variable stiffness device for upper-limb rehabilitation," *Intelligent Robots and Systems (IROS 2014), 2014 IEEE/RSJ International Conference on*, vol., no., pp.3598,3603, 14-18 Sept. 2014
- [6] Mottura, S.; Arlati, S.; Fontana, L.; Sacco, M., "Enhancing awareness and personification by virtual reality and multimedia means in post-stroke patients during rehabilitation," *5th IEEE CogInfoCom Conference on*, vol., no., pp.179,184, 5-7 Nov. 2014
- [7] B. Vanderborght, A. Albu-Schaeffer, A. Bicchi, E. Burdet, D. G. Caldwell, R. Carloni, M. Catalano, O. Eiberger, W. Friedl, G. Ganesh, M. Garabini, M. Grebenstein, G. Grioli, S. Haddadin, H. Hoppner, A. Jafari, M. Laffranchi, D. Lefeber, F. Petit, S. Stramigioli, N. Tsagarakis, M. Van Damme, R. Van Ham, L. C. Visser, and S. Wolf, "Variable impedance actuators: A review," *Robot. Auton. Syst.*, vol. 61, pp. 1601–1614, Dec. 2013.
- [8] Caimmi, M.; Guanziroli, E.; Malosio, M.; Pedrocchi, N.; Vicentini, F.; Tosatti, L.M.; Molteni F., "Normative Data for an Instrumental Assessment of the upper-limb functionality," *BioMed Research International*, In press, <http://www.hindawi.com/journals/bmri/aip/484131/>
- [9] Zangiacomi A.; Redaelli C.; Valentini F.; Bernardelli G.; "Design of interaction in a Virtual Environment for post-stroke rehabilitation: a cognitive perspective," in *5th IEEE CogInfoCom Conference*, Vietri sul Mare, Italy, 2014.
- [10] Novak D.; Nagke A.; Keller U.; Riener R.; "Increasing motivation in robot-aided arm rehabilitation with competitive and cooperative gameplay," *J Neuroeng Rehabil*, vol. 11, no. 64, 2014.
- [11] Schwann S.; Riempp R.; "The cognitive benefits of interactive videos: learning to tie nautical knots", *Learning and Instruction*, vol.14, pp. 293-305, 2004.
- [12] Koenig, A.; Omlin, X.; Zimmerli, L.; Sapa, M.; Krewer, C.; Bollinger, M.; Müller, F.; Riener, R.; "Psychological state estimation from physiological recordings during robot-assisted gait rehabilitation", *J Rehabil Res Dev*, vol. 48, no. 4, pp. 367 - 385, 2011.

Homogenization methods for the multiscale constitutive description of soft connective tissues

Michele Marino and Peter Wriggers

*Institute of Continuum Mechanics, Leibniz Universität Hannover,
Appelstr. 11, 30167 Hannover, Germany. E-mail: marino@ikm.uni-hannover.de*

Abstract—In this paper, the mechanics of soft tissues is modeled by describing tissue structured hierarchical arrangement and reducing model complexity by means of multiscale homogenization techniques. Such an approach is referred to as a structural multiscale method. It consists in regarding the tissue at the macroscale as a fiber-reinforced composite material, wherein properties of reinforcement phase are recovered by coupling mechanical models at different length scales by means of consistent inter-scale relationships. Accordingly, the equivalent responses of tissue substructures at different scales, including possible damage and inelastic mechanisms are analytically derived and consistently integrated and upscaled, allowing to include at the macroscale the dominant mechanisms occurring at smaller scales.

Keywords—Biomechanics of soft tissues, Homogenization methods, Structural multiscale approach.

I. INTRODUCTION

SOFT collagenous tissues share a peculiar histological structure, characterized by a hierarchical organization from the nanoscale (molecules) up to the microscale (crimped periodic fibers). The mechanical behaviour of collagenous tissues affects a number of both micro (e.g., mechano-regulated tissue remodelling) and macro (e.g., mechanics of joints or vessels) physiological systems. Moreover, many physiopathological processes, which are strictly related to experimentally observable histological or biochemical alterations, affect collagenous tissues mechanics and, therefore, the functional role of a number of anatomical structures (e.g., joints or blood vessels). For instance, joint hypermobility, higher risk of vascular rupture, as well as aneurismatic development have been observed in association with a reduction of collagen content or an alteration of collagen cross-linking properties. Accordingly, modeling the mechanical behaviour of collagenous tissues (such as arterial wall, [1]) is a challenging open problem. The choice of a multiscale approach, based on tissue structure, enables to analyze macroscopic effects as a function of diseased histological features at different scales, [2], [3].

II. METHODS

Crimped collagen fibers own a non-linear mechanical behaviour due to their geometric arrangement as well as to molecular kinks (i.e., labile domains) within molecular structure. In the present approach, soft collagenous tissues are regarded as composite materials with a reinforcement phase (i.e., crimped collagen fibers) embedded in a soft isotropic

matrix [2]. Crimped collagen fibers own a non-linear mechanical behaviour due to their geometric arrangement as well as to molecular kinks (i.e., labile domains) within molecular structure.

Analytical and computational approaches are coupled in order to obtain the macroscale tissue response in function of both nanoscale mechanisms and microscale non-linearities and by following a structural multiscale approach [3]. Within a finite-strain formulation, parameters governing polyconvex anisotropic strain energies are set on the basis of computational models of curvilinear fiber-like structures and analytical entropic/energetic molecular descriptions.

Accordingly, by introducing \mathbf{F} as the deformation gradient and $\mathbf{C} = \mathbf{F}^t \mathbf{F}$ as the right Cauchy-Green deformation tensor, the second Piola-Kirchhoff stress \mathbf{S} is obtained through

$$\mathbf{S} = 2 \frac{\partial \Psi}{\partial \mathbf{C}}, \quad (1)$$

where $\Psi = \Psi(\mathbf{C})$ is the tissue free-energy, describing an anisotropic hyperelastic behavior and ensuring convergence properties of the numerical scheme by taking advantage of the notion of polyconvexity, [4]. Accordingly, it is chosen

$$\Psi = P(\mathbf{F}, \text{Adj}\mathbf{F}, \det\mathbf{F}), \quad (2)$$

where the function $\mathbb{R}^{19} \mapsto \mathbb{R}$, $(\tilde{X}, \tilde{Y}, \tilde{Z}) \mapsto P(\tilde{X}, \tilde{Y}, \tilde{Z})$ is convex for all points $\mathbf{X} \in \mathbb{R}^3$, [4]. The functional form for function P and the value of model parameters are chosen on the basis of the response of suitable Representative Unit Systems (RUSs) modeling the dominant mechanisms at a given length scale.

For soft biological tissues, the microscale response is determined by the behavior of crimped collagen fibers (being the μ -RUS) modeled through their non-linear tangent modulus E_F , and in turn depending from the nanoscale mechanics of collagen fibrils (representing the nanoscale n -RUS), described by the tangent modulus E_f . The latter is obtained from the evidence that fibrils are staggered arrays of collagen molecules (with non-linear entropic-energetic tangent modulus E_m) *in-series* connected by inter-molecular cross-links of density λ and stiffness k_c . Refer to Fig. 1 and [3] for further details.

III. RESULTS

Obtained results allow to analyze the link between histological evidences related to collagen-related diseases with mechanical pathological behaviors. For instance, by referring to a standard aortic inflation test, the macroscopic effects of a

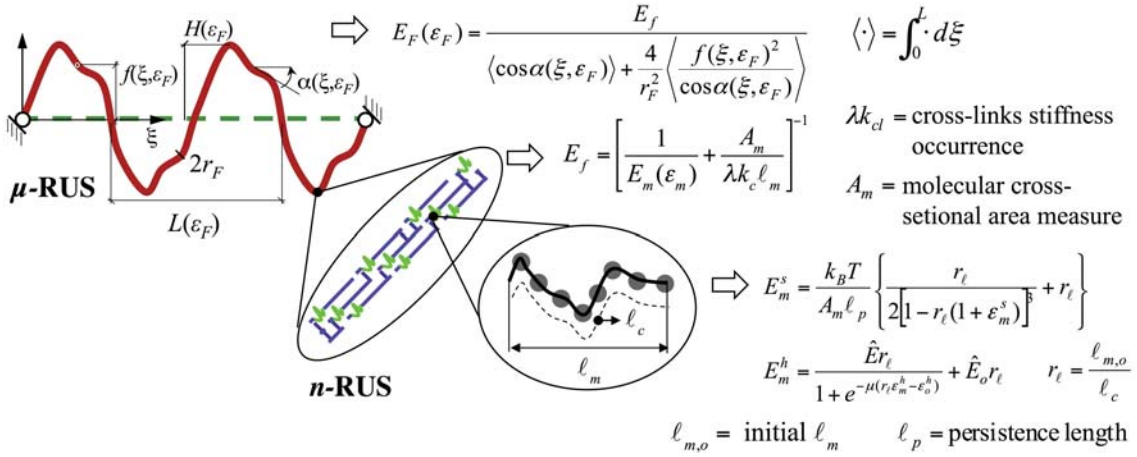


Fig. 1: Multiscale structural approach for biological tissues. Molecular parameters: ℓ_m = end-to-end extension, ℓ_c = contour length, ℓ_p = persistence length, \hat{E} , \hat{E}_o = upper and lower energetic tangent modulus, μ = uncoiling resistance, ε_o^h = uncoiling strain, A_m = cross-sectional area measure, k_B = Boltzmann constant, T = absolute temperature.

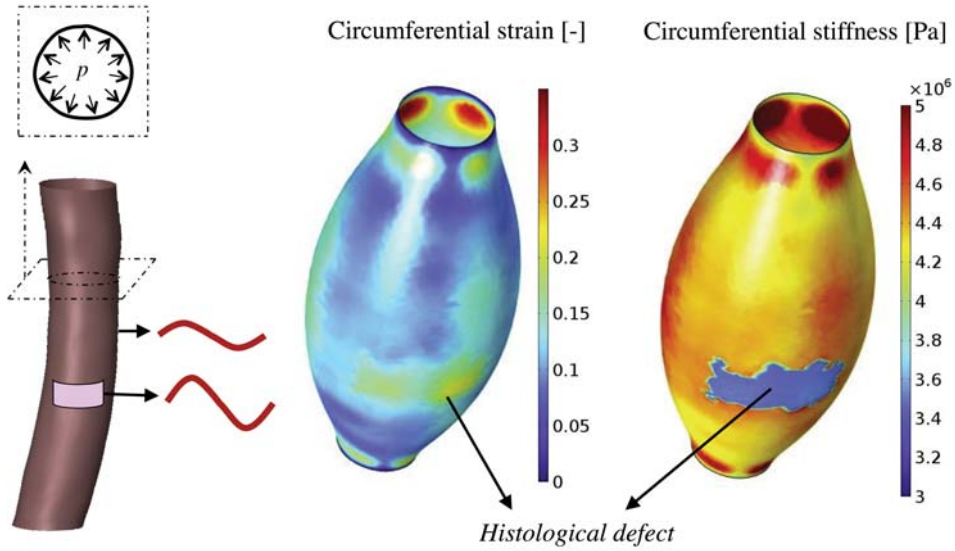


Fig. 2: Inflation test of an aortic segment characterized by a localized defect in fibers' crimp aspect. Geometry (left), circumferential strain [-] at $p = 180$ mmHg (middle) and circumferential stiffness [Pa] at $p = 180$ mmHg (right).

localized microscale defect in the aspect of fibers' crimp are investigated (see Fig. 2).

Moreover, the physiological or pathological tuning of tissue mechanics with collagen cross-linking enzymatic activity, collagen metabolism and histological arrangement of tissue constituents can be straightforwardly analyzed.

IV. CONCLUSIONS

By means of the present structural multiscale approach, nanoscale non-linearities represented by energetic-entropic effects are coupled with microscale ones associated with collagen fiber crimped configuration, leading to an effective analytical formulation.

Thanks to the structured organization of biological tissues, the proposed multiscale structural approach is effective and

accurate for different regular soft collagenous tissues (such as tendons, periodontal ligament and aortic media). Furthermore, the value of model parameters straight follows histo-chemical evidences opening to the analysis of the mechanics of diseased tissues or organs.

REFERENCES

- [1] G. Holzapfel, T. Gasser, and R. Ogden, "A new constitutive framework for arterial wall mechanics and a comparative study of material models". *J. Elast.*, 2000.
- [2] F. Maceri, M. Marino, and G. Vairo, "Age-dependent arterial mechanics via a multiscale elastic approach". *Int. J. Comput. Methods Eng. Sci. Mech.* 14, 2013, pp. 141–151.
- [3] M. Marino, G. Vairo, "Multiscale elastic models of collagen bio-structures: from cross-linked molecules to soft tissues". *Stud. Mechanobiol. Tissue Eng. Biomater.* 14, 2013, pp. 73–102.
- [4] J. Schröder, P. Neff, "Invariant formulation of hyperelastic transverse isotropy based on polyconvex free energy functions". *Int. J. Solids Struct.* 40, 2003, pp. 401–445.

Decoupling the roles of stiffness and hydroxyapatite signalling in the osteo-differentiation of stem cells

G. Mattei¹, C. Ferretti², M. Mattioli-Belmonte², A. Ahluwalia¹

¹ Research Centre "E. Piaggio", University of Pisa, Italy

² Department of Clinical and Molecular Sciences-Histology, Università Politecnica delle Marche, Ancona, Italy

Abstract—To decouple the contribution of mechanical cues from the effects owed to other HA signals in modulating periosteal progenitor cell (PDPC) osteogenic differentiation, a range of stiffness-matched HA/gelatin (HA/Gel) and gelatin based (Gel) materials were developed and characterised. This approach allowed us to independently investigate the role of stiffness and other HA-derived signals in directing stem cell fate. Our results show that both stiffness and HA contribute to directing PDPC osteogenic differentiation, with HA accelerating this differentiative process.

Keywords— stiffness, bone, periosteal stem cells, hydrogels, differentiation.

I. INTRODUCTION

BIOMATERIALS for engineering osteochondral tissues are typically composites made of an organic matrix such as collagen and an inorganic filler, often hydroxyapatite (HA), to mimic the composition of native bone. Several reports have shown that the bulk mechanical properties of composite materials increase with filler content, with subsequent implications on cell behaviour [1], [2]. However, the increase of HA, besides augmenting mechanical properties, also modifies the physicochemical cues provided by the material. As a consequence, decoupling the effects of different environmental signals on cell behaviour is difficult to achieve. To isolate the contribution of mechanical cues from other HA-derived signals in modulating progenitor cell differentiation towards the osteogenic phenotype, composite HA/gelatin hydrogel substrates with different amounts of inorganic phase and a set of HA-free gelatin substrates mimicking their stiffness were developed and characterised. The substrates were then seeded with human periosteal derived progenitor cells (PDPCs) and cultured over 7 days, analysing cell morphology and gene expression as function of mechanical and physicochemical cues. Our results show that both stiffness and HA contribute to directing PDPC fate towards an osteogenic phenotype, highlighting the role of stiffness in triggering the expression of osteogenic genes and of HA in accelerating the differentiative process. Given that tissue stiffness and mineral content in bone are frequently altered with ageing and/or disease, identifying their individual contributions in modulating progenitor cell differentiation towards the osteogenic phenotype has important implications for devising improved regenerative medicine strategies in the elderly.

II. MATERIALS AND METHODS

Hydroxyapatite/gelatin (HA/Gel) composites with different composition (i.e. HA/Gel = 0/100, 10/90, 25/75, 60/40, 70/30

w/w) were prepared by adding HA particles to a 5 % w/v gelatin solution. These weight ratios mimic those typical of osteochondral tissue, gradually ranging from cartilage (0/100) to subchondral bone (70/30) [1], [3]. HA/Gel substrates were crosslinked with 5mM GTA, while HA-free Gel were crosslinked using solutions with different concentrations of glutaraldehyde (i.e. 5, 10, 50, 100 mM) in order to find the mathematical relation between GTA concentration and substrate stiffness. Then, using the mathematical relationship between GTA concentration and Gel stiffness, appropriate crosslinking solutions were chosen and used to prepare Gel samples with stiffness matching those of HA/Gel. Samples were tested in unconfined uniaxial compression at a fixed strain rate of 0.01 s^{-1} . Compressive moduli were derived as the slope of the first linear portion of the stress-strain plot.

Periosteal tissue was obtained from 6 subjects. All patients provided their informed consent to participate in the study. Briefly, periosteal tissue was aseptically dissected, washed, cut into small pieces ($2\text{-}3 \times 2\text{-}3 \text{ mm}$) and placed in a 100 mm culture dish in Dulbecco's Modified Eagle Medium/Nutrient Mixture F-12 (DMEM/F-12) supplemented with 10 % Foetal Bovine Serum (FBS) and 1 % penicillin-streptomycin (100 U/mL) [4]. Before seeding, all the substrates (HA/Gel and Gel) were sterilized in 70 % v/v EtOH for 2 h, washed two times in PBS $1 \times$ for 30 min and placed under UV light for 30 min each side. Samples were observed with a Philips XL 20 SEM (FEI Italia SRL, Milan, Italy) equipped for X-ray microanalysis (EDS-PV 9800).

After 7 days of culture total RNA was isolated from PDPCs. Real-time (RT-qPCR) assays were performed using a Mastercycler Realplex2 thermocycler (Eppendorf GmbH, Germany). Each assay was performed as triplicate and reference gene's Cq values were used to normalise cellular mRNA data. The qPCR efficiency in all our experiments was more than 90 %. Experiments were all performed in triplicate. Data are reported as mean \pm standard deviation, unless otherwise noted. Data were analysed by one-way ANOVA, Student-Newman-Keuls's and Student's t-tests. Statistical significance was set at $p < 0.05$.

III. RESULTS AND DISCUSSION

HA/Gel stiffness increases with HA content, as expected (Fig. 1). The mechanical properties of HA-free gelatin (Gel) substrates were then characterised as a function of GTA. Having established a logarithmic relation between Gel stiffness and GTA concentration, different crosslinking solutions were used to obtain Gel hydrogels matching the

stiffness of HA/Gel samples. This approach allowed us to investigate the role of stiffness in modulating PDPC differentiation towards the osteogenic phenotype, independently of other HA-derived signals.

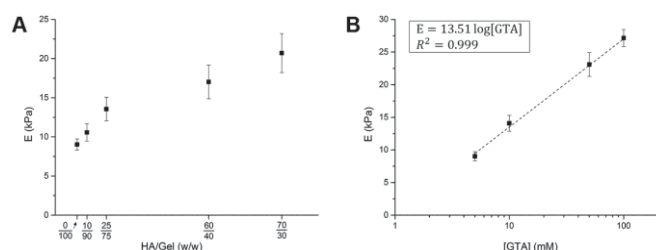


Figure 1: Compressive moduli obtained for (A) HA/Gel and (B) Gel substrates. Results are reported as a function of HA/Gel weight ratio and GTA concentration, respectively.

After 2 days PDPCs were able to adhere on all the substrates, independent of their composition, with minimal differences in cell morphology. At day 7 a good substrate colonisation was observed with changes in cell morphology related to the presence of HA. In particular, on HA/Gel substrates the increase in HA content from 25/75 to 70/30 affected cell spreading, with cells exhibiting a more elongated shape. On the contrary, cells adopted a star-shaped morphology on all Gel substrates, with no significant differences related to stiffness variations. Thus, PDPCs cultured on the different substrates differ in cell behaviour and this difference is mainly related to the change of stiffness, confirming their role as mechano-sensing cells.

RT-qPCR data are reported in Fig. 2 as fold-regulation over PDPCs seeded on 0/100 HA/Gel structures. In cells cultured on HA/Gel and Gel substrates we observed an almost comparable sequence of gene activation, confirming the hypothesis that extracellular matrix stiffness provides instructive signals dictating cell behaviour. Comparing the gene expression data of PDPCs after 7 days of culture on HA/Gel and Gel substrates, we observed that the presence of HA promotes an acceleration in cell differentiation. The expression of all genes involved in osteogenesis was up-regulated on HA/Gel substrates, with significant changes starting from the 25/75 HA/Gel substrate. Remarkably, only in PDPCs seeded on 70/30 HA/Gel substrates was the increase in bglap expression associated with a decrease in bmp2 mRNA transcription. This feature was not evident in cells seeded on Gel substrates, in which an increase in bglap expression is promoted. The concomitant interchange of bmp2 and bglap in PDPCs seeded on 70/30 HA/Gel substrates suggested that these cells were at a further stage of differentiation than on all the other substrates. Finally, even though bmp2 and runx2 have been shown to cooperatively interact to stimulate osteoblast gene expression, in our cells bmp2 overexpression is not always associated with an increase of runx2 mRNA levels. This observation strengthens the hypothesis that bmp2 signalling for osteoblast differentiation can also function independently of runx2.

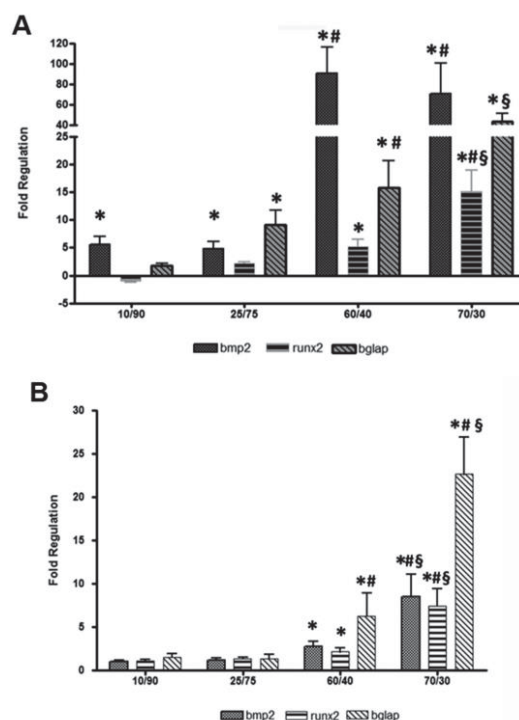


Figure 2: Changes in bmp2, runx2 and osteocalcin (bglap) mRNA expression in PDPCs seeded on (A) Gel and (B) HA/Gel substrates. Data are expressed as Fold-regulation which represents fold-change results in a biologically expressive manner. Fold-regulation is equal to the fold-change ($2^{-\Delta\Delta C_t}$) for fold-change values greater than one, which indicate an up-regulation. Fold-change values less than one indicate a down-regulation: in this case the fold-regulation is the negative inverse of the fold-change ($-1/2^{-\Delta\Delta C_t}$). a = $p < 0.05$ vs CTRL; b = $p < 0.05$ vs 25/75 substrates; c = $p < 0.05$ vs 60/40 substrates.

IV. CONCLUSIONS

In this work scaffolds with different HA content and their HA-free mechanical equivalents were investigated to isolate the contribution of stiffness from other HA-derived signals in PDPCs osteogenic differentiation. Our results show that both stiffness and HA contribute to directing PDPC osteogenic differentiation, highlighting the role of stiffness in triggering the expression of osteogenic genes and of HA in accelerating the process, particularly at high concentrations.

ACKNOWLEDGEMENT

The study was co-funded by the Italian Ministry of Education, University & Research (MIUR) (Project PRIN 2010, MIND, 2010J8RYS7) and an Italian FIRB Grant (project RBAP10MLK7).

REFERENCES

- [1] P. Gentile, M. Mattioli-Belmonte, V. Chiono, C. Ferretti, F. Baino, C. Tonda-Turo, et al., "Bioactive glass/polymer composite scaffolds mimicking bone tissue", *J. Biomed. Mater. Res. A*, vol. 100, pp. 2654-67, 2012.
- [2] C. Jelen, G. Mattei, F. Montemurro, C. De Maria, M. Mattioli-Belmonte, G. Vozzi, "Bone scaffolds with homogeneous and discrete gradient mechanical properties", *Mater Sci Eng C*, vol. 33, pp. 28-36, 2013.
- [3] A. Tampieri, M. Sandri, E. Landi, D. Pressato, S. Francioli, R. Quarto, et al., "Design of graded biomimetic osteochondral composite scaffolds", *Biomaterials*, vol. 29, pp. 3539-46, 2008.
- [4] R. Pal, M. Hanwate, M. Jan, S. Totey, "Phenotypic and functional comparison of optimum culture conditions for upscaling of bone marrow-derived mesenchymal stem cells", *J. Tissue Eng. Regen. Med.*, vol. 3, pp. 163-74, 2009.

Smart enzymatically stiffenable hydrogels for 3D in-vitro models of tissue ageing and fibrosis

G. Mattei¹, A. Tirella², M. La Marca¹, D. Giacomelli¹, N. Tirelli² and A. Ahluwalia¹

¹ Research Centre “E. Piaggio”, University of Pisa, Italy

² School of Materials, University of Manchester, United Kingdom

Abstract—This work presents the development and characterisation of enzyme-responsive hydrogels for engineering 3D in-vitro models of tissue ageing and fibrotic processes. Given the critical role of the biomechanical environment in regulating cell behaviour and directing the development of tissue fibrosis, hydrogels were designed to reproduce the stiffness of healthy tissue and to subsequently be stiffenable via enzymatic activity to recreate aged or fibrotic environments, in an in-vivo like manner. Hydrogels design and characterisation are first described, then preliminary cell experiments are presented.

Keywords—hydrogels, 3D in-vitro models, liver, tissue fibrosis.

I. INTRODUCTION

DURING the last decade, there has been a decisive shift from 2D cell monolayers grown on plastic to 3D cell cultures, implementing more relevant in-vitro models to predict the complex behaviour of biological systems [1]. The classical tissue engineering approach, based on the successful interaction between cell, scaffold and bioreactor, represents an attractive strategy to develop 3D in-vitro models [2]. The consensus is that an ideal scaffold should mimic most of the properties of the native extracellular matrix (ECM) to provide cells with an appropriate microenvironment promoting their growth, differentiation and function. Among the ECM cues, biomechanical properties play a critical role in regulating pathophysiological cell behaviour and directing the development of tissue fibrosis (which is generally associated with an enzyme-mediated ECM stiffening) [3]. With the hypothesis that tissue stiffness increases as fibrosis progresses and aiming at replicating the time-dependency of fibrotic processes, dynamic scaffolds that mimic the elasticity of healthy and diseased tissue ECM in-vitro need to be redesigned to temporally manipulate their mechanical properties on demand [4]. In the context of 3D in-vitro organ models, this work is focused on the liver, by way of its central role in both endogenous and exogenous metabolism [5]. Aiming at developing pathophysiological 3D in-vitro liver models, we present a library of synthetic hydrogels for hepatic cell encapsulation. Given the importance of the biomechanical environment, the main hydrogel design requirement is to mimic the stiffness of healthy liver ECM and to be subsequently stiffenable at a user defined time for reproducing fibrotic-like environments on demand. Hydrogels were designed in view of using lysyl oxidase (LOx) enzymatic crosslinking to be dynamically stiffened towards aged or fibrotic environments at a user-defined time, in an in-vivo like manner. Hydrogels were characterised in their mechano-structural properties, then preliminary cell experiments with hepatocytes were performed to assess the suitability of

developed materials for encapsulating hepatic cells to engineer 3D in-vitro liver models.

II. MATERIALS AND METHODS

Hydrogels with tunable elastic moduli were obtained via a 1st step photo-crosslinking of mixtures of mono- and diacrylate poly(ethylene glycol) derivatives, tethered with different amounts of primary amines (NH₂). Three different hydrogel families in terms of acrylate/diacrylate molar ratio (A/DA) were investigated keeping the total PEG content constant to 5 % w/v. Each A/DA family was functionalized with three different quantities of amino groups (NH₂/A=0.00, 0.05, 0.10) generating a library of hydrogels where the densities of cross-links (hence the resultant mechano-structural properties) could be varied independently of the amount of tethered amines. Afterwards, “healthy” hydrogels stiffness was enhanced to “fibrotic” values, by administering a LOx-containing solution as 2nd step crosslinking reaction. Glyoxal (GO), a low molecular weight amine cross-linker, was used as a positive control for LOx. Amine crosslinking reactions were optimised using soluble models prior to their application to hydrogels.

Hydrogel mechanical properties were characterized in shear using a Gemini Advanced Rheometer (Bohlin Instruments, UK) and in unconfined compression using a Zwick/Roell ProLine Z005 uniaxial testing device (Zwick/Roell, Ulm, Germany) equipped with a 10 N load cell. Then, 2D and 3D hepatic healthy models were obtained seeding HepG2 on hydrogels surface (2D model, 50·10³ cell/cm²) or encapsulating hepatocytes within the gels (3D model, 1 mm thickness, 5·10⁶ cell/mL). Amino containing hydrogels with A/DA=0.50 and NH₂/A=0.10 were chosen for preliminary cell experiments with HepG2 cells. The latter were also cultured onto collagen gels and used as 2D control. The 2D and 3D constructs were cultured in a bioreactor under dynamic conditions for 7 days, assessing hepatic functions (urea and albumin production), cell viability (Live/Dead assay) and morphology (DAPI/phalloidin).

III. RESULTS AND DISCUSSION

Rheological (G'), compressive (E) and swelling (Q) properties of healthy hydrogels were found to be decoupled from their amino content and dictated only by different A/DA ratios (Table 1).

TABLE I
HYDROGELS MECHANO-STRUCTURAL PROPERTIES

A/DA	$G' (kPa)$	$E (kPa)$	Q
0.25	1.22 ± 0.04	3.81 ± 0.12	20.0 ± 0.03
0.50	0.59 ± 0.06	1.81 ± 0.08	25.4 ± 1.1
0.75	0.28 ± 0.03	0.81 ± 0.05	31.0 ± 1.0

GO and LOx amino cross-linking reactions exhibited similar kinetic and conversion (about 40% of initial free NH_2 in the gel reacted in 48 h), resulting in an averaged compressive stiffening of 126 ± 13 Pa per mmol of reacted amine. Hydrogel stiffness match that of healthy and (after LOx reaction) fibrotic liver tissue [6], [7]. Metabolite production, expressed as quantity produced per cell per day, was found to be similar between 2D and 3D models and 2D controls, in agreement with [8], [9]. In particular, average albumin and urea production rate were found to be equal to 2.01 ± 0.11 and 596 ± 41 pg/cell/day, respectively. Confocal acquisitions revealed that cells in 2D models possess high viability ($> 95\%$) and reorganize into clusters (Fig. 1), while in 3D constructs cells are vital ($> 60\%$) and homogeneously distributed throughout the hydrogel volume (Fig. 2). No differences in cell morphology were observed between 2D and 3D models.

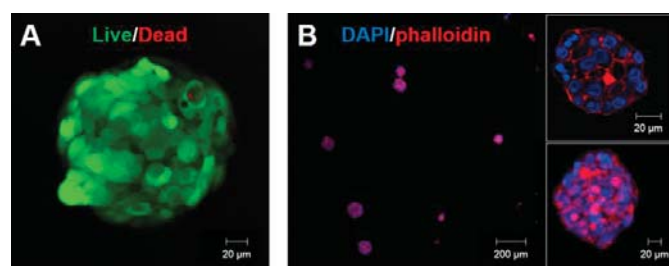


Figure 1: Confocal acquisitions of HepG2 cells seeded onto hydrogels (2D models) at day 7. A) Live/Dead assay showing a cluster of live (green) and dead (red) cells. B) DAPI/phalloidin staining showing cell nuclei (blue) and F-actin (red). Image inserts show details of HepG2 cells reorganized into spheroids.

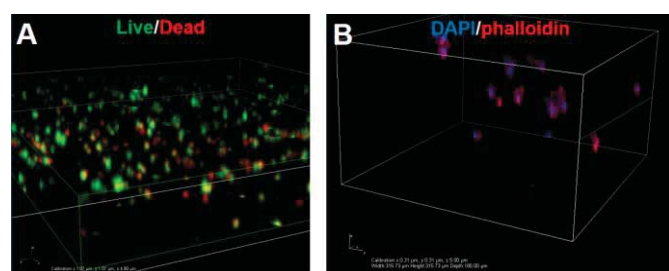


Figure 2: Volume rendered confocal acquisitions of HepG2 cells photo-encapsulated within hydrogels (3D models) at day 7. A) Live/dead assay showing live (green) and dead (red) cells. Volume size: $1093 \times 1093 \times 110 \mu m$. B) DAPI/phalloidin staining showing cell nuclei (blue) and F-actin (red). Volume size: $315 \times 315 \times 180 \mu m$.

IV. CONCLUSIONS

A library of hydrogels with tunable mechanical properties was developed. These gels can be stiffened towards fibrotic models on demand, by using an enzyme typically involved in ECM crosslinking (i.e. LOx), mimicking the

pathophysiological fibrotic process. Encapsulated cells were found to be vital and preserve their function, suggesting that developed gels can be attractive platforms for 3D in-vitro liver models to study the effect of fibrotic-like environmental stiffening on cell response.

ACKNOWLEDGEMENT

The work leading to these results has received partial funding from the European Union Seventh Framework Programme (FP7/2007-2013) under grant agreement n° 304961 (ReLiver).

REFERENCES

- [1] H. Geckil, F. Xu, X. Zhang, S. Moon, and U. Demirci, "Engineering hydrogels as extracellular matrix mimics", *Nanomedicine*, vol. 5, pp. 469–84, 2010.
- [2] R. Pörtner, C. Giese, "An Overview on Bioreactor Design, Prototyping and Process Control for Reproducible Three-Dimensional Tissue Culture", in *Drug Testing in vitro*, M. Uwe, V. Sanding, Ed. Wiley-VCH Verlag GmbH & Co. KGaA, 2006, pp. 53–78.
- [3] C. Frantz, K. M. Stewart, and V. M. Weaver, "The extracellular matrix at a glance", *J. Cell Sci.*, vol. 123, no. 24, pp. 4195–200, 2010.
- [4] M. Guvendiren, J. A. Burdick, "Stiffening hydrogels to probe short- and long-term cellular responses to dynamic mechanics.", *Nat. Commun.*, vol. 3, p. 792, 2012.
- [5] I. M. Arias, H. J. Alter, J. L. Boyer, D. E. Cohen, N. Fausto, D. A. Shafritz, and A. W. Wolkoff, *The Liver*. Chichester, UK: John Wiley & Sons, Ltd, 2009.
- [6] G. Mattei, V. Di Patria, A. Tirella, A. Alaimo, G. Elia, A. Corti, A. Paolicchi, and A. Ahluwalia, "Mechanostructure and composition of highly reproducible decellularized liver matrices", *Acta Biomater.*, vol. 10, pp. 875–82, 2014.
- [7] W. C. Yeh, P. C. Li, Y. M. Jeng, H. C. Hsu, P. L. Kuo, M. L. Li, P. M. Yang, and P. H. Lee, "Elastic modulus measurements of human liver and correlation with pathology", *Ultrasound Med. Biol.*, vol. 28, pp. 467–474, 2002.
- [8] B. Vinci, D. Cavallone, G. Vozzi, D. Mazzei, C. Domenici, M. Brunetto, et al., "In vitro liver model using microfabricated scaffolds in a modular bioreactor", *Biotechnol J*, vol. 5, pp. 232–41, 2010.
- [9] S. F. Lan, B. Safiejko-Mroccka, B. Starly, "Long-term cultivation of HepG2 liver cells encapsulated in alginate hydrogels: a study of cell viability, morphology and drug metabolism", *Toxicol In Vitro*, vol. 24, pp. 1314–23, 2010.

Patient-specific multi-scale modelling of cardiac biomechanics in single ventricle circulation

A. Meoli¹, E. Cutri¹, G. Dubini¹, F. Migliavacca¹ and G. Pennati¹

¹Politecnico di Milano, Milan, Italy

Abstract—Patient-specific models of single ventricle circulation represent a powerful tool to investigate ventricular functionality. In this study, we adopt a multi-scale approach that couples 0D circulatory model of the patient to 3D structural model of the single ventricle. To investigate this particular condition two patients affect by hypoplastic heart syndrome have been considered.

Keywords—Single ventricle heart, multi-scale patient-specific model, lumped parameter network, 3D cardiac mechanics.

I. INTRODUCTION

SINGLE ventricle (SV) defect is a complex congenital heart disease (CHD) characterized by the underdevelopment of one ventricular chamber, which is invariably fatal during the first weeks of life without intervention [1]. Normally, SV patients are treated following the Fontan procedure: a three-stage surgical repair with the goal of obtaining separated pulmonary and systemic circulations [2]. The technique involves changes in the circulatory layout, with the SV providing systemic blood flow and venous return flowing passively into the lungs. Hence, the SV heart in addition to an unusual high work is subjected to abrupt changes in the working conditions after each surgical stage.

Nowadays, thanks to the improvements in the imaging techniques it is easier to build patient-specific models of cardiovascular hemodynamics (e.g. for the treatment of CHD). In this regard, 3D finite element models have proved to be a valid tool to assess regional information (e.g. stress and strain) in the normal and abnormal heart, thus evaluating changes in the ventricular functionality that cannot be directly measured in the patient [3,4].

The aim of this study is the assessment of SV functionality across the stage 1 surgery by means of patient-specific multi-scale 3D-0D models. The approach consists in coupling a patient-specific lumped-parameter network (LPN) of the entire circulatory system with a 3D structural model of the SV. The multi-scale model allows the prediction of local information about ventricular function (i.e. stress and wall kinematics), as well as global parameters such as pressure-volume loops and cardiac performance (i.e. cardiac output and ejection fraction). Two patients from different pathologies (right or left SV hearts) have been considered.

II. MATERIALS AND METHODS

A multi-scale 3D-0D patient-specific model of SV heart is composed of four main components (Fig. 1): i) a closed-loop circulatory model; ii) an anatomical model of the SV; iii) a passive constitutive law; iv) an active dynamic model.

A. Closed loop LPN model

Patient-specific closed-loop 0D models of the circulatory network were developed to apply proper hemodynamics boundary conditions to the 3D model. The basic LPN layout is comprised of four RLCRCR blocks to account for upper body, lower body, right and left pulmonary branches. The proper connection of the four blocks allows the description of SV circulations for different stages.

To estimate the LPN parameters, the loop is closed with two time-varying elastances, representing the single atrium and the SV, as well as atrio-ventricular (AV) and aortic valves, described by non-linear diodes [5]. Patient right and left pulmonary vascular resistances (RPVR LPVR) and upper and lower body systemic vascular resistances (UBSVR LBSVR) were calculated on the basis of mean values of pressures and flows [6], while the other circulatory parameters are obtained by means of an optimization process described elsewhere [7].

B. Anatomical model

Hexahedral cubic-Hermite finite element mesh of the ventricular geometry is constructed based on the clinical image data. Endocardial and epicardial contours of the SV patient heart at end-diastole were manually segmented from cardiac magnetic resonance images. Then an initial template of a SV heart was fitted to the reconstructed geometry in order to match the patient anatomy. Fibre architecture is assumed as in physiological ventricles since information for SV hearts are lacking.

C. Passive model and unloaded geometry

The resting material properties of the myocardium were described using the transversely-isotropic form of the constitutive model proposed by Holzapfel and Ogden [8]. The myocardial passive material parameters were estimated together with the identification of the unloaded geometry. To this aim, an iterative method previously developed was adopted [4]. This unloading algorithm was able to estimate the unloaded geometry on the basis of the ED ventricular model, if the ED pressure (measured) and the unloaded volume (assumed) were known, whereas the passive material parameters were iteratively tuned.

D. Active model

After SV unloaded geometry and passive material parameters were obtained, the contractile parameters were determined to match the measured peak SV pressures and end-systolic volumes. To adjust the parameters of the Lumens et al. [9] active contraction model the 3D model was contracted isovolumically at different level of volumes tuning the active parameters.

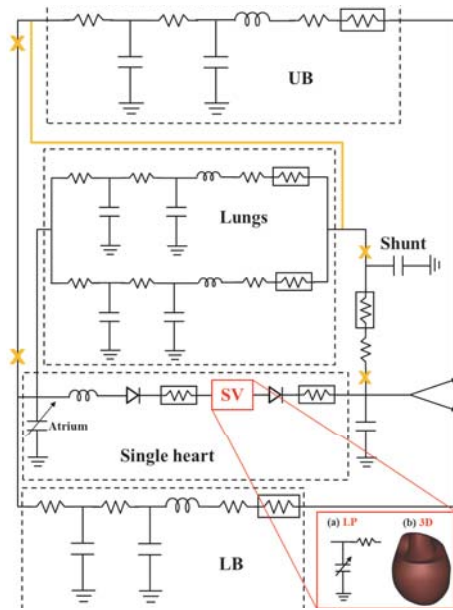


Figure 1 - Patient-specific biomechanical model for stage 1 and stage 2. The circulatory layout of stage 1 is showed in continuous black lines. After the stage 2 surgery, the shunt was removed and the UB circulation connected in series to the pulmonary circulation (changes are shown in orange). The SV was modelled as a time-varying elastance (red box (a)) to perform parameters identification. In the multiscale models of stage 1 and stage 2 conditions the LP model of the SV was replaced by the 3D (red box (b)).

III. RESULTS AND DISCUSSION

The 3D-0D results of the stage 1 condition of the patients are summarized in Table 1. Results were reported against the pre-operative clinical data. An overall good agreement was obtained for both patients in replicating the main clinical quantities (error lower than 5%). A proper CO indicates a satisfactory description of ventricular-arterial and venous-atrial couplings. Moreover, the correct repartition of flows to the systemic (Q_{UB} and Q_{LB}) and pulmonary circulations (Q_P) ensures good modelling of the systemic-to-pulmonary shunt.

Table 1 - Comparison between clinical data and results of the 3D-0D models for both stage 1 and stage 2. CO, cardiac output; EDV, end-diastolic volume; mP_{ao} , mean aortic pressure; $maxP_{ao}$, maximum aortic pressure; $minP_{ao}$, minimum aortic pressure; mP_{SA} , mean atrial pressure; mP_{PA} , mean pulmonary pressure; $maxP_{SV}$, maximum single ventricle pressure; mQ_P , mean pulmonary flow; mQ_{UB} , mean upper body flow; mQ_{LB} , mean lower body flow. CO and flows in ml/s, EDV in ml and pressures in mmHg.

	MUSC7			UM5		
	CLIN	S1	S2	CLIN	S1	S2
CO	27.1	26.7	20.3	27.0	27.4	19.0
EDV	28.0	28.7	26.3	29.6	29.2	24.1
mP_{ao}	53.0	53.9	74.0	53.0	53.2	69.1
$maxP_{ao}$	80.0	81.5	95.8	87.0	82.8	90.4
$minP_{ao}$	30.0	31.7	55.5	30.0	29.1	50.6
mP_{SA}	7.0	7.8	4.6	5.0	4.8	1.7
mP_{PA}	17.0	16.9	14.4	13.3	12.9	10.6
$maxP_{SV}$	82.0	83.3	96.7	90.0	85.2	91.3
mQ_P	12.0	12.1	12.9	12.0	12.2	10.0
mQ_{UB}	10.0	10.2	12.8	11.0	11.1	13.4
mQ_{LB}	5.1	5.2	7.5	4.0	4.1	5.6

The changes in the circulatory layout associated with the surgery, led to an increase in the afterload and to a decrease of the preload of the SV. Results are reported in Table 1. Comparing stage 1 and stage 2 simulations: i) stroke volume (i.e. the CO, assuming no change in the frequency)

significantly decreases (about 20-40% depending on the considered patient; ii) the EDV decreases confirming the beneficial effect of the surgery; iii) aortic pressure increases in the mean value. It is worth noting that the predicted changes in flows and pressures are in agreement with a previous work on SV circulation [10], thus increasing the confidence in the multiscale models.

Concerning fibre stress in the preoperative state, at the systolic peak UM5 presented the higher value (46 kPa) while at end diastole MUSC7 showed the higher value (5 kPa). In other works, similar values and patterns of stress in the fibre direction are reported, thus suggesting reliability of the obtained results. Regarding the fibre strain, MUSC7 showed the higher values of strain reaching 25%. It is worth noting that both patients showed significant portions of the myocardial wall with fibre strains ranging from 20% to 25%. These values are known to be rather critical because they are very close to sarcomere decompensation. Postoperatively, stresses at the systolic peak remain similar due to the increase in the SV peak pressure, while at end diastole significantly decreases confirming the beneficial effect of the surgery.

IV. CONCLUSION

In this work, we adopt a patient-specific multi-scale approach to study the cardiac biomechanics in two patients affected by SV malformations. The models showed good capability in reproducing hemodynamics of different patients affected by SV defects for stage 1 and stage 2 states.

ACKNOWLEDGEMENT

This study was supported by a grant from the Fondation Leducq, Paris, France.

REFERENCES

- [1] D.M. Bardo, D.G. Frankel, K.E. Applegate, D.J. Murphy and R.P. Saneto, "Hypoplastic left heart syndrome", *Radiographics*, vol. 21, pp 705-717, 2001.
- [2] M.R. de Leval and J.E. Deanfield, "Four decades of Fontan palliation", *Nat Rev Cardiol*, vol. 7, pp 520-527, 2010.
- [3] A. Aguado-Sierra, A. Krishnamurthy, C.T. Villongco, J. Chuang, E. Howard, et al., "Patient-specific modeling of dyssynchronous heart failure: A case study", *Prog Biophys Mol Bio*, vol. 107, pp 147-155, 2011.
- [4] A. Krishnamurthy, C.T. Villongco, J. Chuang, L.R. Frank, V. Nigam, et al., "Patient-specific models of cardiac biomechanics", *J Comput Phys*, vol. 244, pp 4-21, 2013.
- [5] F. Migliavacca, G. Pennati, G. Dubini, R. Fumero, R. Pietrabissa, et al., "Modeling of the Norwood circulation: effects of shunt size, vascular resistances, and heart rate", *Am. J. Physiol. Heart Circ. Physiol.*, vol. 280, pp 2076-2086, 2001.
- [6] A. Baretta, C. Corsini, W. Yang, I.E. Vignon-Clementel, A.L. Marsden, et al., "Virtual surgeries in patients with congenital heart disease: a multi-scale modelling test case", *Philos T R Soc A.*, vol. 369, pp 4316-4330, 2011.
- [7] A. Baretta, "Patient-specific modeling of the cardiovascular system for surgical planning of single-ventricle defects", *PhD thesis*, School of Bioengineering, Politecnico di Milano, 2014.
- [8] G. Holzapfel and R. Ogden, "Constitutive modelling of passive myocardium: a structurally based framework for material characterization", *Philos T R Soc A.*, vol. 367, pp 3445-3475, 2009.
- [9] J. Lumens, T. Delhaas, B. Kirn and T. Arts "Three-wall segment (TriSeg) model describing mechanics and hemodynamics of ventricular interaction", *Ann Biomed Eng.*, vol. 37(11), pp 2234-2255, 2009.
- [10] C. Corsini, C. Baker, E. Kung, S. Schievano, G. Arbia, et al., "An integrated ap- proach to patient-specific predictive modeling for single ventricle heart palliation", *Computer Methods in Biomechanics and Biomedical Engineering*, vol. 367, pp 3445-3475, 2014.

A Finite Element Study of the Pedicle Subtraction Osteotomy (PSO)

C. Ottardi¹, M. Sasso¹, L. Prosdocimo¹, A. Luca², F. Galbusera², T. Villa^{1,2}

¹ L, Department of Chemistry, Materials and Chemical Engineering "G. Natta", Politecnico di Milano

² IRCCS Istituto Ortopedico Galeazzi, Milano

Abstract — Pedicle Subtraction Osteotomy is a complex surgical technique, trying to restore a physiological lumbar lordosis. However, serious complications and instrumentation failure are often reported. This work was aimed at the numerical evaluation of different osteotomies and their possible treatments, to understand the failure mechanism and assist the decision making process of the clinician.

Keywords—PSO, lumbar instability, finite element.

I. INTRODUCTION

Pedicle Subtraction Osteotomy (PSO) is a surgical technique that can be used when there is a severe sagittal imbalance and all the conservative treatments fail. The surgical procedure is aimed at increasing the lumbar lordosis, cutting a wedge of the vertebral body, the posterior elements and the ligaments [1,2]. Several complications are reported in literature [2,3] and often when a consolidation of the bone in the anterior part of the column is not achieved, a failure of the instrumentation is reported [2,3].

The goal of this study was to investigate the instability induced on the lumbar spine after a Pedicle Subtraction Osteotomy. Moreover, with a numerical comparative analysis different treatments were analysed.

II. MATERIAL AND METHODS

The computational analysis were performed starting from a validated finite element model (FEM) of the intact human lumbar spine (L1-S1) complete of vertebrae, discs and ligaments. The lumbar lordosis of 35° between L1-S1, is low and compatible with a surgical treatment of PSO.

In particular, this surgical technique was simulated on two different levels of the spine, L3 and L4 (models OL3 and OL4 respectively) resecting the vertebral body with a wedge shape and causing a 30° increase of the lumbar lordosis, as shown in Figure 1. A contact with friction was defined between the fractured surfaces. All the models were loaded with pure moments of 7.5 Nm in all the motion directions (flexion-extension, lateral bending and axial rotation), with a follower load of 500 N. After that, the destabilized models were treated with spinal fixators two levels above and below the osteotomy and simulations were run with the same loading conditions. For each osteotomy model, different devices were used for the fixation (models OL3-fixed and OL4-fixed shown in Figure 2), in particular rod with 5 and 6 mm to investigate the role of the diameter and TiAl4V and Cr-Co devices to study the effect of the material.

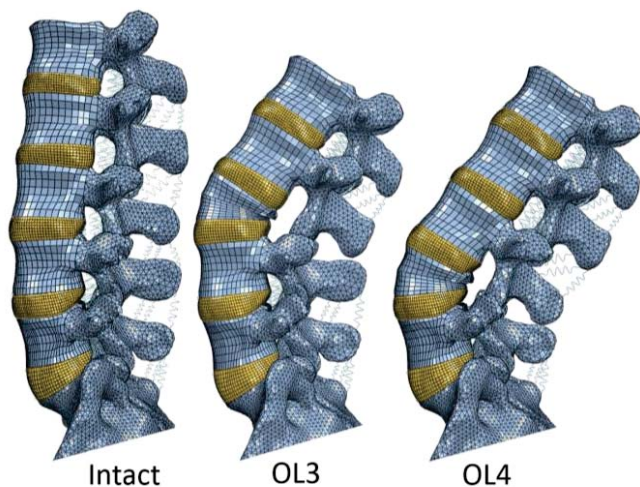


Figure 1: Intact model, osteotomy in L3 (OL3 model) and osteotomy in L4 (OL4 model)

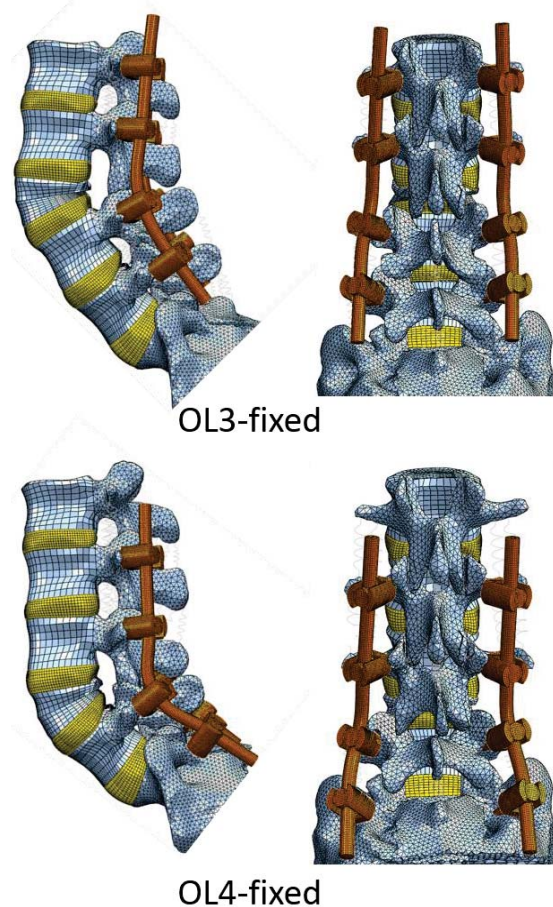


Figure 2: instrumented models corresponding to the osteotomy in L3 (OL3-fixed) and in L4 (OL4-fixed)

III. RESULTS

The Range of Motion of each model, the von Mises stresses at the osteotomy level and the internal loads in the rods were calculated. In Table I the ROM of the intact and destabilized models are shown. As expected, both destabilizations cause an increase of the ROM for all the movement. The ROM and the stresses obtained using a 5 mm rod are slightly bigger than using a 6 mm one. While using Cr-Co rods, the ROM of the models decreases up to 10%. The stresses at the osteotomy level increases and also the axial force along the rod, because of the lower stiffness of the titanium devices.

TABLE I: ROM of the intact and destabilized models (°)

<i>Model</i>	<i>Flex-Ext</i>	<i>Lat. Bend</i>	<i>Ax. Rot</i>
<i>Intact</i>	22.9	14.6	13.0
<i>OL3</i>	27.4	20.2	19.1
<i>OL4</i>	28.8	28.9	16.6

IV. DISCUSSION

The PSO is an effective surgical technique, for the treatment of rigid spine with sagittal imbalance. Two spinal osteotomy, performed on different levels were studied. In all the cases, the part of the spinal fixators subjected to the higher loads was the rod, in correspondence with the vertebral resection. The axial force measured in the rod of the instrumented models (OL3-fixed and OL4-fixed) was about 20% of the follower load imposed at the beginning of the analysis. Changing the material and using Cr-Co alloys, lead to a 5% increase of the axial force and a 30-40% of the stresses, due to the higher stiffness. A similar trend is noticed varying the diameter of the rod: using a bigger rod (6 mm instead of 5) change the load path, increasing the axial force on the construct but in this case, due to the increased section of the rod, decreasing the von Mises stresses at the osteotomy level. Other configurations will be further studied such as a bilateral double rod and the effect of an anterior support, with the aim of find new strategies to prevent rod breakage and support the bone healing.

REFERENCES

- [1] P.F. Bergin, J.R. O'Brien, L.E. Matteini, W.D. Yu, K.M. Kebaish (2010), "The Use of Spinal Osteotomy in the Treatment of Spinal Deformity", *Ortopedics*, 33-8:586-594
- [2] A.Luca, A. Lovi, F. Galbusera, M. Brayda-Bruno (2014), "Revision surgery after PSO failure with rod breakage: a comparison of different techniques"
- [3] Y. Wang, O. Boachie-Adjei, L. Lenke (2015), "Spinal osteotomy", Springer, Ch.1 and 8

Evaluation of the accuracy and precision of a local DVC approach applied to natural and augmented vertebrae

Palanca M.¹, Tozzi G.², Danesi V.¹, Dall'Ara E.³, Viceconti M.³, Cristofolini L.¹

¹ School of Engineering and Architecture, University of Bologna, Bologna, Italy

² School of Engineering, University of Portsmouth, Portsmouth, UK

³ Insigneo, Institute for in Silico Medicine, University of Sheffield, UK

Abstract—The Digital Volume Correlation (DVC) approach allows investigating the internal displacement and strain in biological structures, including vertebrae. The reliability of the output cannot be taken for granted, so an optimization is strongly required. Six vertebra specimens (natural and augmented) were scanned with a micro-CT in a zero-strain condition. A local DVC approach was used to compute the displacement and strain. Accuracy and precision errors were evaluated for 5 volumes of interest (VOI) and for different microstructures. The results, of the preliminary test on a single vertebra, showed that the VOI with the lowest errors was the bone-cement fully augmented; the worst was the VOI containing the trabecular/cortical interface. Future work includes, rigid registration, masking of the background and the use of a global DVC approach in order to investigate possible improvements of accuracy and precision.

Keywords—Digital Volume Correlation, vertebra, accuracy, precision.

I. INTRODUCTION

Digital Volume Correlation (DVC) is a toolkit that combine high-resolution imaging and an algorithm to elaborate internal displacements and strains [1, 2]. Measuring the accuracy and precision of DVC-computed displacements and strains is a complex, but mandatory task. An intrinsic difficulty in validating DVC is that no other experimental technique allows measuring displacements and strain inside the specimen [3]. The aim of this work is to evaluate the accuracy and precision of a DVC approach on natural and augmented vertebrae.

II. MATERIALS AND METHODS

Six thoracic vertebra specimens (three natural and three prophylactically augmented) were scanned twice, in a zero-strain condition, with a micro-CT (resolution: 33-39 micrometers). Five different volume of interest (VOI) were determined for each vertebra (Table 1). The displacements and strains were computed, with a commercial DVC software (DaVis, LaVision, Goettinger, Germany), based on a local correlation approach.

Table 1: Summary of the different volumes of interest investigated and their relative dimensions.

VOI	Region	Dimension (voxels)
VOI-1	Entire vertebra	887x639x481
VOI-2*	Bone-cement fully augmented	150x150x310
VOI-3*	Bone-cement partially augmented	150x150x310
VOI-4	Trabecular bone	150x150x310
VOI-5	Trabecular/cortical bone interface	150x150x310

*VOI available only in the augmented vertebrae.

DVC computation achieved a final sub-volume size of 32x32x32 with an overlap of 75% using a multi-pass scheme; as in the work [4]

Accuracy and precision were evaluated as average (accuracy) and standard deviation (precision) of the average of the six components of the strain in each sub-region of the considered VOI [5].

III. RESULTS

The preliminary accuracy and precision errors calculated for the selected volumes of interest with the commercial software DaVis on a single vertebra are reported in Fig. 1. For the preliminary test, the errors were evaluated in absence of rigid registration before the DVC algorithm was applied.

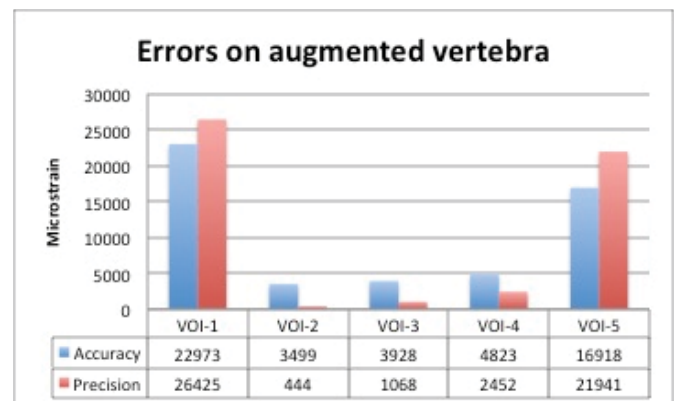


Fig. 1: Accuracy and precision errors in the different volumes of interest in augmented vertebra.

IV. DISCUSSION

Most of the uncertainties were localised in the trabecular/cortical interface. Conversely, the fully augmented VOI exhibited the best accuracy and precision. The current results suggest how, in absence of rigid registration and background masking, the strain error is unacceptable for many biomechanical applications. In order to improve the accuracy and precision of the DVC approach, the next step of this work will include a rigid body correction (to overcome the micromovements of the machine) and a masking background (to evaluate the effect of the gradient in between the different microstructures). Moreover, we will add a comparison with a global DVC approach [2] and extend the analysis of accuracy and precision errors to each strain component [4]

ACKNOWLEDGEMENT

The authors would like to thank the European Society of Biomechanics (ESB mobility award 2014) and the Royal Society (RG130831).

REFERENCES

- [1] [1] Roberts, B. C., Perilli, E., and Reynolds, K. J., 2014, "Application of the digital volume correlation technique for the measurement of displacement and strain fields in bone: A literature review," *Journal of biomechanics*, 47(5), pp. 923-934.
- [2] [2] Dall'Ara, E., Barber, D., and Viceconti, M., 2014, "About the inevitable compromise between spatial resolution and accuracy of strain measurement for bone tissue: A 3D zero-strain study," *Journal of biomechanics*, 47(12), pp. 2956 - 2963.
- [3] [3] Freddi, A., Olmi, G., and Cristofolini, L., 2015, *Experimental Stress Analysis for Materials and Structures: Stress Analysis Models for Developing Design Methodologies*.
- [4] [4] Palanca, M., Tozzi, G., Cristofolini, L., Viceconti, M., and Dall'Ara, E., accepted (doi:10.1115/1.4030174), "3D Local Measurements of Bone Strain and Displacement: Comparison of Three Digital Volume Correlation Approaches," *J. Biomech Eng. (ASME)*.
- [5] [5] Liu, L., and Morgan, E. F., 2007, "Accuracy and precision of digital volume correlation in quantifying displacements and strains in trabecular bone," *Journal of biomechanics*, 40(15), pp. 3516-3520.

The role of aortic shape and valve phenotype in the bicuspid aortopathy

S. Pasta¹, A. Rinaudo², G. Gentile³, G.M. Raffa³, A. Luca³, M. Pilato³ and C. Scardulla³

¹ *Fondazione RiMED, Palermo, Italia*

² *DICGIM, Università di Palermo, Palermo, Italia*

² *ISMETT (IRCCS) Palermo, Italia*

Abstract— Patients with bicuspid aortic valve (BAV) frequently develop ascending aortic dilatation, with different degree of pattern and aortic growth. This study adopted fluid-structure interaction analysis to assess the hemodynamic and structural loads portending aortic dilatation in patient with different BAV phenotypes.

Keywords—BAV, aortic dilatation, finite element analysis.

I. INTRODUCTION

THE mechanism underlying the development of aortic dilatation in individuals with bicuspid aortic valve (BAV) is an ongoing debate with remarkable implication for surgical treatment [1]. The phenotypic presentation of BAV may include an anterior-posterior cusp-fusion pattern (BAV-AP) or a right-left cusp-fusion pattern (BAV-RL). Dilatation of the aorta due to BAV (namely “bicuspid aortopathy”) may involve either the isolated aortic root or the tubular ascending aorta.

Clinical observations suggest that the progression of an aortic dilatation varies considerably among BAV phenotypes, ranging from normal size development to severely dilated at early ages [2]. The central hypothesis of this study is that a flow-mediated mechanism induced by different BAV phenotypes may increase local aortic wall shear stress causing adverse vascular remodelling and ultimately resulting in proximal dilatation of the ascending aorta. Therefore, we performed two-way fluid structure interaction (FSI) analysis to quantify the hemodynamic and structural parameters likely portending aortic dilatation in BAV.

II. METHODS

A. Clinical data and geometric reconstruction

Electrocardiogram (ECG)-gated CT angiography (CTA) was performed on n.20 patients with different BAV phenotypes and degree of aortic dilatation enrolled from 2011 to 2015. To perform a phenotypic stratification of BAV aortopathy, the classification scheme was extrapolated from that proposed by Schaefer et al. [2]. Specifically, BAV phenotypes were separated in BAV-AP and BAV-RL on the basis of the spatial position of the cusp fusion. The pattern of aortic dilatation was separated in dilatation involving the aortic root (AR) or the tubular ascending aorta (TA) according to the commonly observed shapes of aortic dilatations. Demographic (ie, age and gender) and echocardiographic data (ie, level of stenosis and regurgitation, transthoracic aortic flow) were collected for

each patient.

CTA images were segmented from the aortic valve, through the ascending aorta, the aortic arch and supra-aortic vessels and the descending aorta, ending at the level of the diaphragm using Mimics software. 3D models were then exported to Gambit (ANSYS Inc., Canonsburg, PA) for meshing both fluid (lumen) and structural (aneurysm wall) domains.

B. FSI modelling

Parallel coupled, two-way FSI analyses were performed using the commercial software MpCCI (Fraunhofer SCAI, Germany) to couple the structural component, Abaqus (SIMULIA Inc, Providence, RI), and the fluid solver, Fluent (ANSYS Inc., Canonsburg, PA). Only the systolic peak was simulated and the exchange time step was set to 0.1 s for a total time of 4s, which ensured convergence analysis. Data exchange occurred every time step with Fluent sending the fluid-induced wall forces to Abaqus and Abaqus sending the deformed nodal coordinates to Fluent.

For the structural model, the aortic wall was modelled as a hyperelastic and isotropic composite shell with two layers, which mechanical properties were derived from previous mechanical testing data [3]. Constitutive material parameters were extrapolated from that presented in our previously published FSI simulations [4,5]. Specifically, the model parameters were $\alpha=2.4$ N/cm² and $\beta=34.5$ N/cm² for the inner aortic layer and $\alpha=12$ N/cm² and $\beta=59.5$ N/cm² for the outer aortic layer. Thicknesses were 1 mm and 0.7 mm for the outer layer and inner layer, respectively. For the aorta to deform in physiological way, the distal ends of supra-aortic vessels, aortic valve and descending aorta were fixed in all directions.

For the fluid model, the blood flow was assumed incompressible and Newtonian with a density of 1060 kg/m³ and viscosity of 0.00371 Pa x s. The PISO algorithm was used for pressure-velocity coupling and a 2nd order upwind scheme for discretization of each control volume. Convergence was enforced by reducing the residual of the continuity equation by 10⁻⁵ at all time steps. To include patient-specific flow conditions, the fluid model adopted the trans-aortic flow measurements obtained by Doppler echocardiography as the inflow velocity at aortic valve. This flow was distributed between supra-aortic vessels and descending aorta with a ratio of 40/60. A remeshing technique is used where cells in Fluent are remeshed based on whether they violate a user specified size and skewness criteria. A fluid-dynamics analysis was also performed for each patient to assess the wall shear oscillatory index (OSI).

III. RESULTS AND DISCUSSION

Out of n.20 patients, mean age was 57 ± 13 years with a prevalence of male compared to female. A minimal degree of hypertension was found in few patients whereas a severe degree of aortic insufficiency was found in two patients. These cases were not considered for statistical analysis since they do not represent a clinical dilemma. BAV-AP was observed in n.14 patients and was associated to TA dilatation as compared to AR dilatation (n.10 with TA and n.4 with AR). Differently, BAV-RL occurred in five individuals, with only one case with AR dilatation. Table 1 summarizes patient clinical data.

TABLE I: CLINICAL DATA OF SELECTED PATIENT

<i>Age, years</i>	57 ± 13
<i>Male,</i>	80%
<i>Hypertension,</i>	15%
<i>Aortic Insufficiency</i>	15% none, 60% minimal, 20% moderate, 5% severe
<i>Aortic Stenosis</i>	95% none, 5% moderate
<i>BAV-AP</i>	70%
<i>BAV-RL</i>	30%
<i>TA</i>	90%
<i>AR</i>	10%
<i>Transthoracic Aortic Flow, m/s</i>	2.1 ± 0.7

Note: n=20

For both BAV phenotypes, the flow exhibited a nested right-handed helical pattern with the jet directed toward the right-anterior wall of the ascending aorta (Figure 1). In BAV-RL, the flow jet impinged the aorta in a more distal region compared to that observed in BAV-AP.

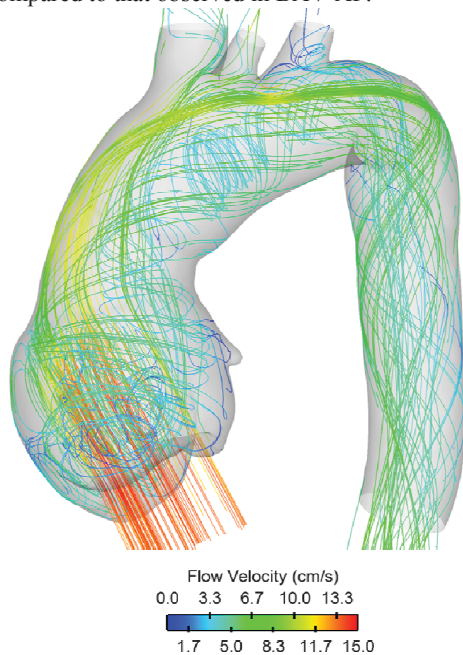


Figure 1: Flow streamlines for a patient with AR dilatation

Wall shear stress (WSS) and OSI were found higher in patients with TA dilatation compared to those with AR dilatation (Figure 2), suggesting a greater risk of aortic enlargement in these individuals. For patients with TA dilatation, WSS and OSI dictated by BAV-RL were found higher in the anterior wall of the ascending aorta compared to those observed in BAV-AP. Local maxima of wall stress and blood pressure occurred in the distal ascending aorta for BAV-RL and closer to sino-tubular junction in BAV-AP. This suggests that the risk of complications related to the development of aortic dilatation differs among individuals with BAV.

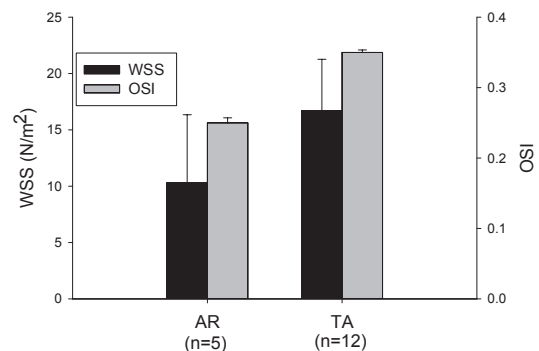


Figure 2: WSS and OSI for patients with AR and TA dilatation

IV. CONCLUSION

Hemodynamic and wall stress in BAV reflect the heterogeneity of bicuspid phenotype and patterns of aortic dilatation. These differences may have a prognostic implication in the progression of bicuspid aortopathy and may be used to stratify subgroups of patients with BAV at greater risk of aortic dilatation.

ACKNOWLEDGEMENT

This study was supported by a 'Ricerca Finalizzata' grant from the Italian Ministry of Health (GR-2011-02348129) to Salvatore Pasta and by a grant from Fondazione RiMED.

REFERENCES

- [1] S Verma et al. *Aortic Dilatation in Patients with Bicuspid Aortic Valve*. N Engl J Med, vol 370, pp. 1920-9, 2014.
- [2] V Rampoldi et al. *Simple risk models to predict surgical mortality in acute type A aortic dissection: the International Registry of Acute Aortic Dissection score*. Ann Thorac Surg. vol 83, pp.55-61, 2007.
- [3] S Pasta et al. *Effect of aneurysm on the mechanical dissection properties of the human ascending thoracic aorta*. J Thorac Cardiovasc Surg.vol.143, pp. 460-7, 2012.
- [4] Pasta et al. *Difference in Hemodynamic and Wall Stress of Ascending Thoracic Aortic Aneurysms with Bicuspid and Tricuspid Aortic Valve*. J Biomech, vol.46, pp. 1729-38, 2013.
- [5] A Rinaudo et al. *Regional Variation of Wall Shear Stress in Ascending Thoracic Aortic Aneurysms*. P I Mech Eng H, vol. 228, pp.627-38, 2014.

Shear-promoted drug encapsulation into red blood cells: a CFD model and μ -PIV analysis

M. Piergiovanni¹, G. Casagrande¹, E. Bianchi¹, M.L. Costantino¹

¹ LaBS, Dept. Chemistry, Materials and Chemical Engineering "Giulio Natta", Politecnico di Milano

Abstract — The present work focuses on the main parameters that influence shear-promoted encapsulation of drugs into erythrocytes. A CFD model was built to investigate the fluid dynamics of a suspension of particles flowing in a commercial micro channel. Micro Particle Image Velocimetry (μ -PIV) allowed to take into account for the real properties of the red blood cell (RBC), thus having a deeper understanding of the process. Coupling these results with an analytical diffusion model, suitable working conditions were defined for different values of haematocrit.

Keywords — Drug encapsulation, Red Blood Cells, CFD model, μ -PIV analysis.

I. INTRODUCTION

CHEMICAL and physical forces are known to induce temporary formation of pores on the membrane of red blood cells and thus allow for the diffusion of molecules inside the erythrocytes, where they are trapped after the closing of the pores [1], [2]. Subsequent haemolysis, either natural or externally induced, causes the release.

Previous studies, performed in our laboratory, showed that a balance between the shear stress applied on the membrane and the molecular diffusion kinetics should be achieved. These two mechanisms, in fact, work in opposite directions:

- high flow rates are required to have shear stresses sufficiently high to induce pore opening;
- low flow rates are necessary to allow the probe molecule diffusion into the RBCs.

In this preliminary study, we hypothesize to use the shear forces arising in a fluid flowing in a microfluidic device to induce the opening of the pores and allow for the diffusion of a probing molecule into the cell.

II. MATERIAL AND METHODS

A. Computational model

A computational model was developed using COMSOL Multiphysics 4.2a, representing a commercial micro channel (50x50 μ m cross-section, 58.8 mm length). The *Mixture Model, Laminar Flow* was used to evaluate velocity, volume fraction of dispersed phase and estimate shear stress on RBCs (τ_{RBC}), using Casson equation. This model accounts for rigid, spherical particles ($d_{RBC} = 8 \mu$ m). The diffusion dynamic of a probing molecule (dextran, MW = 40000) was analytically modelled to evaluate the minimum time (t_{min}) required to guarantee the diffusion of the molecule into the RBCs: a corrective coefficient of 1.5 was applied to t_{min} in order to

account for the not-instantaneous nature of the pore opening mechanism.

The conditions were considered suitable to promote encapsulation when both the following requirements were satisfied:

- the pair of τ_{RBC} values and transit time results nearly haemolytic, according to the Tillman diagram [3];
- t_{min} has to be shorter than the residence time of the RBC into the channel.

An appropriate efficiency index was defined to identify the flow conditions mainly promoting the encapsulation: velocity, distribution of the particle in the channel and applied shear stress.

B. μ -PIV analysis

The high number of particles involved in the process do not allow the simultaneous simulation of the RBCs deformability with the CFD model. At the same time it should be highlighted that the developed model is not intended to accurately describe the physics of mechanical haemolysis, but to determine the average position of the RBCs in the microchannel.

However, to overcome these limitations and to have a deeper understanding of the process, experimental activity was performed using μ -PIV analysis, a technique already used in the literature to evaluate blood velocity both *in vivo* [4] and *in vitro* [5]. Using a commercial micro channel, it was possible to evaluate the impact of RBCs real mechanical properties and behaviour on the actual fluid dynamic. Flow rates of 30 and 50 μ l/min were tested. Table I summarises the suspension composition used during experiments. The volume of fluorescent particles (V_P) contains 0.1% fluorescent micro particles (polystyrene, diameter: 1 μ m, $\rho = 1.06 \text{ g/cm}^3$) in distilled water. The PBS was a solution 1M, pH=7.2. Both were purchased from Thermo Fisher Scientific (Waltham, MA USA). Red cells were supplied by SIMT, Istituto Nazionale dei Tumori. The blood sample were taken from informed and consentient donors.

TABLE I
SOLUTION USED FOR MICRO-PIV EXPERIMENTS

$V_{RBC} [\mu\text{l}]$	$V_{PBS} [\mu\text{l}]$	$V_P [\mu\text{l}]$	V_{TOT}	Ht [%]
12	588	300	900	1.3

The use of suspensions with a higher haematocrit was not performed due to the technical limitations in the optical system used.

III. RESULTS AND DISCUSSION

Taking into account the conditions promoting encapsulation, with the pair of τ_{RBC} values and transit time nearly haemolytic, and RBCs transit time higher than the dextran diffusion time, based on the outputs of the diffusion model, four different conditions were identified and subsequently analysed. The flow rates calculated with the diffusion model are the maximum values that should be applied in order to guarantee the correct diffusion time of the probing molecule into a single RBC.

From the CFD analysis the sub haemolytic flow conditions suitable to promote dextran encapsulation were identified for different Ht (Figure 1). The computational model also allows to verify the absence of RBCs deposition along the channel, so that all the flowing cells can be involved in the encapsulation process. The efficiency of the process, evaluated using the specifically defined index, results higher in the round crown region of the flow section, with radius $0.4R < r < 0.6R$, where R is the hydraulic radius of the channel. This results agree with observations made for similar geometries [6], where the RBCs underwent axial migration till an equilibrium position at $0.6R$ (so-called “pinch effect”).

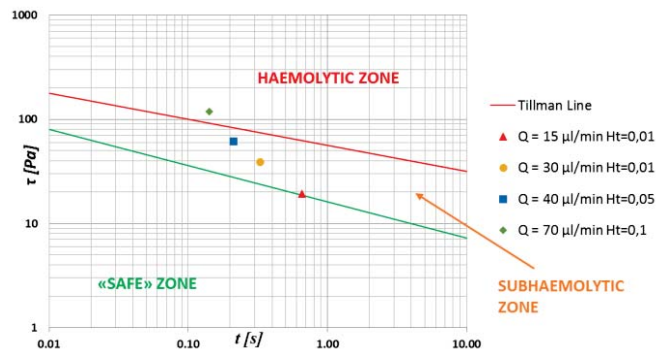


Figure 1: Pairs of value τ_{RBC} – t from the CFD at varying Ht and Q.

The experimental approach revealed that the velocity profiles (and the derived shear stress) were lower than the predicted ones, but still near Tillman haemolytic line (Figure 2).

The flow rates (Q), suitable to promote encapsulation, at different haematocrit, were identified in: 30 $\mu\text{l}/\text{min}$ for $Ht = 0.01\%$, 40 $\mu\text{l}/\text{min}$ for $Ht = 0.05\%$, 70 $\mu\text{l}/\text{min}$ for $Ht = 0.1\%$.

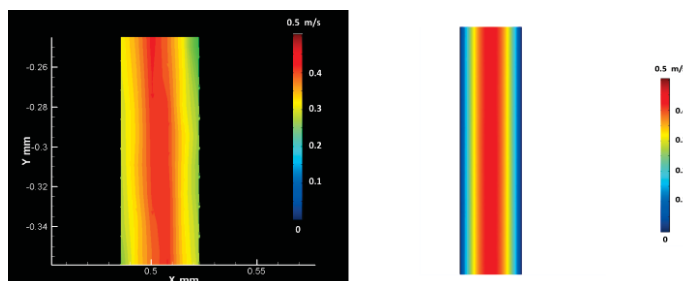


Figure 2: Velocity field from μ -PIV analysis and CFD model for $Q = 30 \mu\text{l}/\text{min}$ and $Ht = 0.01$.

IV. CONCLUSION

This study provides the preliminary knowledge to control the process of stress-promoted encapsulation of molecules into RBCs flowing in a micro channel.

Coupling the results from the computational model and μ -PIV analysis, it was possible to identify suitable working conditions that will be used in the forthcoming encapsulation tests.

These results also suggest the introduction of a previous focusing step, so that most of the cells would follow paths through maximum efficiency region.

REFERENCES

- [1] V.R. Muzykantor, “Drug delivery by red blood cells: vascular carriers designed by mother nature”, in *Expert opinion on drug delivery*, 7:403-427, 2010;
- [2] F. Pierige, S. Serafini, L. Rossi, M. Magnani, “Cell-based drug delivery”, in *Advanced drug delivery reviews*, 60:286-295, 2008;
- [3] W. Tillman, H. Reul, M. Herold, K.H. Bruss, J. Gilse, “In-vitro wall shear measurements at aortic valve prostheses”, in *Journal of Biomechanics*, 17:263–279, 1984;
- [4] Y. Sugii, S. Nishio and K. Okamoto, “In vivo PIV measurement of red blood cell velocity field in microvessels considering mesentery motion”, in *Physiological measurements*, 23:403-416, 2002;
- [5] R. Lima, S. Wada, M. Takeda, K.I. Tsubota, T. Yamaguchi, “In vitro confocal micro-PIV measurements of blood flow in a square microchannel: The effect of the haematocrit on instantaneous velocity profiles”, in *Journal of Biomechanics*, 40:2752–2757, 2007;
- [6] R. Lima, T. Ishikawa, Y. Imai, M. Takeda, S. Wada, T. Yamaguchi, “Radial dispersion of red blood cells in blood flowing through glass capillaries: The role of haematocrit and geometry”, in *Journal of Biomechanics*, 41:2188–2196, 2008;

An automated adaptive bioreactor – based platform for culturing Cardiac Tissue Models

G. Pisani¹, D. Massai¹, A. Rodriguez¹, G. Cerino², R. Galluzzi¹, G. Falvo D'Urso Labate³, C. Bignardi¹, A. Tonoli¹, A. Audenino¹, A. Marsano², U. Morbiducci¹

¹ Politecnico di Torino, Turin, Italy

² University and University Hospital of Basel, Basel, Switzerland

³ Bioexpansys Srl, Turin, Italy

Abstract — An automated bioreactor-based system for the adaptive culture of cardiac tissue-engineered models has been developed. The system is able to monitor the milieu parameters in real-time, to reproduce physiological-like and pathological-like mechanical stimuli, and to non-destructively monitor and characterize the physical responses of the mechanically stimulated constructs along the culture. The bioreactor monitoring and control system allows to automatically adapt the applied stimulation to the construct maturation phase in real time. The proposed platform represents a very promising tool (1) for an in-depth investigation on cardiac tissue maturation and remodeling, (2) for drug screening and disease modeling studies, and (3) for an optimized production of cardiac tissue models.

Keywords — cardiac tissue engineering, bioreactor, real-time monitoring, adaptive mechanical stimulation, non-destructive monitoring.

I. INTRODUCTION

CARDIAC regenerative medicine requires investigation on cardiac tissue developmental aspects and factors that influence the generation of functional tissues [1], [2], [3]. The possibility for a challenging tight and adaptive control of individual parameters (separated from *in vivo* systemic effects), could assess the effects of biochemical and physical stimuli on cardiac tissue maturation and function. To meet this challenge, an automated bioreactor-based system has been developed for culturing cardiac tissue models *in vitro* in an environment where tissue maturation is achieved under real-time monitored and controlled conditions. This platform has been designed to provide native-like biochemical and biophysical stimuli that can be dynamically and automatically adapted to the maturation phase of the cultured constructs. The rationale is to overcome limitations of the current bioreactor-based approach, where the stimuli are not real-time adapted to the maturation of the construct.

The system proposed here allows for the application of a more realistic biomimetic stimulation strategy. In particular, the system allows to quantitatively monitor the maturation phase of the construct and to adapt the dynamic culture conditions (i.e. stretch magnitude/stretch-mode) to the evolution phase.

II. MATERIALS AND METHODS

The platform is composed of a bioreactor, designed to be incubated, easy to handle, and easy to sterilize (by autoclave and UV radiations), and the engineered cardiac tissue rings.

The bioreactor (Fig. 1) consists of three main components: 1) a culture chamber; 2) a mechanical stimulation system; 3) a monitoring and control system.

The culture chamber is a transparent autoclavable rectangular vessel (140 x 80 x 75 mm³ with a priming volume of ~100 ml), realized in polycarbonate (Fig.1a). Two interchangeable sample holders allow to house engineered cardiac tissue rings and patches. On the lid of the culture chamber, an optical access allows the visual inspection of the constructs during the dynamic culture. The chamber filling/emptying as well as the medium replacement is ensured by the inlet and outlet ports on the lid. The mechanical stimulation system (Fig.1b) includes a linear actuator, that allows to supply controlled cyclic stretch to the constructs (up to 200% deformation, frequency range 1-10 Hz), and a position transducer (displacement resolution ~ 15µm). The monitoring and control unit (Fig. 1c), based on feedback loop with real-time communication and processing, is composed of: 1) removable sensors (temperature, pH, CO₂, O₂ and force); 2) an embedded controller (Data Acquisition Modules and a compactRIO, National Instruments); 3) a dedicated computer; 4) a custom-made software with a user-friendly interface suitable for setting and monitoring the operating culture conditions and, through the feedback loop, for the automatic control and adaptation of the stimulation (based upon the measured quantities).

In addition to the real-time monitoring and recording of the milieu parameters, thanks to the presence of a force sensor (XFTC300, 10N full scale) it is possible to measure in real-time the force developed by the construct during the stimulation and to non-destructively characterize its mechanical behavior. The monitoring of the construct, being part of the feedback loop, allows for a force-based adaptive control of the dynamic culture depending on the construct maturation (i.e., on its current mechanical properties).

Engineered cardiac constructs have been developed starting from preliminary tests dedicated to assess the optimal fibrin gel mixture. Rat cardiac fibroblasts were embedded in fibrin gel at a density of 1x10⁶ cells/ml. Fibrinogen (50 mg/mL) was dissolved in saline (0.9% w/v of NaCl) solution. Aprotinin (1000 IU per mL of solution) was added to the solution under mild stirring. Polymerization of fibrinogen was achieved by the addition of a 100 IU/mL thrombin solution (0.1 IU per mg fibrinogen). Solution was transferred into a 24-well plate, cast into circular molds (external diameter = 16 mm, internal diameter = 12 mm, height = 3 mm) and incubated at 37°C for 2 hours until

polymerization (Fig. 2). The cardiac constructs were then cultured for 7 days under mechanical stimulation (1Hz; 2, 5 and 10% deformation) (Fig. 3). The use of 3D rings as cardiac construct shape allows the application of homogeneous load [4].

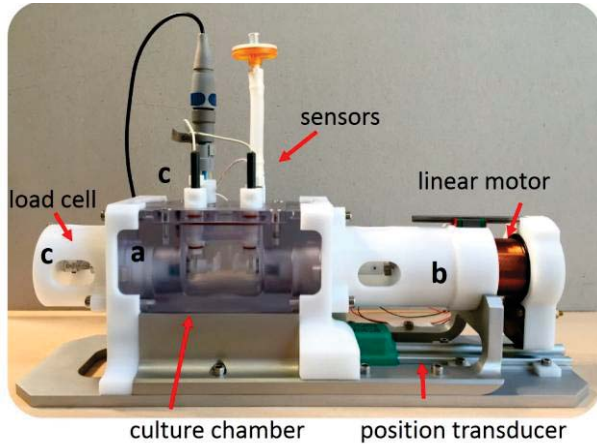


Fig. 1 – Bioreactor components: a. culture chamber; b. linear motor and position transducer; c. T, O₂, CO₂, pH and force sensors



Fig. 2 – Engineered cardiac tissue ring



Fig. 3 – Cardiac construct under mechanical stimulation

III. RESULTS

In-house tests confirm the bioreactor biocompatibility and sterility maintenance, the performances of the monitoring and stimulation units, and the culture process automation.

Moreover, preliminary results demonstrated the feasibility to obtain reproducible cardiac constructs able to withstand at the mechanical stimulation up to 1Hz and 10% of deformation for one week. Histological analysis are ongoing to assess the effects of the mechanical stimulation on the cardiac fibroblast phenotype and alignment.

IV. CONCLUSION

A bioreactor-based model system for biomimetic adaptive stimulation culture of cardiac tissue models has been developed.

This automated, adaptive platform is a very promising tool for acquiring in-depth knowledge on the cardiac tissue growth and remodeling processes, and will be also useful for drug screening and disease modeling research. Moreover, the use of a closed and almost operator-independent system will assure greater reproducibility, traceability, scalability, and lower contamination risk than traditional manual processes, finally maximizing the efficiency of the cardiac tissue models investigation and production. In the near future, engineered cardiac tissues will be employed for assessing the influence of the mechanical stimulation on cardiomyocyte maturation and ultrastructure organization.

REFERENCES

- [1] G. Vunjak-Novakovic, N. Tandon, A. Godier, R. Maidhof, A. Marsano, T.P. Martens, M. Radisic, "Challenges in cardiac tissue engineering", *Tissue Engineering Part B Review*, 2010, 16(2):169-187
- [2] D. Massai, G. Cerino, D. Gallo, F. Pennella, M.A. De Riu, A. Rodriguez, F.M. Montecvecchi, C. Bignardi, A. Audenino, U. Morbiducci, "Bioreactors as Engineering Support to Treat Cardiac Muscle and Vascular Disease", *Journal of Healthcare Engineering*, 2013, 4(3):329-370
- [3] G. Vunjak Novakovic, T. Eschenhagen, C. Mummery. Myocardial tissue engineering: In Vitro Models. Cold Spring Harbor Perspectives in Medicine 2014; 4(3)
- [4] W.H. Zimmermann, C. Fink, D. Kralish, U. Remmers, J. Weil, T. Eschenhagen, "Three-dimensional engineered heart tissue from neonatal rat cardiac myocytes" *Biotechnology and Bioengineering*, 2000, 68(1):106-114

A porous media foot model integrating gait analysis: proof of concept in a diabetic neuropathic subject

M. Pizzocaro¹, A. Guiotto², G. Sciumè³, Z. Sawacha², C. Cobelli², D.P. Boso¹ and B.A. Schrefler¹

¹ Department of Civil, Environmental and Architectural Engineering, University of Padova, Padova, Italy.

² Department of Information Engineering, University of Padova, Padova, Italy.

³ Department of Innovation Engineering, University of Salento, Lecce, Italy.

Abstract—A computational foot model based on porous media mechanics is proposed here as an aid in diabetic ulcer prevention. The soft plantar tissue is modelled as a system consisting of two phases: one solid for the tissue cells and their extracellular matrix, and one fluid (interstitial fluid). Bones, cartilages and ligaments are linear elastic. The load history and boundary conditions are taken from the experimental measurements performed: the acquisition of in-vivo foot kinematics and magnetic resonance imaging give the input data of the model. The case of a diabetic neuropathic patient is presented.

Keywords—Porous media, gait analysis, diabetic foot, stress peaks.

I. INTRODUCTION

DIABETES, and in particular diabetic neuropathy, have their main biomechanical effect on the lower limb and may lead to diabetic foot pathology and foot ulcerations.

Gait analysis allows for the acquisition of kinematics and ground reaction forces (GRFs) during gait, and *three-dimensional finite element (FE) modelling* allows for obtaining the stress and strain fields developed in the different internal structures of the foot. In the literature on FE foot models, the soft tissue is almost always considered as a hyperelastic material [1]–[5]. A hyperelastic constitutive law is a simplification; actually it behaves like a viscoelastic material as observed experimentally [6]. If the viscous nature of the soft foot tissue is taken into account, *time* (therefore the duration of the gait cycle) has a sensible impact on tissue strain, which is otherwise disregarded by using linear elasticity or hyperelastic models.

In this paper, a method to model properly one or more gait cycles and the associated plantar pressures as a function of time is presented. This method integrates experimental data of patient-specific foot kinematics with the modelling process. With respect to the existing formulations, it is a truly *time dependent model* where attention is paid to the real micro-structure of the plantar tissue, which is modelled as a *porous medium* filled by an interstitial fluid.

Porous media mechanics has already been exploited in biomechanical modelling, for example to simulate intervertebral disc behaviour [7] or tumour mass growth [8]. Here that framework is applied to plantar tissue modelling, so that a more realistic material behaviour is obtained: stress transfer from fluid to the solid phase and vice versa occurring inside the tissue can be taken into account, thus resulting in a global viscoelastic response of the material [9].

II. METHODS

3D foot gait analysis was carried out as in [10] on a diabetic neuropathic subject: age 71 years, BMI 37 kg/m², with type 2 diabetes, affected also by peripheral neuropathy and vasculopathy, HbA1c of 8.6%, with cavus foot, valgus heel, claw toes and callosities under the metatarsal heads. Experimental setup included a 6-camera motion capture system (60-120 Hz, BTS S.r.l, Padova), 2 force plates (FP4060-10, Bertec, USA) and 2 plantar pressure (PP) systems (Imagotresi, Piacenza). The signals coming from all systems were synchronized.

The hindfoot, midfoot and forefoot subsegments as well as tibia 3D kinematics, GRF and PP were calculated as in [10]. The protocol was approved by the local ethic committee. A right foot MRI (Siemens Avanto, 1.5 T, Spacing between slides: 0.7mm, Slice thickness: 1.5mm) was acquired and a FE discretization was generated as in [5]: the MRI was segmented with Simpleware ScanIP (v.5.0), meshed with ScanFE module and imported into Abaqus.

III. MODELLING ASPECTS

Subject-specific kinematics and GRFs are input data for the numerical model. Ligaments, bone, cartilage are considered linearly elastic, while the soft tissues are considered as an elastic porous medium in the large strain regime with the pore space completely filled by a fluid phase. The tissue cells and their extracellular matrix form the solid skeleton with pores saturated by the interstitial fluid.

A cut of the 3D FE mesh of the soft tissue (in blue), of the bone segments (in green), of the cartilages (in grey), and of an aluminium surface (in red) supporting the foot, is represented in Figure 1. Material properties were obtained from the literature and are summarized in Table I. The elastic modulus of the dried soft tissue is assumed as 1 MPa. This Young's modulus is higher than values measured in some slow-loading plantar tissue studies [6]. However this relatively high modulus value compensates for neglecting high strain rate stiffening effects and accounts for the increase of elastic modulus at large strains in the hyperelastic tissue behaviour, as it is expected to occur in the plantar tissue during gait (similar values are used in [11], [12]). No experimental data have been found in the literature for the intrinsic permeability of the plantar tissue. In this work, it is assumed equal to $2 \cdot 10^{-13} \text{ m}^2$, the same order of magnitude found in [13], where a comparable tissue is analysed. The

mechanical parameters of bones and cartilages are assumed according to [1].

TABLE I
MATERIAL PROPERTIES

Parameter	Value	Unit
Young's modulus of the bones	7300	MPa
Poisson's ratio of the bones	0.3	-
Young's modulus of the dried soft tissue	1.0	MPa
Poisson's ratio of the dried soft tissue	0.4	-
Young's modulus of the cartilages	1.01	MPa
Poisson's ratio of the cartilage	0.4	-
Intrinsic permeability of the tissue	$2 \cdot 10^{-13}$	m^2

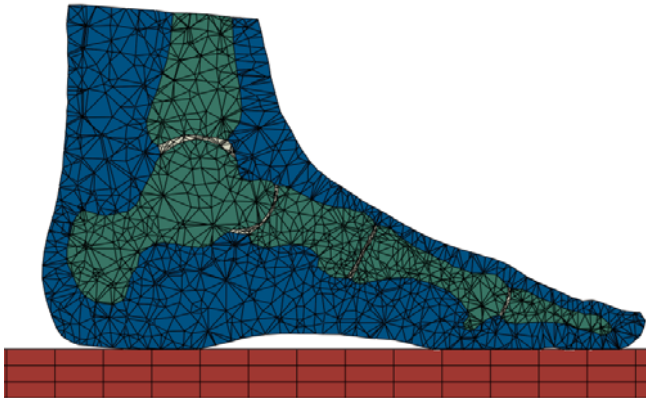


Figure 1. A cut of the three dimensional finite element mesh of the foot

IV. NUMERICAL RESULTS

The presence of the interstitial fluid in the pores allows mimicking of the real global viscoelastic behaviour of the plantar soft tissue. In Figure 2 the map of the interstitial fluid pressure is presented, and in Figure 3 the corresponding effective stress field in the tissue solid skeleton is shown.

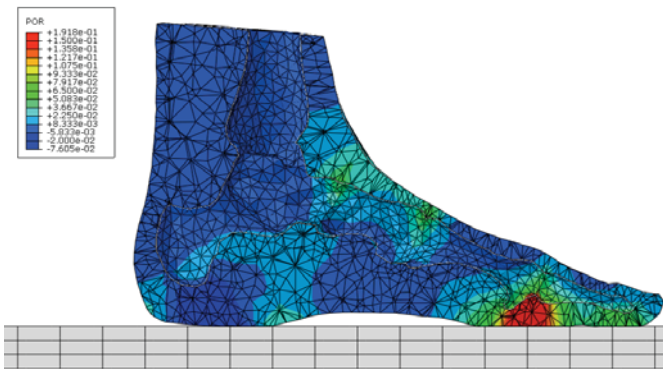


Figure 2. Interstitial fluid pressure [MPa] at the instant $t= 0.2715$ s.

V. CONCLUSION AND FUTURE PERSPECTIVE

A real case of a diabetic neuropathic patient is reported to show the potentiality of the method and the resulting fields made available by numerical FE simulation. The presence of the interstitial fluid in the pores allows mimicking the real global viscoelastic behaviour of the plantar soft tissue. In the near future, the tissue vascularization and its efficiency will be taken into account, to obtain a model which can be useful for better understanding the bio-chemo-mechanical processes

involved in foot ulceration and its progression. Although porous media analysis has been used previously in biomechanical simulations, to our knowledge it has not been applied to plantar tissue modelling and prediction of diabetic wounds.

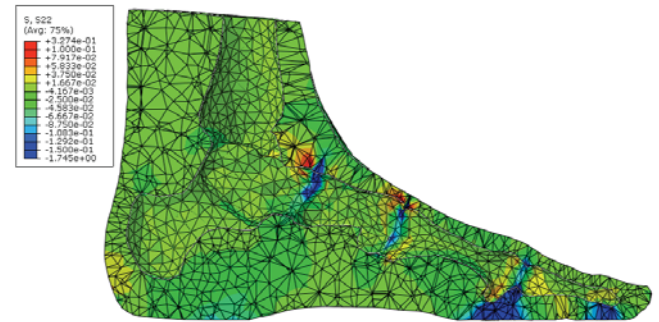


Figure 3. Stress field [MPa] in the solid skeleton at the instant $t= 0.2715$ s.

ACKNOWLEDGEMENT

The partial support by the Italian National Research Project CPDA135240 'Development of a multiphysics diabetic foot model for plantar ulcers prevention in diabetic subjects' is gratefully acknowledged.

REFERENCES

- [1] W.-M. Chen, T. Lee, P.V.-S. Lee, J.W. Lee, and S.-J. Lee, "Effects of internal stress concentrations in plantar soft-tissue-A preliminary three-dimensional finite element analysis," *Med Eng Phys*, vol. 32, pp. 324–331, 2010.
- [2] J. T.-M. Cheung, M. Zhang, A.K.-L. Leung, and Y.-B. Fan, "Three-dimensional finite element analysis of the foot during standing - A material sensitivity study," *J Biomech*, vol. 38, pp. 1045-1054, 2005.
- [3] A. Erdemir, et al., "Local plantar pressure relief in therapeutic footwear: design guidelines from finite element models," *J Biomech*, vol. 38, pp. 1798-1806, 2005.
- [4] S. Goske, A. Erdemir, M. Petre, S. Budhabhatti, and P.R. Cavanagh, "Reduction of plantar heel pressures: Insole design using finite element analysis," *J Biomech*, vol. 39, pp. 2363-2370, 2006.
- [5] A. Guiotto, Z. Sawacha, G. Guarneri, A. Avogaro, and C. Cobelli, "3D finite element model of the diabetic neuropathic foot: A gait analysis driven approach," *J Biomech*, vol. 47, pp. 3064–3071, 2014.
- [6] A. Gefen, M. Megido-Ravid, and Y. Itzhak, "In vivo biomechanical behavior of the human heel pad during the stance phase of gait," *J Biomech*, vol. 34, pp. 1661-1665, 2001.
- [7] W. Ehlers, N. Karajan, and B. Markert, "An extended biphasic model for charged hydrated tissues with application to the intervertebral disc", *Biomech. Model Mechanobiol.*, vol. 8, pp. 233-251, 2009.
- [8] G. Sciumè, R. Santagiuliana, M. Ferrari, P. Decuzzi, and B.A. Schrefler, "A tumor growth model with deformable ECM", *Physical Biology*, Vol. 11, Article number 065004, 2014.
- [9] G. Sciumè, D.P. Boso, W.G. Gray and B.A. Schrefler, "A two-phase model of plantar tissue: a step toward prediction of diabetic foot ulceration," *Int J Numer Meth Biomed Engng*, vol. 30, pp. 1153–1169, 2014.
- [10] Z. Sawacha, et al., "Integrated kinematics–kinetics–plantar pressure data analysis: A useful tool for characterizing diabetic foot biomechanics", *Gait & Posture*, vol. 36, pp. 20–26, 2012.
- [11] G. Yarnitzky, Z. Yizhar, and A. Gefen, "Real-time subject-specific monitoring of internal deformations and stresses in the soft tissues of the foot: A new approach in gait analysis," *J Biomech*, vol. 39, pp. 2673-2689, 2006.
- [12] I.R. Spears, J.E. Miller-Young, M. Waters, and K. Rome, "The effect of loading conditions on stress in the barefooted heel pad," *Medicine and Science in Sports and Exercise*, vol. 37, pp. 1030-1036, 2005.
- [13] A. Fahlgren, L. Johansson, U. Edlund, and P. Aspenberg, "Direct ex vivo measurement of the fluid permeability of loose scar tissue," *Acta Bioeng Biomech*, vol- 14, pp 47-51, 2012.

Patient-specific CFD of the aortic haemodynamics: Bringing cardiovascular virtual reality to clinical bedside practice

L. Antiga¹, F. Auricchio², M. Conti², A. Lefieux³, S. Morganti², A. Reali², R.M. Romarowski^{2*}, F. Secchi⁴, C. Trentin³, S. Trimarchi⁴ and A. Veneziani⁵

¹ *Orobix s.r.l., Bergamo, Italy*

² *University of Pavia, Pavia, Italy*

³ *IUSS Pavia, Pavia, Italy*

⁴ *IRCCS Policlinico San Donato, Milan, Italy*

⁵ *Emory University, Atlanta, USA*

Abstract— With the development of new and more powerful computing systems, computational fluid dynamics (CFD) has become a widespread topic of interest for researchers all over the world. In particular, its application to blood flow in the aorta has the potential to give information that cannot be retrieved in other ways. Even though many groups are working hard to improve the current scope of the topic, the technology is not yet available in the hospitals to be used both for diagnosis and treatment. In this work, we propose a framework to take numerical simulation to the bedside. All the stages from image acquisition, pre-processing, calculations, post processing and interpretation are addressed and shown for a single patient case. We conclude that, given the feasibility of the stages and the current computational power, this analysis can be satisfactorily applied to support clinical practice

Keywords— CFD, aorta, patient specific modelling, high performance computing

I. INTRODUCTION

REALISTIC computer-based simulation tools are widely studied and developed in the field of cardiovascular biomechanics with the aim to provide diagnostic and therapeutic solutions thanks to their capability of assessing real and virtual scenarios both in the medical room and during the pre-operative planning.

Unfortunately, such simulations are currently adopted only by a small number of real-life case studies and are still limited to research, whereas their actual translation to clinical practice has to face different challenges ranging from the assimilation and managing of clinical data (big data) to the integration of the required multidisciplinary skills.

The goal of this study is to present a developing project identified as *iCardioCloud*, which, grounding its motivation on the above-mentioned issues, aims at actually bringing patient-specific CFD analysis of aortic haemodynamics, before and after endovascular surgery, into the clinical practice [1]. All the steps from the image acquisition, processing, numerical simulations on high performance computers, post processing and, finally, end user visualization of the data are addressed. The research team is composed by engineers and physicians (surgeons and radiologists) in order to cover all the required skills to realize the ideal workflow depicted in Figure 1.

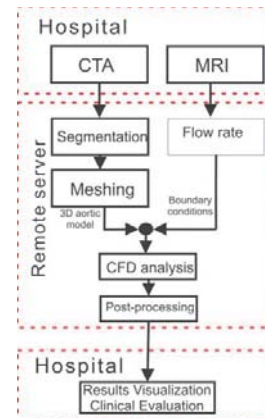


Figure 1: iCardioCloud workflow

II. METHODOLOGY

A. Image acquisition, image processing and mesh generation

For patients with suspected thoracic aorta diseases such as aneurysms, dissections and coarctations, CT images are acquired in the hospital. Furthermore, Velocity Encoded MRI (VE-MRI) is performed to record the flow profiles in all the inputs and outputs from the aorta. All this information is sent anonymized from the clinical institution to our engineering platform. Figures 2 and 3 illustrate rough and extracted information received from the hospital respectively.



Figure 2: MRI showing the aneurysm.

*Corresponding author. Email: rodrigo.romarowski@unipv.it

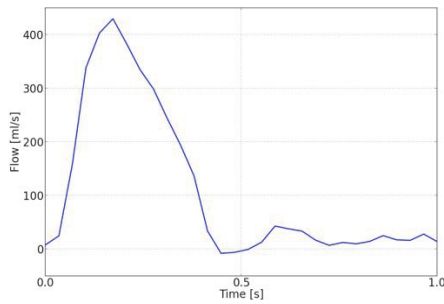


Figure 3: flow profile in the ascending aorta extracted from VE-MRI

Once the images are in our database, CT is pre-processed and segmented in order to obtain a 3D surface reconstruction of the aortic lumen. The 3D model is then processed through a pipeline that leads to the generation of a CFD-suitable mesh in a semi-automatic way.

The pipeline of operations are performed via the Vascular Modelling Toolkit (www.vmtk.org) and it consists primarily, in cropping the surface at the in- and out-flow section. The computational domain is artificially extended, by inserting at the boundary sections, cylindrical region called flow extensions and the mesh generation step is performed, with local refinement if necessary, using tetrahedral elements of pre-defined edge length. The result of this step is depicted in Figure 3.

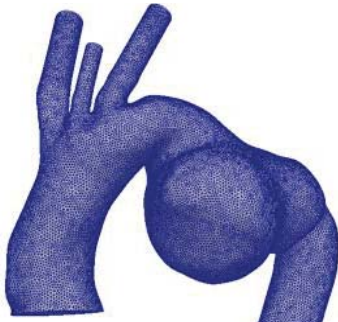


Figure 3: Aneurysm zone showing the result of the meshing procedure

B. CFD simulation

The patient specific mesh and boundary conditions are then loaded into the Finite Element Analysis software. We use the open-source C++ library LifeV (<http://www.lifev.org>), developed by some of the authors within a collaborative project including EPF Lausanne, Politecnico di Milano, INRIA Paris, and Emory University. The reason for choosing this software is that it has the flexibility to adopt many types of boundary conditions, is open source and it can easily scale for parallel processing. Taking into account the size of the meshes and the target accuracy of the simulations, we use a high performance cluster to perform the calculations. This capability allows retrieving the information to the physician in time to decide whether a surgery is needed or not. After performing the numerical analysis, different ad-hoc tools developed by our group are used to provide a more visual and 'medical' representation. Both images and animations are created for velocity field, pressure along the vessel and Wall Shear Stress (WSS). All these parameters were chosen due to their well-known correlation with cardiovascular events.

In the final stage, data is returned to the hospital from our database and the physician can make both a diagnosis and a predictive analysis for each patient.

III. RESULTS AND CONCLUSIONS

To illustrate the potential of the project, we show a single patient case with an aortic aneurysm. For this case we used a 3,5 million elements mesh with P1Bubble-P1 finite elements for velocity and pressure space respectively. The simulation was performed in a 64 core server with 256GB RAM where the whole process took one week. The results are represented in terms of velocity, pressure and WSS as show in figure 4.

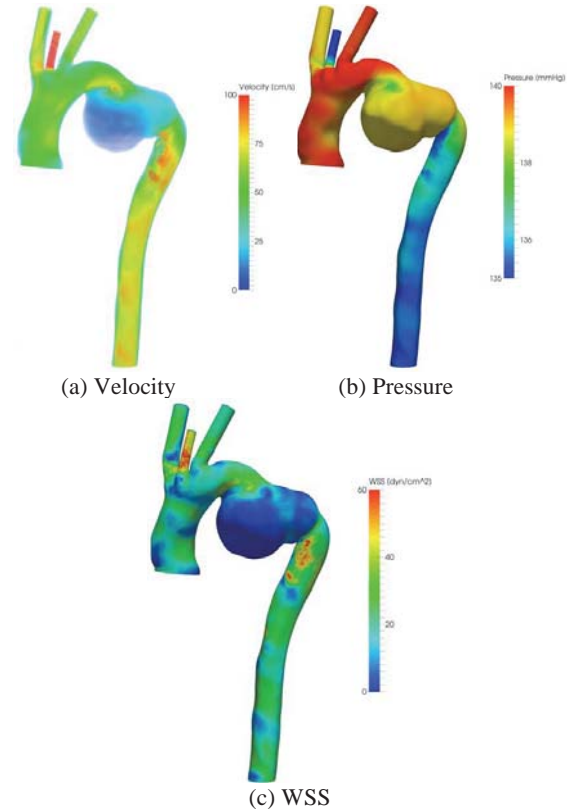


Figure 4: Instantaneous values at the systolic peak taken from the CFD simulation

After watching this results and taking into account the times and availability of resources in current medical practise, we conclude that this framework is currently applicable for diagnosis and planning of surgeries such as TEVAR, etc. The obtained physical quantities can be translated into clinical information (e.g., prediction of aneurysm growth [2]). Thus, they can support the physicians on both a better understanding of the patient's pathology and on procedure planning. For this reason, in the final stage, data are always returned to the hospital, from our database to the bedside. Short-term future developments include the prediction of postoperative haemodynamic behaviour based on postoperative virtual surgery models.

REFERENCES

- [1] F. Auricchio, M. Conti, A. Lefieux, S. Morganti, A. Reali, F. Sardanelli, F. Secchi, S. Trimarchi, A. Veneziani, "Patient-specific analysis of post-operative aortic hemodynamics: a focus on Thoracic Endovascular Repair (TEVAR)" in *Comput Mech* 54, no. 4, 2014, pp.943-953.
- [2] L. Boussel, V. Rayz, C. McCulloch, A. Martin, G. Acevedo-Bolton, M. Lawton, R. Higashida, W. Smith, W. Young, D. Saloner, "Aneurysm growth occurs at region of low wall shear stress patient-specific correlation of hemodynamics and growth in a longitudinal study" in *Stroke* 39, no. 11, 2008, pp. 2997-3002.

LIGHTarm: an exoskeleton for upper-limb neurorehabilitation

Alessandro Scano^{1,2}, Giulio Spagnuolo^{1,2}, Marco Caimmi^{1,2}, Andrea Chiavenna¹, Matteo Malosio^{1,2}, Giovanni Legnani², Lorenzo Molinari Tosatti¹

¹ Istituto di Tecnologie Industriali e Automazione, Consiglio Nazionale delle Ricerche, Milano, Italy

² Università di Brescia, Italy

Abstract—This paper presents the prototype of LIGHTarm, an exoskeleton for neuro-rehabilitation whose main feature is the low cost, not actuated design, capable of providing weight support and good transparency features. Our first experimental trials on three healthy subjects investigated such characteristics by comparing the kinematics and the EMG activity of the main muscles involved in functional daily life motor tasks.

Keywords—exoskeleton, rehabilitation, upper limb, transparency.

I. INTRODUCTION

Stroke is one of the leading causes of long-term disability and impairment in US and Europe [1].

At the state of the art, there are several possibilities in rehabilitation practice to reduce motor impairment and to improve upper-limb functionality in stroke.

Weight support is fundamental in the exploration of the workspace as it allows discharging the muscles from the burden of supporting the limb against gravity, affecting the capability of performing the most part of functional motor tasks [2], and reducing the influence of abnormal coupling (flexural-synergies) between shoulder and elbow **Errorre.**

L'origine riferimento non è stata trovata. Exoskeleton-based devices, replicating the kinematics of the limb, are more suitable to properly gravity compensate the upper-limb weight in an extensive range of motion. Patients treated with the passive exoskeleton Armeo Spring showed moderated but statistically significant improvements [2].

Unfortunately, remarkable drawbacks of commercial exoskeletons are the only partial backdrivability in singular kinematic configurations of the elbow (ES) and the low adaptability to the shoulder rhythm, that is the physiological movement of the shoulder. Exoskeletons backdrivability (i.e. transparency) is a desirable feature in rehabilitation practice [4, [5]. Transparency is needed to allow the exploration of the causal relationship between effort end errors [3] that is considered as crucial in the process of motor re-learning.

In this paper, *LIGHTarm* is presented. It is a passive and gravity-compensated exoskeleton for upper-limb neuro-rehabilitation based on a peculiar kinematic structure, specifically conceived to maximize the transparency and face the elbow-singularity issue [7]. An experimental campaign has been designed to test gravity support features and transparency in static and dynamic conditions.

II. MATERIALS AND METHODS

A. LIGHTarm design e description

The peculiar LIGHTarm kinematic architecture was conceived to: 1) avoid the exoskeleton and human shoulder and bones origins to coincide, thus enabling the human shoulder to move compatibly with the physiological shoulder rhythm; 2) avoid the singularity configuration of the exoskeleton in the whole upper-limb range of motion. These features, together with low inertia and low frictions, should guarantee a good transparency, allowing the exoskeleton to accurately follow the upper-limb movements in a large exploitable range of motion, without incurring in mechanical locks of the device. A gravity-balanced mechanism supports the weight of the limb. In order to partially decouple the gravitational load contributions of the upper-arm and the forearm segments, the designed gravity-balancing system is made up of a combination of two mechanical elements: a spring-based system acts on the elbow joint and a counterbalance system on the shoulder one. In addition, a four-bar linkage is provided to make the counterbalance system independent of the forearm orientation. A proper counterweight W_s counterbalances the gravitational torque perceived at shoulder level.

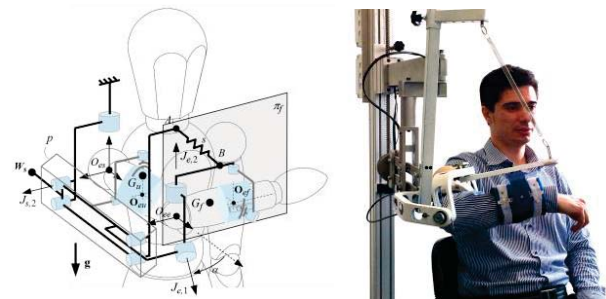


Fig. 1. LIGHTarm kinematic scheme and prototype

B. Aim of the work

The aim of the study is twofold.

Firstly, to experimentally test the LIGHTarm weight support characteristics in significant configurations.

Secondly, to experimentally investigate LIGHTarm transparency during the execution of functional motor tasks.

C. Participants and trials

Three healthy subjects were enrolled for this study: age 32.7 ± 11.9 , height 181 ± 2 cm, weight 77 ± 8 kg, 3M, all right-handed. Trials were given an alphanumeric ID as shown in Tab I, and were all executed with and without weight support. In order to investigate *weight support*, the activity of Deltoid Anterior (DA) muscle, the main shoulder elevator in the sagittal plane, was recorded in three static configurations (Fig.2). In order to investigate *transparency* during motion, three dynamic tasks were designed: the Reaching against Gravity (RCH), the Hand-to-Mouth (HTM), and the Hand-to-Nape (HTN, Fig.3), executed with and without exoskeleton. Such motor tasks are paradigmatic and their combination allows a daily-life purposeful interaction with the environment. EMG activity of eight muscles and kinematics were recorded.

III. RESULTS AND DISCUSSION

Static trials indicate that LIGHTArm can provide uniform support against gravity, consistently lowering DA activity. Little residual muscular activity is addressed probably to the fact that subjects weren't able to fully relax.

In dynamic trials, EMG activity suggests that transparency features are generally achieved; the presence of the exoskeleton does not alter significantly the EMG patterns of the main agonists and antagonists muscles. The shape of the EMG spikes is generally preserved, even if sometimes amplitudes are partially altered. All subjects referred their comfort when assisted by the exoskeleton in supporting the arm weight.

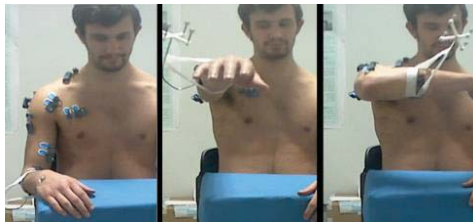


Fig. 2. Static positions. Begin (B), End (E), and Intermediate (I).

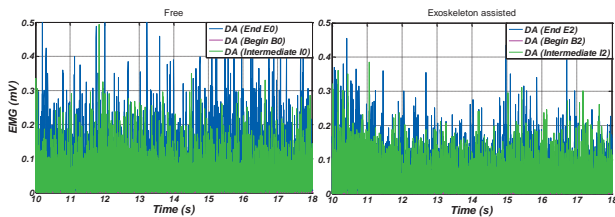


Fig 3: DA EMG activity during static trials, free and exoskeleton-assisted

TABLE I – Static and dynamic trials

Static trials IDs						
Free Positioning			Exoskeleton-assisted			
Task	Begin	Int	End	Begin	Int	End
Not Supp	B0	I0	E0	B2	I2	E2
Supp	B1	I1	E1	B3	I3	E3

Dynamic trials IDs						
Free Movement			Exoskeleton-assisted			
Task	RCH	HTM	HTN	RCH	HTM	HTN
Not Supp	R0	M0	N0	R2	M2	N2
Supp	-	-	-	R3	M3	N3

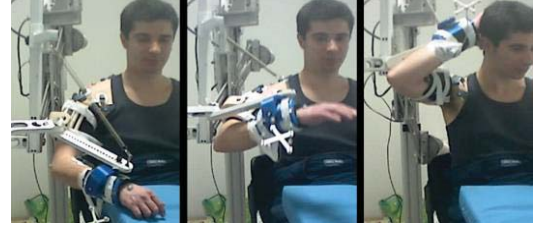


Fig. 4. The Hand-to-Nape Movement

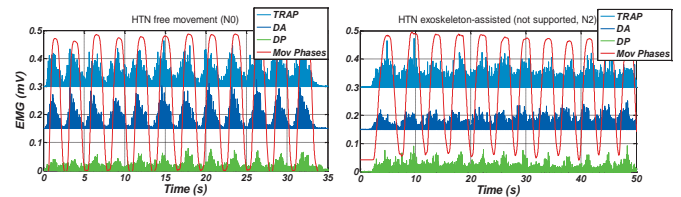


Fig. 5. The Hand-to-Nape Movement EMG patterns

IV. CONCLUSIONS

EMG analysis suggests that LIGHTArm weight-support and transparency features are satisfactory. Subjects could hold static positions with very low EMG residual activity and perform the three daily-life motor tasks in a physiological way. Future works will focus on validating these preliminary results in a larger cohort of able-bodied adults and in subjects with stroke. In addition, quantitative and statistical analyses will be performed on the EMG levels of activations and range of motions.

REFERENCES

- [1] Younan Zhang et al., "The Incidence, Prevalence, and Mortality of Stroke in France, Germany, Italy, Spain, the UK, and the US: A Literature Review", Hindawi Publishing Corporation Stroke Research and Treatment, Volume 2012, Article ID 436125
- [2] Sarah J. Housman, Kelly M. Scott, MD, and David J. Reinkensmeyer, PhD, "A Randomized Controlled Trial of Gravity-Supported, Computer-Enhanced Arm Exercise for Individuals With Severe Hemiparesis"
- [3] R. J. Sanchez et al., "Automating arm movement training following severe stroke: functional exercises with quantitative feedback in a gravity-reduced environment," Neural Systems and Rehabilitation Engineering, IEEE Transactions on, vol. 14, no. 3, pp. 378–389, 2006.
- [4] David J. Reinkensmeyer, et al., "Comparison of 3D, Assist-as-Needed Robotic Arm/Hand Movement Training Provided with Pneu-WREX to Conventional Table Top Therapy Following Chronic Stroke"
- [5] T. Nef et al., Effects of Arm Training with the Robotic Device ARMin I in Chronic Stroke: Three Single Cases, Neurodegenerative Dis, DOI: 10.1159/000262444
- [6] Morasso et al., Desirable features of a "Humanoid" Robot-Therapist. Conf Proc IEEE Eng Med Biol Soc. 2009;2009:2418-21.
- [7] M. Malosio et al., "Analysis of elbow-joints misalignment in upper-limb exoskeleton," in Rehabilitation Robotics (ICORR), 2011 IEEE International Conference on, 2011, pp. 1–6.

Kinect One-based biomechanical assessment of the upper limb during rehabilitation

A. Scano^{1,2}, M. Caimmi^{1,2}, A. Chiavenna¹, M. Malosio^{1,2}, Lorenzo Molinari Tosatti¹

¹ Inst. of Industrial Technologies and Automation, National Research Council of Italy, Via Bassini 15, Milano, Italy

² University of Brescia, Via Branze 38, Brescia, Italy

Abstract — This paper presents a Kinect One sensor-based protocol for the evaluation of the motor-performances of the upper limb of neurological patients during rehabilitative sessions. The assessment provides evaluations of kinematical, dynamical, motor and postural control variables. A pilot study was conducted on three post-stroke neurological patients, comparing Kinect-One biomechanical assessment with the outcomes of a variety of clinical scales for the evaluation of impairment and body functions of the upper limb. Results indicate coherency between the two evaluation systems, while Kinect-One assessment can provide complementary quantitative precise indications, consistently integrating the clinical scales assessment.

Keywords—Kinect One; biomechanics; upper-limb; clinical scales; rehabilitation; motor control.

I. INTRODUCTION

Stroke is a leading cause of chronic disability in Western countries [1].

In order to restore partially the lost motor functionalities, patients need to perform rehabilitative sessions to train the impaired limb and promote neuro-motor recovery. Standard methodologies are required for evaluations and monitoring of the clinical course. Motion capture systems are available in many clinics. However, because of cost, portability and time issues, the use of such sensors is not always available and their use is not suitable for home and domestic rehabilitation and evaluations.

In the last years, the Kinect sensor was released for videogame industry. Its embedded algorithms track the position of human articular centers at 30Hz frequency. Kinect applications have rapidly grown in number: in the neurological rehabilitation field, especially for stimulating the patients to move in a gaming environment [2], provide feedback to the patient [3] or train specific motor primitives [4],[5]. Previous studies investigated the difference between Kinect and marker-based systems on the evaluations used in clinical environment to assess the performances of patients' upper-limbs [6],[7], showing that, despite losing sensibility, the Kinect can provide useful evaluations clustering healthy subjects and patients depending on the level of their *impairment* and evaluating their *activity* level on reaching against gravity motor tasks. Recently, the Kinect-One sensor was released. It features a more precise and accurate tracking, thanks to improved joint recognition algorithms and a more accurate sensor. Kinect-One is available for the very low price of about 200\$, and can be easily connected to a PC at

home.

A protocol for biomechanical evaluations already in use in robotic rehabilitation, conceived for assessing some of the characteristics of the *neuromusculoskeletal and movement related functions and structures related to movement and mobility* of the International Classification of Functioning, was tested on the Kinect sensor for acquisitions on healthy subjects and patients [6], [7]. In this study, such protocol was adapted to the Kinect-One sensor, used to evaluate patients' performances, and proposed for comparison and integration with specific clinical scales assessment.

II. MATERIALS AND METHODS

A. Aim of the work

The aim of the work is to compare the assessments of the upper-limb motor performances of neurological patients with the Kinect and Kinect-One sensors and a marker-based commercial motion capture system, during the execution of functional movements (reaching against gravity, RCH, Fig.3).

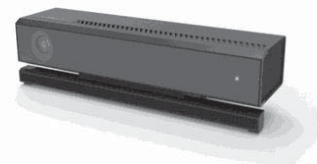


Fig. 1. The Kinect One sensor

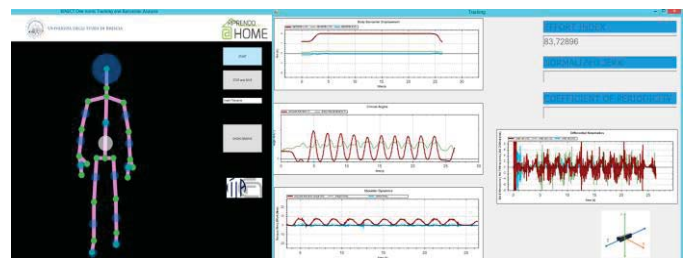


Fig. 2. The Kinect-One application

B. Materials

The following equipment was used:

- Microsoft Kinect-One with SDK 2.0 and C# software and Microsoft Kinect (Python software) developed at ITIA CNR
- a 6-TVC Marker-based Motion Capture system (Smart-D, B|T|S, Italy).
- Matlab 2013a for off-line data analysis

The study took place in the ITIA Robotic Laboratory, at the Villa Beretta Rehabilitation Center, Costa Masnaga, Lecco, Italy.

C. Evaluation protocol

The evaluation protocol is based on the following measures:

Kinematics:

- Shoulder elevation angle;
- Elbow flexo-extension angle;

Both measured at maximum arm elevation, they provide indications about the range of motion.

Dynamics:

- Shoulder elevation torque (measured at maximum elevation);
- Effort index of the shoulder (provides assessment on the effort exerted to support the limb during the motor task);

Motor Control:

- Normalized Jerk (associated to the smoothness of the motion of the wrist; it is a typical parameter related to motor control and correct movement execution);
- Coefficient of Periodicity (evaluates the repeatability of the motion law);

Postural Control:

- Displacement of center of mass of the body;
- Displacements of the center of mass of the segments;

Such evaluations are part of a clinical protocol currently in use for the evaluation of free and robotic-assisted movements on RCH and hand-to-mouth motor tasks, and previously used in Kinect studies [5], [6].

III. RESULTS AND DISCUSSION



Fig. 3. A patient performing a reaching against gravity movement

For brevity, only Normalized Jerk results, correlated to the smoothness of the movement, are shown in comparison to the BTS system, used as reference. Subjects 1-5 and Patients 1-2 were tested with the Kinect, while Patients 3-5 were tested with the Kinect One. Healthy subjects executed smooth, low-jerk movements. Patient 1 and 3 showed good residual motor control and perform quite-physiological movements. Results indicate that, despite losing some sensibility, patients and healthy subjects are clustered correctly with Kinect sensors. The same conclusions are valid for the other parameters of the biomechanical assessment.

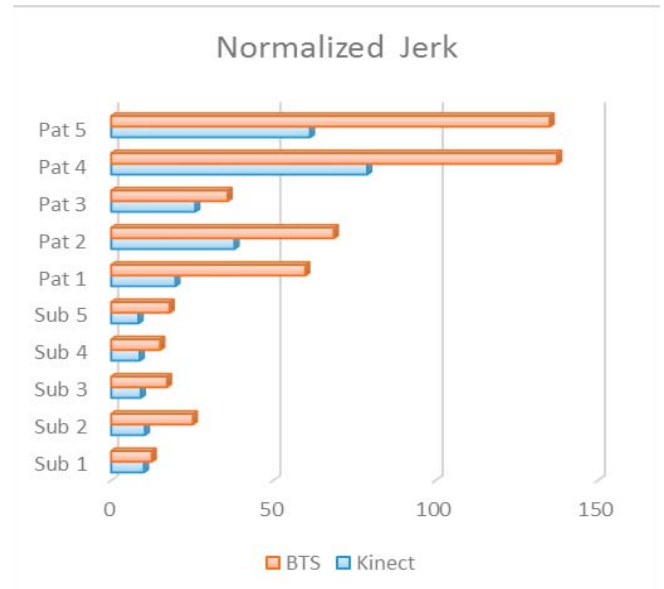


Fig. 4. Mean Normalized Jerk for Healthy Subjects and Patients. Sub 1-5 and Pat 1-2 with Kinect, Pat 3-5 with the Kinect One, compared to BTS.

IV. CONCLUSIONS

A Kinect-One based software for the biomechanical evaluation of the upper limb was presented. It features an online evaluation of the performances of the upper-limb during the execution of reaching against gravity movements. Preliminary results on healthy subjects and neurological patients indicate that Kinect is capable of fine evaluations that can discriminate among different degrees of impairment.

ACKNOWLEDGEMENT

This work was partially supported by the Italian Lombardy region within the RIPRENDO@home project.

REFERENCES

- [1] M. Mill'an and A. D'avalos, "The need for new therapies for acute ischaemic stroke," *Cerebrovasc Dis*, vol. 22(suppl 1), pp. 3–9, 2006.
 - [2] Michele Pirovano, Renato Mainetti, Gabriel Baud-Bovy, Pier Luca Lanzi, Nunzio Alberto Borghese, Self-Adaptive Games for Rehabilitation at Home, 2012 IEEE Conference on Computational Intelligence and Games (CIG'12)
 - [3] Stefano Mottura, Sara Arlati, Luca Fontana, Marco Sacco, "Enhancing awareness and personification by virtual reality and multimedia means in post-stroke patients during rehabilitation", *CogInfoCom 2014 • 5th IEEE International Conference on Cognitive Infocommunications • November 5-7, 2014, Vietri sul Mare, Italy*
 - [4] Y. J. Chang, W. Y. Han, and Y. C. Tsai, "A Kinect-based upper limb rehabilitation system to assist people with cerebral palsy," *Res Dev Disabil*, vol. 34, pp. 3654–3659, Nov 2013.
 - [5] Y. J. Chang, S. F. Chen, and J. D. Huang, "A Kinect-based system for physical rehabilitation: a pilot study for young adults with motor disabilities," *Res Dev Disabil*, vol. 32, no. 6, pp. 2566–2570, 2011.
 - [6] A.Scano, M.Caimmi, M.Malosio, L.Molinari Tosatti, "Using Kinect for upper-limb functional evaluation in home rehabilitation: A comparison with a 3D stereoscopic passive marker system", *Biomedical Robotics and Biomechatronics (2014 5th IEEE RAS & EMBS International Conference on)*, Sao Paulo (Brasil), 12-15 Aug. 2014, Page(s):561 - 566
- A.Scano, M.Caimmi, M.Malosio, L.Molinari Tosatti, "Motor control indexes in rehabilitation: effect of the sampling frequency", *XIV Siamoc-Esmac Conference, Rome (Italy)*, 30 sept.-4oct. 2014

Static mechanical characterization of cements for dental implantology through nanoindentation

G.Serino¹, M.Terzini¹, and A.L. Audenino¹

¹ Department of Mechanical and Aerospace Engineering – Politecnico di Torino, ITALY

Abstract — The nanoindentation technique has become very popular in the field of mechanical testing of materials for biomedical applications, due to the punctuality of the test, the reduced quantity of material required and the possibility of testing soft materials. This technique has been used in this work with the purpose of identifying the mechanical properties of cements for dental implantology. Three cements were characterized. For all the samples the same input curve was applied. The experimental plan considered three factors: the cement type, the loading rate and the indentation depth. On samples, the Young's Modulus and Hardness were calculated by applying the Oliver and Pharr Method. The mechanical properties were subsequently compared through multivariate analysis of variance (ANOVA). Results confirmed the higher mechanical properties of permanent cements compared with temporary ones, also highlighting a viscous-plastic behavior for all the cements analyzed.

Keywords—indentation, cements, implantology, mechanical-properties

I. INTRODUCTION

Nowadays dental implants have become a valid substitute of natural teeth thanks to their functionality and aesthetics [1]. Dental prosthesis can be fixed on the dental implant screwing the crown on the abutment (screw-retained), or alternatively by means of special cements (cement-retained). These same cements are also used as luting agents in fixing the crowns on natural teeth. The retrievability of the crown is actually challenging in implant dentistry, where using temporary or permanent cements ensure different degrees of crown retrievability [2]. In this scenario, providing a characterization of the mechanical properties of cements for dental applications is mandatory. Even if several studies have been performed to identify the failure load of dental implants, a systematic, reliable characterization of the mechanical behavior of cements for dental applications is still lacking. In this work we apply nanoindentation technique in order to systematically characterize the mechanical response of both temporary and permanent cements.

II. MATERIALS AND METHOD

Here three different commercial cements were tested, i.e., the temporary cements Temp Bond (composed by Zinc Oxide) and Telio C.S (composed by Bis Metacrilati and Fillers) and the permanent cement Harvard (composed by Zinc Oxide, Magnesium Oxide and Phosphoric Acid).

Cement samples were embedded into epoxy resin, cut and polished.

All tests were performed with a Nanoindenter XP (MTS/Agilent, USA), equipped with a diamond Berkovich indenter. As a first step, a standard calibration procedure was performed on a silica sample, so as to determine the proper *area function*. In order to properly identify an adequate site for indentation, a microscope-to-indenter calibration was also performed.

Here an input curve made of a loading step and a successive unloading step characterized by the same slope was adopted. An intermediate holding step was maintained for 30 seconds.

All the cements underwent experiments where two values of *Indentation Depth*, and four values of *Loading Rate* were applied, as summarized in Table I.

TABLE I

<i>Loading Rate</i> (mN/s)	<i>Samples</i>	<i>Indentation Depth (nm)</i>
0.05	Temp Bond Telio C.S. Harvard	1000
0.1		
0.25		2000
0.5		

For each sample twenty indentations were performed, exploring the overall sample surface by varying the values of the experimental factors.

The curves recorded by nanoindentation were elaborated with the Oliver and Pharr method [3], which allowed us to estimate the elastic (Young's Modulus) and plastic properties (Hardness) of the samples.

A. Statistical analysis

An analysis of variance (ANOVA) was performed to analyze the influence of the experimental setting on cements' mechanical properties. Preliminarily, results for all cement types, indentation depths and loading rates were considered, pursuing two different analysis considering the elastic and plastic properties separately. A further analysis of variance was performed considering separately the temporary and the permanent cements.

III. RESULTS AND DISCUSION

The findings from the experimental tests show high repeatability, thus confirming nanoindentation as an

appropriate method when cements for dental implantology have to be mechanically characterized.

Load-displacement resulting curves (Fig. 1), as expected, exhibited a trend resembling the input curve. As for the hold and the unload phases, different behavior were observed, depending on the properties of the cements: temporary cements showed an holding segment longer than the permanent one. Curves of permanent cements also presented a slope more marked than the temporary cement, in the unloading segment.

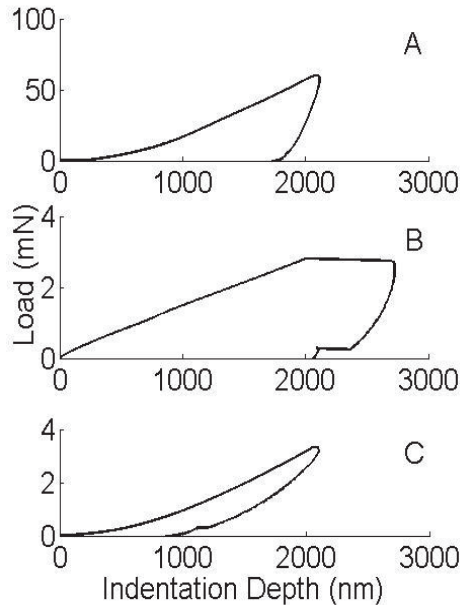


Fig.1 Load-Displacement curve obtained for: A-Harvard sample, B-Temp Bond sample, C-Telio C.S. sample

The obtained results, summarized in Table II and Table III, highlight that the permanent cement is characterized by higher hardness and Young modulus when compared with temporary cements, in agreement with the results found in literature [4], [5], [6].

TABLE II
YOUNG'S MODULUS (GPa)

Loading Rate (mN/s)	Indentation Depth							
	1000 nm				2000 nm			
	0.05	0.1	0.25	0.5	0.05	0.1	0.25	0.5
Harvard	32,89	29,3	26,28	25,8	36,86	34,56	33,64	23,06
Temp Bond	1,07	0,9	0,94	1,39	1,16	1,22	0,93	0,79
Telio C.S.	0,37	0,41	0,44	0,5	0,48	0,38	0,41	0,37

TABLE III
HARDNESS (GPa)

Loading Rate (mN/s)	Indentation Depth							
	1000 nm				2000 nm			
	0.05	0.1	0.25	0.5	0.05	0.1	0.25	0.5
Harvard	0,81	0,68	0,59	0,74	0,58	0,6	0,66	0,52
Temp Bond	0,02	0,02	0,02	0,04	0,01	0,01	0,01	0,01
Telio C.S.	0,02	0,03	0,03	0,02	0,03	0,03	0,03	0,02

Interestingly, the Young's modulus appeared to be related to the loading rate, suggesting that the elastic properties of these cements are loading rate dependent. Conversely, no clear evidence of dependence of the plastic properties from the loading rate was observed, at this stage of investigation.

The statistical analysis confirmed the correlation between loading rate and indentation depth with the Young's Modulus parameter ($p < 0.05$). Hardness, on the contrary, was found to be dependent only on the indentation depth, presumably due to different concentrations of components at different depths.

IV. CONCLUSION

This work showed that a dependence of the mechanical behavior of cements for dental application on the *loading rate* there exists, also highlighting that, in addition to the elasto-plastic properties of these materials, also a viscous behaviour is present. The Oliver and Pharr method used for the analysis of the experimental data turned out to be the proper method for the quantification of the mechanical properties of these cements.

As a possible limitation of the study, it should be noted that all the experiments were performed on dry specimens, which is not their operating condition, being these cements used in a wet environment, i.e., the oral cavity. Other tests will be performed on wet specimens.

IV. REFERENCES

- [1] JE Dudley, LC Richards, JR Abbott. Retention of cast crown copings cemented to implant abutments. *Australian Dental Journal*. 2008, Vol. 53, p. 332-339.
- [2] "Dental implants and improvement of oral health-related of life". K. Pavel, M. Seydlova, T. Dostalova, V. Zdenek, K. Chleborad, Z. February 2012, *Community Dent Oral Epidemiol*, Vol. 40, p. 66-71.
- [3] W.C. Oliver, G.M. Pharr. An improved technique for determining hardness and elastic modulus using load and displacement sensing indentation experiments. *J. Mater. Reserch*. June 1992, Vol. 7, 6.
- [4] Breeding LC, Dixon DL, Bogacki MT, Tietge JD. Use of luting agents with an implant system: Part 1. *J. Prosthet Dent*. 1992.
- [5] Yongsik Kim, Yamashita, Jeffrey L. Shotwell, Kok-Heng Chong and Hom-Lay Wang. The comparison of provisional luting agents and abutment surface roughness on the retention of provisional implant-supported crowns. *the Journal of Prosthetic Dentistry*. 2006, Vol. 95, 6.
- [6] The effects of height and surface roughness of abutments and the type of cement on bond strength of cement-retained implant restorations. Khaled Q. Al Hamad, Bashar A. Al Rashdan, Ethar H. Abu-Sitta. 2010.

LIGHTarm: a gravity-compensated exoskeleton for the upper-limb rehabilitation

G. Spagnuolo^{1,2}, M. Malosio^{1,2}, J.C. Dalberto¹, A. Scano^{1,2},
A. Chiavenna¹, M. Caimmi^{1,2}, G. Legnani², L. Molinari Tosatti¹

¹ *Inst. of Industrial Technologies and Automation, National Research Council of Italy, Via Bassini 15, Milano, Italy*

² *University of Brescia, Via Branze 38, Brescia, Italy*

Abstract— This paper presents LIGHTarm, a highly ergonomic gravity-compensated exoskeleton for the upper-limb neurorehabilitation, characterized by a peculiar kinematic structure, expressly conceived to face shoulder rhythm and elbow singularity issues, achieving high backdrivability throughout a large exploitable range of motion. The designed gravity compensation mechanism guarantees a good limb support for impaired people, facilitating upper-limb spatial movements in rehabilitation therapies.

Keywords— Upper-limb rehabilitation, Gravity-compensated exoskeleton, Shoulder rhythm, Elbow singularity.

I. INTRODUCTION

SUPPORT against gravity is a promising strategy to enable upper extremity rehabilitation in neurological patients. Raising the upper-limb against gravity is one of the hardest tasks for neurological patients, since neurological diseases affect the capability of performing the majority of functional movements and interacting with the environment [1]. The effectiveness of weight-support approaches was observed in exoskeleton-assisted studies that showed benefits in terms of motor function recovery [2] and reduction of the influence of abnormal coupling (flexural-synergies) between shoulder and elbow. Technology that allows patients to perform therapy without robotic actuation may also be effective in improving recovery [3]. In contrast to actuated devices, unactuated and gravity-compensated orthoses are potentially less costly, safer and appropriate for semiautonomous training at home. Starting from a peculiar and patent-pending kinematic architecture [4], a highly ergonomic and passively gravity-compensated exoskeleton for the upper limb neuro-rehabilitation, namely *LIGHTarm*, is being developed. Its peculiar kinematic structure a) enables the human shoulder to move complying with the physiological shoulder rhythm and b) avoids the occurrence of any singularity in the whole elbow range of motion [4]. These features are promising for guaranteeing high transparency, allowing the exoskeleton to follow accurately arm's movement in a large exploitable range of motion.

II. PASSIVELY GRAVITY-BALANCED EXOSKELETON

An articulated mechanism is said to be *gravity-balanced* if it is in indifferent equilibrium without requiring joint actuator forces or torques [5]. Physically, this means that the total potential energy of the device is invariant whatever its configuration is. This condition can be realized in different ways, using counter masses, springs and/or auxiliary parallelograms [6]. The gravity-balancing system is made up of a combination of these three mechanical elements, in order

to partially decouple the gravitational load contributions of the upper-arm and the forearm segments. A schematic representation of the exoskeleton is depicted in Fig 2.a. The gravity-balancing contribution has been partially decoupled between a counterweight W_s , in charge of supporting the arm and exoskeleton masses, and a spring s in charge of supporting the elbow mass. No torque is transferred from the human upper limb and the exoskeleton, through the interface cuffs because of the presence of the spherical joints. For convenience, referring to Fig 2.b-2.c, let us denote by:

- $\mathbf{Q}_{\{t\}}$ the vector connecting the origin O_i of frame $\{t\}$ to point Q ;
- $\mathbf{Q}_{\{t\},i}$ the component of vector $\mathbf{Q}_{\{t\}}$ along the direction i (i.e. x,y,z) of frame $\{t\}$;
- \mathbf{G}_a and m_a the center of mass and the value of the mass of a , respectively;
- \mathbf{G}_f and m_f the center of mass and the value of the mass of f , respectively.

A. Auxiliary Parallelogram Counter-Balance Mechanism

The overall mass of the exoskeleton and of the upper limb is counterbalanced by a mass W_s , rigidly connected to an auxiliary-parallelogram mechanism (Fig 2.a-2.b): referring to the plane of elevation (π_a), the planar hinged-parallelogram produces 1-DoF circular translation [7]. It consents to the reference frame $\{ee\}$ centered in the elbow to translate w.r.t. the shoulder reference frame $\{es\}$, as represented in Fig 2.b. This leads the point A to be above O_{ee} , having the line $\overline{OA}/e_{es,x}$ for any configuration, guaranteeing that the forces generated by the spring s supporting the forearm is unaffected by the upper-arm.

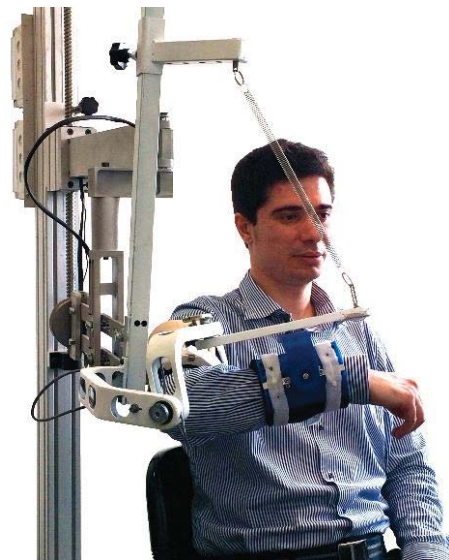


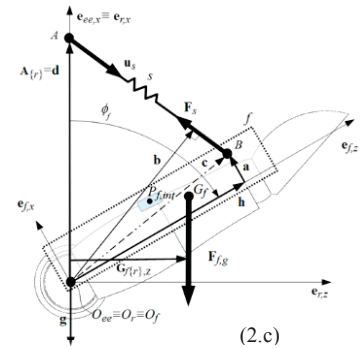
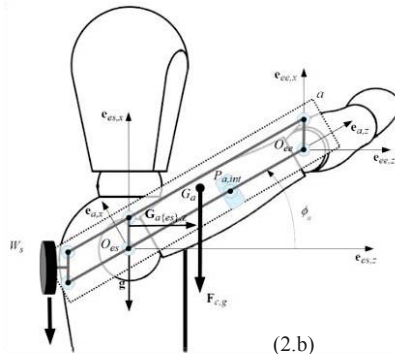
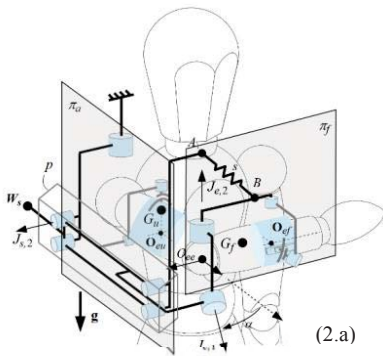
Fig. 1. First prototype of *LIGHTarm*.

Fig. 2. Kinematic scheme of the gravity-balanced version of *LIGHTarm*. (1.a) The counterbalance W_s supports the whole arm mass about the shoulder joint $J_{s,2}$, spring s supports the forearm mass about Cardan joint $S_e = \{J_{e,1}, J_{e,2}\}$ nearby the elbow. (1.b) Counterbalance-based mechanism supporting the upper limb. (1.c) Spring-based mechanism supporting the forearm.

Referring to Fig 2.b, let us consider the fixed reference frame $\{es\}$ w.r.t. which the body a rotates, and a reference frame $\{a\}$ rigidly connected to a . The counterweight W_s has to counterbalance all the arm and forearm masses. The auxiliary parallelogram allows the mass balance in respect to O_{es} to be not influenced by the actual configuration of the masses downline the parallelogram. Thus, the counterbalance system is independent from the forearm orientation.

$$\tau_{a,g} = \mathbf{G}_{a\{es\},z} \times \mathbf{F}_{ea,g} + \mathbf{P}_{a,int\{es\},z} \times \mathbf{F}_{ha,g} + \mathbf{O}_{ee\{es\},z} \times \mathbf{F}_{f,g}$$

denoting by $\mathbf{F}_{ea,g}$, $\mathbf{F}_{ha,g}$, $\mathbf{F}_{f,g}$ the gravity forces of the exoskeleton and human upper-arm, and the whole forearm contribution, $\mathbf{G}_{a\{es\},z}$, $\mathbf{P}_{a,int\{es\},z}$, $\mathbf{O}_{ee\{es\},z}$ their respective distance from O_{es} . The torque arm of the masses downline the parallelogram is constantly equal to $\mathbf{O}_{ee\{es\},z}$.

B. Forearm Spring-Balancing Mechanism

The forearm mass is antigravitary suspended by tension spring, generating a tension force between point A of the exoskeleton structure and point B along the forearm (Fig 2.a). Let us refer to the model depicted in (Fig 2.c), schematizing the spring balancing system, supporting a body f , modeling the forearm, hinged to a point O_f . Referring to (Fig 1.a), it is a representation of the forearm kinematics on the plane π_r . Let us consider a fixed reference frame $\{r\}$ w.r.t. which the body f rotates, and a reference frame $\{f\}$ rigidly connected to f . A tension spring s is connected between points A and B , respectively fixed w.r.t. $\{r\}$ and $\{f\}$. According to the conventions introduced in the previous paragraph, the total torque applied to f is $\tau_{f,t} = \tau_s + \tau_{f,g}$, where:

- $\tau_s = \mathbf{b} \times \mathbf{F}_s$,
- $\tau_{f,g} = \mathbf{G}_{f\{r\},z} \times \mathbf{F}_{ef,g} + \mathbf{P}_{f,int\{r\},z} \times \mathbf{F}_{hf,g}$,

denoting by \mathbf{F}_s the force exerted by the spring, $\mathbf{F}_{ef,g}$, $\mathbf{F}_{hf,g}$ the gravity forces of the exoskeleton and human forearm, \mathbf{b} , $\mathbf{G}_{f\{r\},z}$, $\mathbf{P}_{f,int\{r\},z}$ their respective distance from O_{ee} . The body f is

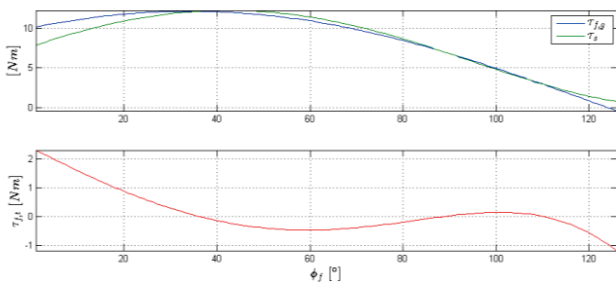


Fig. 3. Numerical optimization of the spring-balancing mechanism (Male subject, age 29, height 179 cm, weight 78 kg. The inertial parameters have been deduced from anthropometric data reported in [9]).

in static equilibrium if $\|\tau_{f,t}\| = 0$. Finally, let ϕ_f be the angle

defined as: $\phi_f \triangleq \angle(e_{ee,x}, e_{f,z})$. The presented model has been applied to optimize the spring balancing mechanism and to identify the commercial springs to be employed in the prototype [8]. A numerical routine has been implemented to optimize the mechanical spring parameters (k , l_0) and the geometry of the spring support system (d , h) in order to minimize the cost function $\max(\|\tau_{f,t}\|)$ varying ϕ_f in the elbow range of motion (e.g. depicted in Fig. 3).

III. CONCLUSION

LIGHTarm is a passive gravity-compensated exoskeleton for upper-limb rehabilitation. Specific benefits derive from its peculiar kinematic structure. It is currently being tested in preliminary clinical trials by healthy subjects. The first prototype will be presented during the V Meeting ESB-ITA.

ACKNOWLEDGEMENT

This work was partially supported by the Italian Lombardy region within the RIPRENDO@home project.

REFERENCES

- [1] Krabben T., Prange G. B., et al., "Influence of gravity compensation training on synergistic movement patterns of the upper extremity after stroke, a pilot study," *Neuroeng Rehabil.* 2012; 9: 44.
- [2] David J. Reinkensmeyer, Eric T. Wolbrecht, et al., "Comparison of 3D, Assist-as-Needed Robotic Arm/Hand Movement Training Provided with Pneu-WREX to Conventional Table Top Therapy Following Chronic Stroke," *Am J Phys Med Rehabil.* 2012 Nov; 91(11 0 3): S232-S241.
- [3] Kahn, L. E., Lum, et al. (2006). Robot-assisted movement training for the stroke-impaired arm: Does it matter what the robot does?. *Journal of rehabilitation research and development*, 43(5), 619.
- [4] Malosio, M.; Pedrocchi, N.; Vicentini, F.; Tosatti, L.M., "Analysis of elbow-joints misalignment in upper-limb exoskeleton," *Rehabilitation Robotics (ICORR), 2011 IEEE International Conference on*, vol., no., pp.1,6, June 29 2011-July 1 2011
- [5] Rahman, T., Ramanathan, R., Seliktar, R., & Harwin, W. (1995). A simple technique to passively gravity-balance articulated mechanisms. *Journal of Mechanical Design*, 117(4), 655-658.
- [6] Herder, J. L. (2001). *Energy-free Systems. Theory, conception and design of statically*.
- [7] Lee, C. C., & Hervé, J. M. (2014). Geometric Derivation of 6R Linkages with Circular Translation. In *Advances in Robot Kinematics* (pp. 59-67). Springer International Publishing.
- [8] G. Spagnuolo, M. Malosio, J. C. Dalberto, M. Caimmi, e L. Molinari Tosatti, "LIGHTarm: A highly adaptable gravity-compensated exoskeleton for upper-limb rehabilitation and ADL assistance", *1st Clinical Movement Analysis World Conference*, 29 September – 4 October 2014, Rome, Italy.

- [9] Winter, D. A. (2009). *Biomechanics and motor control of human movement*. John Wiley & Sons.

Design with finite element method (FEM) of a modular small dimensions force platform for gait analysis

P. Tamburini¹, R. Stagni^{1,2}, and A. Cappello¹

¹ Department of Electrical, Electronic and Information Engineering "Guglielmo Marconi", University of Bologna, Italy

² Health Sciences and Technologies, Interdepartmental Center for Industrial Research (HST-ICIR), Ozzano dell'Emilia, Italy

Abstract— The gait analysis of subjects with short and non-uniform gait is difficult using the common commercial force platforms. The present work consists in the design, based on finite element method (FEM) analysis, of a force platform of small dimensions (0.40x0.40 m) considering static and dynamic simulation of its behaviour. The aim of this project is to improve, with a simple and low cost structure, the instrumentation available for the gait analysis of children and neurologic patients. The applicability of gait analysis to children and neurologic patients, improved the flexibility of force platforms without losing the performance provided by traditional force platforms (e.g. for postural analysis)

Keywords—gait analysis, force plate, dynamometry, FEM analysis

I. INTRODUCTION

GAIT analysis of subjects with short and non-uniform gait, typical children, children with cerebral palsy, elderly and stroke patients, can result critical in terms of ground reaction force (GRF) quantification with traditional force platforms. The standard *de facto* of commercial force platforms dimension (0.60x0.40 m) can determine problems resulting from the double contact of the foot on the same platform that does not allow the identification of the GRF under each foot. The current proposal of the companies is the use of standard force platforms arranged so as to achieve a sensitive corridor. This solution allows the acquisition of several steps, but maintaining the size of the force platform does not solve the problem of double contact.

The aim of this work is the design, by finite element method (FEM), of a small modular force platform (0.40x0.40 m) to solve the problem of double contact, maintaining the reference performance of commercial larger platforms. The small dimensions require the use of large number of platforms in order to instrument a corridor. However, the simplicity of the design and materials used allows the use of multiple force platforms at low cost. Electronics dedicated to the acquisition of the output signal is not required because a commercial evaluation board can be exploited, that is able to independently manage the output of the strain gauges. This solution simplifies the realization of instrumented corridors.

II. MATERIALS & METHODS

The design of the proposed small modular force platform [1] was performed aiming to obtaining a performance comparable to that of commercial force platforms.

For modularity purpose and to allow the differentiate short steps, the total dimension of the force platform is: 0.40x0.40x0.105 m. The force platform was composed of: *i*) 1 aluminium top 0.40x0.40x0.02 m *ii*) 4 aluminium hollow cylindrical posts with inner radius 0.013 m and outer radius 0.011 m and height 0.07 m *iii*) 1 steel base 0.40x0.40x0.015 m. The minimum number of mono-axial strain gauges is used for deformation sensing: six for each post, longitudinally arranged. The total number of strain gauges used is twenty-four per platform. The output of each strain gauge is directly provided as input to a commercial evaluation board (e.g. Texas Instruments DDC264 DDC1128). This removes the need for ad hoc electronics for signal acquisition. In addition, the commercial evaluation board manages current signals, solving the problem of signal attenuation introduced by the cable length that is present when using voltage signals.

COMSOL Multiphysics was used for implementing the FEM. Static analysis was performed to estimate the platform calibration matrix based on least square fitting. A uniformly distributed load was applied to a surface of radius $R_{Area} = 0.05$ m and 576 simulations were implemented considering applied forces varying between -200 N and 200 N for F_x and F_y and between -2000 N and -200 N for F_z , in 9 different points of application. The coordinates (x_{cop} , y_{cop}) of centre of pressure (COP) of distributed load were all possible combination of $x_{cop} = [0.05, 0.20, 0.35]$ m, and $y_{cop} = [0.05, 0.20, 0.35]$ m; which were used in order to cover most of the surface of the platform. The large number of testing conditions used for the estimation of the calibration matrix was chosen in order to cover the largest number of possible operative conditions.

Eighty-four additional simulations were performed to test the calibration matrix and quantify the error that the system commits in the estimation of applied loads and moments. For these testing simulations, loads and corresponding application points were chosen in order to test the calibration matrix with settings not exploited in the estimation of the

calibration matrix.

Dynamic analysis was implemented with the default COMSOL eigenfrequencies solver, allowing the estimation of the resonance frequency of the force platform.

III. RESULTS

The median error made in the determination of the forces is between -0.0378% and 0.0041%. The maximum error made in the determination of the forces ranges from a minimum of 0.0325% to a maximum of 0.8075 %. These results are valid regardless of the value of the applied load. The median error made in the determination of the moments is between 0.0028 % and 0.0372 %. The maximum error made in the determination of the moments is in M_x 0.1112 % at -45 Nm, in M_y 0.2401 % at 15 Nm and in M_z 3.435 % at 10 Nm. Choosing a reference value exciding 20 Nm, the maximum error committed in the determination of M_x does not change. For M_y is 0.1540 % and for M_z is 0.6090 %. The median and the maximum error in the determination of the forces and moments, based on the calculated calibration matrix, resulting from the 84 additional simulations are illustrated in Tables 1 and 2.

The resonance frequency resulting from the dynamic analysis was 350 Hz.

TABLE I

<i>Component of the Force</i>	<i>Median Error %</i>	<i>Maximum Error %</i>
F_x	-0.0378	0.8075
F_y	-0.0022	0.2137
F_z	0.0041	0.0325

Table 1 Median and Maximum error in the determination of the Forces.

TABLE II

<i>Component of the Moment</i>	<i>Median Error %</i>	<i>Maximum Error % Reference Value (Nm)</i>
M_x	0.0070	0.112 - 45
M_y	0.0028	0.2401 15
M_z	0.0372	3.435 10

Table 2 Median and Maximum error in the determination of the Moments.

IV. CONCLUSION

The range of the forces used, and the resonance frequency are comparable to those of commercial platforms [2].

In order to obtain a proper functioning of the device, once built, it will be necessary to calibrate *in situ*. This will help to compensate for the error introduced by non-alignment in the positioning of the strain gauges, mechanical crosstalk and more [3 4]. The low cost of mechanical structure and the use of commercial evaluation board encourages the creation of multiple platforms. An *ad hoc* support base is provided in such a way as to allow the isolation of the structure and then

a proper measure. In addition, the support base allows solving many of the critical issues related to the installation.

The starter kit, which consists of two platforms, allows the standard balance analysis achieved with commercial platforms. Furthermore it allows us to distinguish the GRF of each foot and through integration techniques we are able to estimate a global GRF

REFERENCES

- [1] H-B Schmiedmayer, J Kastner, Parameters influencing the accuracy of the point of force application determined with piezoelectric force plates, *JBIOMECH* 32:1237-1242, 1999.
- [2] www.berotec.com.
- [3] Cedrarò, A. Cappello, L. Chiari, A portable system for in-situ re-calibration of force platforms: experimental validation, *GAIT&POSTURE*, 29(3):449-453, 2009.
- [4] Cappello A, Bagalà F, Cedrarò A, Chiari L, Non-linear re-calibration of force platforms GAIT&POSTURE 33(4):724-726, 2011.networks," *IEEE Trans. Neural Networks*, vol. 4, pp. 570-578, July 1993.

Fall risk monitoring: from laboratory to a portable device, influence of sampling frequency

P. Tamburini¹, R. Stagni^{1,2}

¹ Department of Electric, Electronic and Information Engineering "Guglielmo Marconi"—DEI University of Bologna Italy

² Health Sciences and Technologies—Interdepartmental Center for Industrial Research (HST-ICIR), University of Bologna, Italy

Abstract— The understanding of locomotor stability is a critical issue in the assessment of subjects with high level of fall risk either pathological (e.g. stroke subjects) or elderly. Clinical assessment of fall risk is typically based on clinical rating scales; however, this approach heavily relies on the clinician's subjective judgment. Instrumental stability and variability indexes of gait can represent a promising solution for the objective quantification of locomotor function and fall risk. Furthermore clusters of stability and variability indexes give important information about the clinical deficits of subjects that could be the causes of the fall risk.

An important step for the improvement of the assessment of fall risk is to analyze the subject's walk not only in the laboratory but also in his daily life. This is possible with the implementation of the stability and variability indexes in a portable device. Mobile phone is the ideal device for this goal. Indeed it is user friendly, cheap and although the IMUs mounted on standard smart phones have nothing to envy to other commercially available devices, but sampling frequency at 100 or 200 Hz is not compatible with the computational characteristics. The influence of reduced sampling frequency on the assessment of variability and stability indexes used for the monitoring must be assessed, and this is the aim of the present work.

Keywords— fall risk, fall risk assessment, fall risk monitoring, stability and variability indexes.

I. INTRODUCTION

FALLS represent a major community and public health problem, with large clinical and economic consequences.

The understanding of locomotor stability is a critical issue in clinical assessment procedures. Clinicians use clinical rating scales for fall risk assessment; but this approach highly relies on the clinician's subjective judgment [1]. Several variability and stability measures were proposed in the literature for the subject specific assessment of fall risk. Although promising, the assessment of fall risk without any indication of the subject specific factors leading to it, can not provide indication for the design of any effective clinical intervention for its effective reduction. Recent work [2,3] demonstrated that clustering appropriate selected indexes can provide indication regarding the specific subject alterations increasing fall risk. The effective exploitation of this approach is meant in its implementation on a portable device for the continuous monitoring of subjects at risk, either pathological (e.g. stroke subjects) or elderly subjects. The ideal device to maximise the exploitation, and subject acceptance is a mobile phone. Although the IMUs mounted on standard smart phones have nothing to envy to other commercially available devices, but sampling frequency at 100 or 200 Hz is not compatible with the computational characteristics. The influence of reduced sampling frequency

on the assessment of variability and stability indexes used for the monitoring must be assessed, and this is the aim of the present work. This is an essential step for bringing the method from the laboratory to real practice without loosing the performance.

II. MATERIALS & METHODS

A. Participants

Ten healthy young subjects, 7 males and 3 females (28 ± 3 years, 174 ± 11 cm, 67 ± 13 kg), participated to the study. All the subjects were recruited from the students /volunteers at the University of Bologna.

B. Test procedure and measurement equipment

The subjects performed a walking along a straight line at self selected speed on 250 m long dead-end road wearing 2 tri-axial accelerometers (Opal, APDM, USA), one located at the level of the fifth lumbar vertebra and one on the right ankle.

Acceleration and angular velocity in vertical (V), medio-lateral (ML) and antero-posterior (AP) were acquired with sample frequency of 128 Hz.

C. Gait stability and variability indexes

Eleven gait variability and stability indexes were calculated on trunk acceleration signal during gait obtained from the walking trial. Such indexes were Standard Deviation (SD), Coefficient of Variation (CV), Nonstationary index (NI), Inconsistency of Variance (IV), Poincaré Plots (PSD1/PSD2), Maximum Floquet Multipliers (maxFM), short-term Lyapunov exponents (sLE), long-term Lyapunov exponents (lLE), Harmonic Ratio (HR) [8], which gives an indication of the smoothness of the acceleration pattern, Index of Harmonicity (IH) [9], Multiscale Entropy (MSE) [10], which is an indicator of complexity of the signal at several scales, and Recurrence Quantification Analysis (RQA) [11]. The two latter indexes produce 6 and 5 sub-measures respectively, based on the time scale in MSE or based on the feature of the recurrence plot that are analyzed in RQA, namely recurrence rate (rr), determinism (det), average length of diagonal lines (avg), maximum length of diagonal lines (max), divergence (div).

D. Data analysis

Stability and variability indexes were calculated on acceleration data from the whole duration of the walking trial. Each indexes was calculated for the acquired signal (at 128 Hz) and for other two signals obtained from the original one by under-sampling at 64 and 32 Hz and also for anterior-posterior (AP), medio-lateral (ML) and vertical (V)

acceleration directions. Right heel strike instants were obtained from the angular velocity, around the antero-posterior axis, measured by the sensor on the ankle with wavelet analysis based method [13] and stride time was calculated accordingly. The first and last three strides were removed in order to exclude gait initiation-termination phase. The obtained indexes were testing with gaussianity test (Kolmogorov-Smirnov test) in such way was possible performed the right statistical analysis: ANOVA test with a p-value of 5%. Last step of the statistical analysis was the implementation of a multiple comparison analysis using a Tukey-Kramer test. The statistical analysis compares the obtained indexes by original signal (the reference) with the indexes obtained by under-sampling from the original one.

Data analysis and statistical analysis were performed with MatLab (Math Works, NATICK, USA).

III. RESULTS

CV, PSD2, HR, IH, ILE, maxFM, rr and MSE for the time shifting 5 and 6 didn't show significantly differences varying the sampling frequency.

SD, sLE, det, avg, max, div and MSE for time shifting varying between 1 and 4 shown significantly differences varying the sampling frequency.

NI, IV and PSD1 shown significantly differences only for the sampling frequency at 32 Hz.

IV. CONCLUSION

In according to this preliminary study the reduction of sampling frequency splits the indexes in three different groups:

- Indexes affected by under-sampling (NI, IV, PSD1, SD, sLE and RQA)
- Indexes affected by under-sampling depending on the time shift use in their computation (MSE)
- Indexes not affected by under-sampling (CV, PSD2, HR, IH, ILE, maxFM and rr)

Indexes that belong to the two groups are those that, to the current knowledge of the authors, show the highest correlation with the clinical rating scales and provide indication of the subject specific factors leading to fall risk.

In conclusion is possible to affirm that the influence of the sampling frequencies in the computation of the stability and variability indexes is not an obstacle to move the assessment and monitoring of fall risk from the laboratory to a portable device.

REFERENCES

- [1] D Hamacher, N Singh, JH Van Dieën et al. (2011) Kinematic measures for assessing gait stability in elderly individuals: a systematic review. *J R Soc Interface* 8(65), 1682-1698.
- [2] Z.Sawacha, E Carraro, P Contessa et al. (2013) Relationship between clinical and instrumental balance assessments in chronic post-stroke hemiparesis subjects. *J Neuroeng Rehabil* 10:95.
- [3] JD O'Sullivan, CM Said, LC Dillon et al. (1998) Gait analysis in patients with Parkinson's disease and motor fluctuations: Influence of levodopa and comparison with other measures of motor function. *Mov Disord* 13(6):900-906.
- [4] S Gillain, E Warzee, F Lekeu et al. (2009) The value of instrumental gait analysis in elderly healthy, MCI or Alzheimer's disease subjects and a comparison with other clinical tests used in single and dual-task conditions. *Ann Phys Rehabil Med* 52(6):453-474.
- [5] G Frazzitta, R Maestri, G Bertotti et al. (2010) Rehabilitation in Parkinson's disease: assessing the outcome using objective metabolic measurements. *Mov Disord* 25(5):609-614.
- [6] F Riva, M Toebe, M Pijnappels et al. (2013) Estimating fall risk with inertial sensors using gait stability measures that do not require step detection. *Gait Posture* 38(2), 170-174.
- [7] F Riva, P Tamburini, et al., Motor stability evaluation in elderly subjects through instrumental stability measures and clinical rating scales. Conference proceeding pag. 36 SIAMOC-ESMAC 2014
- [8] F Riva, P Tamburini, et al., Association between instrumental stability measures of gait and clinical rating scales in stroke patients. Conference proceeding pag. 146 SIAMOC-ESMAC 2014.
- [9] HB Menz, SR Lord, RC Fitzpatrick (2003) Acceleration patterns of the head and pelvis when walking on level and irregular surfaces. *Gait Posture* 18(1):35-46.
- [10] CJC Lamothe, PJ Beek et al (2002) Pelvis-thorax coordination in the transverse plane during gait. *Gait Posture* 16(2):101-114.
- [11] M Costa, C-K Peng, et al. (2003) Multiscale entropy analysis of human gait dynamics. *Physica A* 330(1-2):53-60.
- [12] F Sylos-Labini, A Meli et al. (2012) Recurrence quantification analysis of gait in normal and hypovestibular subjects. *Gait Posture* 35(1):48-55.
- [13] K Aminian, B Najafi et al. (2001) Spatio-temporal parameters of gait measured by an ambulatory system using miniature gyroscopes. *J. Biomech* 35:689-699, 2002.

From thoracic aorta segmentation to geometric parameters quantification: an automatic tool

C. Trentin¹, G.H.W. van Bogerijen^{2,3}, MD, M. Conti¹, E. Faggiano¹, F. Nauta^{2,3}, PhD, J.A. van Herwaarden², MD, PhD, Frans L. Moll², MD, PhD, S. Trimarchi³, MD, PhD, and F. Auricchio¹, PhD

¹Department of Civil Engineering and Architect, CompMech Group, University of Pavia, Italy

²Department of Vascular Surgery, University Medical Center Utrecht, The Netherlands

³Thoracic Aortic Research Center, I.R.C.C.S. Policlinico San Donato, University of Milan, Italy

³ **Thoracic Aortic Research Center, I.R.C.C.S. Policlinico San Donato, University of Milan, Italy Abstract**—The pulsatile aortic changes vary between the different segments, as well as it vary between individual patients. The wide range of change in aortic extensibility during the cardiac cycle may increase the risk for complications after stent graft placement, such as endoleak or graft migration. For this reason it is important to look at pre- and post-operative medical dynamic imaging to analyse thoracic aortic movement differences during the cardiac cycle before and after Thoracic Endovascular Aortic Repair (TEVAR). In order to quantify this movement differences, we attempt to develop an automatic custom software able to segment the thoracic aorta and to extract relevant geometric features.

Keywords—4D CTA, automatic tool, thoracic aorta, geometric quantities.

I. INTRODUCTION

AORTIC arch repair poses a major challenge for surgeon, due to tortuous anatomy and relevant side branches.

Since patients always have comorbidities, they are treated more and more with minimal invasive endovascular technique [6]. In particular thoracic endovascular aortic repair (TEVAR) has significantly changed the preferred treatment choice for acute type B aortic dissection and saccular aneurysms of the descending aorta. Although TEVAR has minor post-operative complications, it fails to represent the tortuous anatomy of the arch and its outcomes depend on aortic biomechanics and specifically on aorta dynamics [1][2]. In fact after deployment of the stent graft, aortic distension should be preserved during the cardiac cycle, which may play an essential role as repeated stress on the stent graft can lead to stent graft fracture or collapse [1][3]. Therefore, the quantitative analysis of pre- and post-operative medical dynamic imaging, to assess thoracic aortic movement differences during the cardiac cycle before and after TEVAR, is becoming relevant [2] [4]. Our research aims at introducing an approach to segment operator-independently the dynamic images and to quantify how the aortic arch relevant geometric quantities change during the cardiac cycle. The basic data input for our investigation is a set of medical images of the aortic arch acquired by 4D Computed Tomography Angiography (CTA).

II. MATERIALS AND METHODS

A. Clinical input data

CTA is a medical imaging technique used to visualize arterial and venous vessels for the evaluation of aortic

diseases. The progress made in Image Diagnostic enabled CT Angiography to be gated with ECG giving the possibility to free images from cardiac pulsation artifacts and therefore allows the reconstruction of aortic segments. Furthermore, ECG gated CT allows 'time-resolved' image visualization, adding a fourth dimension (4D) to this technology [5] [7]. The dynamic CTA scans of the aorta were performed with a 64-row or 256-row multislice CT system (Philips Medical System, Best, The Netherlands). A three-dimensional scan volume was acquired (ECG-gated) at eight equidistance time steps covering the whole heart cycle and providing a 4D data set. For enhanced vessel contrast each patient received between 150 and 90 ml of a nonionic contrast medium (Iopromide, Schering, Berlin, Germany), followed by a 60 ml saline chaser bolus. Our database is composed of eight patients affected by Thoracic Aortic Aneurysm (TAA), two patient with type B aortic dissection (TBAD) and a healthy control case. All of them, exception made for the control case, underwent TEVAR procedure.

B. Image segmentation

In order to perform the measures on the thoracic aorta, we need the 3D patient specific model of the pre- and post-operative geometry of the vessel, which can be reconstructed from the CTA images. The 8 time instances of each patient are transferred to a workstation equipped with dedicated medical image software for visualization, segmentation, and analysis of this 4D data set. Image segmentation is performed with the use of implicit deformable models, they deform under image-based forces and this deformation is described through the level set technique [8]. Since our database is composed of 8 different time-steps, we sought to implement an operator-independent tool to segment it simultaneously. We modified the initialization technique tailored on the specific aortic anatomy and we passed the initial level sets image of the first time instant to the others, obtaining the 3D models for each set of images.

C. Quantitative analysis of 3D aortic geometry

Given the 3D aortic lumen in, a script in Python, an interpreted high-level programming language, is used to perform a semi-automated geometric feature extraction. The script uses also library such as VTK- Visualization Toolkit and VMTK-Vascular Modeling Toolkit [8] to perform visualization and processing of the 3D aortic arch reconstruction, through a well-defined procedure. Computation of the vessel centerline is reasonable approach exploiting the tubular shape of the vessels to synthetically

describe the geometry. The centerline as descriptor of the vasculature can be easily characterized geometrically with the following quantities: curvature, torsion and tortuosity. Moreover aortic arch length L and its subdivision into the segments $L1$, $L2$ and $L3$ (fig. 1, 2), centerlines key sections, and their relative area, minimum and maximum diameter can be computed.

III. RESULTS

We have mainly tried to develop a tool to improve segmentation of the aortic arch for the target dataset (4D CTA). We focused on reducing elaboration time, inter- and intra-observer variability making also more robust the method for extracting the geometric quantities. We retrieve in aortic area changes a pressure-like pattern (fig. 3) and focusing on the entire aortic arch length L we found that the elongation of the thoracic aorta remains preserved also after TEVAR (Table 1). Furthermore, from the analysis of $L1$, $L2$ extensibility, we can observe that it increases at the post-operative phase compared to the pre-operative phase. This result implicates that $L1$ and $L2$ need to compensate the increased stiffness produced by the stent graft in $L3$. We can add also that $L2$ is extending more than $L1$ for both the pre- and post-operative phase. To conclude we notice that $L3$ is losing extensibility in the post-operative phase. In fact due to the implant stent graft the section $L3$ becomes stiffer.

TABLE I

Patient	L pre-op [mm]	L post-op [mm]
1	360,7	358,3
2	385,9	388,8
3	406,8	418,8
4	428,6	427,9
5	373,4	393,4
6	383,7	385,5
7	356,3	372,1
8	368,8	377,3
9	356,2	

Length of centerline from the sino-tubular junction to the celiac bifurcation in millimeter pre- and post-operatively for 9 patients. Patient 1 and 2 present TBAD, patients 3 to 8 presented TAA, patient 9 is the control case. All the measures are expressed as mean value of the length through the entire heart cycle.

IV. CONCLUSION

From a clinical point of view, we can conclude that the section of the stent graft becomes stiffer and the proximal section compensates through the increased extensibility in this section. The increased extensibility in the section proximal to the stent graft may explain the major feared complication after TEVAR: retrograde type A dissection. It will be essential to define which section of $L2$ and $L3$ is covered by stent graft to be able to explain and verify the results.

ACKNOWLEDGEMENT

The work is supported by a ministerial grant. M. Conti is partially supported by ERC Starting Grant through the Project ISOBIO: Isogeometric Methods for Biomechanics (No. 259229). The authors would like to acknowledge medical doctors of I.R.C.C.S. San Donato, Milan, Italy and of University Medical Center Utrecht for their support.

REFERENCES

- [1] Muhs BE, et al. Dynamic cine-CT angiography for the evaluation of the thoracic aorta; insight in dynamic changes with implications for thoracic endograft treatment. *Eur J Vasc Endovasc Surg* 2006 Nov; 32(5):532-6.
- [2] van Keulen JW, et al. Dynamics of the aorta before and after endovascular aneurysm repair: a systematic review. *Eur J Vasc Endovasc Surg* 2009 Nov; 38(5):586-96.
- [3] van Prehn J, et al. Toward endografting of the ascending aorta: insight into dynamics using dynamic cine-CTA. *J Endovasc Ther* 2007 Aug; 14(4):551-60.
- [4] van Prehn J, et al. Aortic pulsatile distention in young healthy volunteers is asymmetric: analysis with ECG-gated MRI. *Eur J Vasc Endovasc Surg* 2009 Feb; 37(2):168-74.
- [5] Weber TF, et al. Assessment of thoracic aortic conformational changes by four-dimensional computed tomography angiography in patients with chronic aortic dissection type b. *Eur Radiol* 2009; 19: 245-253.
- [6] F. Auricchio, et al. Patient-specific aortic endografting simulation: From diagnosis to prediction, *Comput. Biol. Med.* (2013). Available: <http://dx.doi.org/10.1016/j.compbiomed.2013.01.006>
- [7] Fleischmann D, Miller DC. Clinical 3D and 4D Imaging of the Thoracic Aorta. *Diseases of the Heart, Chest & Breast* 2007; 119-130.
- [8] Piccinelli M, et al. Framework for Geometric Analysis of Vascular Structures: Application to Cerebral Aneurysms. *IEEE Transactions on Medical Imaging*, Vol. 28, No. 8, august 2009.

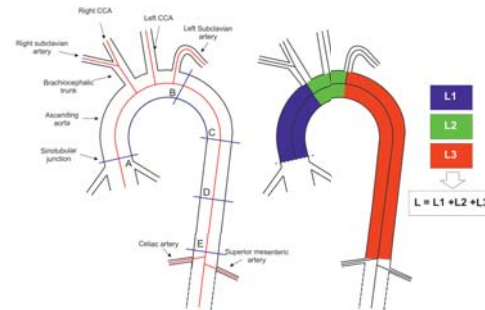


Figure 1: Illustration of the vascular anatomy classification of the aorta. On the left the different main aortic regions are indicated while on the right the subdivision of the aorta performed by the branch splitting algorithm.

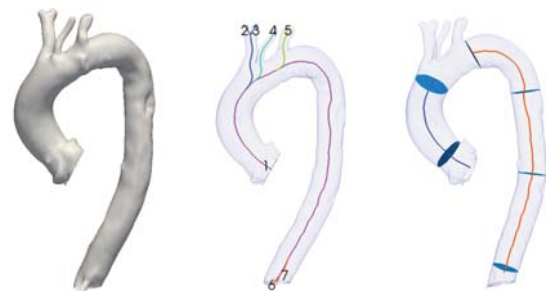


Figure 2: 3D model of the thoracic aorta, from left to right: 3D model of thoracic aorta, 3D model (opaque) with centerlines, one for every vessel, 3D model (opaque) with depicted centerlines and sections automatically extracted and subsequently geometrically characterized.

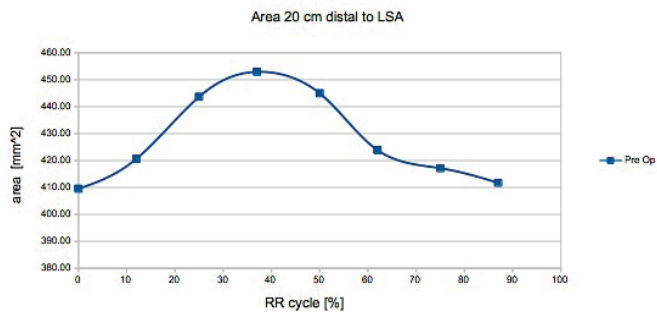


Figure 3: Example of area changes [mm²] through the entire heart cycle. Note how the pressure-like pattern is visible and how the maximum value of the curve is placed around 37.5/50% of the RR cycle, related to the systolic phase.

In vitro tests of human femur before and after total hip arthroplasty with finite element analysis

X. Zou¹, M. Conti¹, S. Morganti¹, F. Sbaiz² and F. Auricchio¹

¹ Department of Civil Engineering and Architecture, University of Pavia, 27100 Pavia, Italy

² Limacorporate S.p.a. Via Nazionale n. 52, 33038 Villanova di San Daniele del Friuli, Udine, Italy.

Abstract—Total hip arthroplasty (THA) is the common surgery for diseases of the hip joint which conventional therapy achieves poor effect. The goal of this study is to evaluate the impact of the implanted hip prosthesis on the mechanical response of the femur both experimentally and numerically. Two ex vivo human femoral samples have been loaded through uniaxial compressive tests without and with prosthesis at normal stance position. After the tests, computed tomography (CT) has been performed for the femora. Then segmentation of the CT images has been made and finite element (FE) meshes have been generated for each femur model. The material properties of the femur bone have been determined by a posteriori calibration with experiment results of the intact femora, and later used for the femora with prosthesis. Having implemented the FE analysis, the results of strains at the strain gauges have been extracted and compared with results from the tests. The comparison showed fairly good agreements for the trends of strains, and clearly certifies that the implanted prosthesis significantly reduces strains on the shaft of femur.

Keywords—Total hip arthroplasty, human femur, in vitro test, finite element analysis.

I. INTRODUCTION

THE femur is the largest, longest and strongest human bone in the anatomical point of view. Taking physiologic loads as heavy as 30 times of the body weight, it is also one of the most vulnerable bone in the musculoskeletal system. Total hip arthroplasty (THA) [1] is a common surgery with excision of the head and proximal neck of the femur and removal of the acetabular cartilage and subchondral bone. In biomechanics, a reasonable mechanical analysis of femur (both cadaveric and synthetic) is important to surgeries and clinics involving THA.

The finite element analysis (FEA) method is proved an efficient and effective supplement of in vitro biomechanical tests. Many researches works on human proximal femur analysis with both experiments and FE simulations such as [2].

Comparing with the bone density assessment, quantitative computerized tomography (QCT) scan-based FE models can achieve equal precision and can better predict fracture load [3]-[5]. The QCT/FEA process has become the main stream of proximal femur stiffness and strength assessment.

Many works focus on the comparison between simulation results and experiment results such as [6]-[8]. We are more interested in some similar works focusing on the comparison of the mechanical behaviour of the femur without/with prosthesis such as [9].

The objective of this study is to evaluate the impact of implanted prosthesis to the shaft of femur. In addition, the feasibility of the extension on FE models from intact femora to femora implanted with a prosthesis is also verified by comparing the strain results from simulation and experiment.

II. MATERIALS AND METHODS

A. In vitro experiments

The in vitro test set-up, depicted in Figure I, aims at reproducing the loading conditions of heeling during averaged simplified gait cycle, i.e., no muscles are considered. The inferior constraint of the sample has to preserve the support given by the patellar surface. The sample was constrained in the inferior side within a nylon cup, partially filled with resin. The data of samples and the maximum applied load F_{max} are listed in Table I. F_{max} is loaded in stance position.

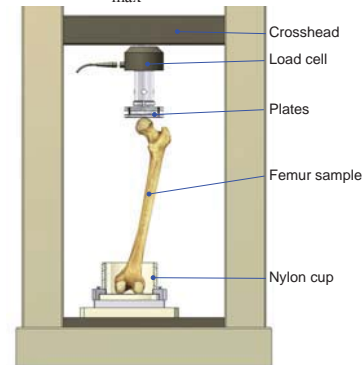


FIGURE I
SETTINGS OF THE IN VITRO EXPERIMENT

TABLE I
SAMPLE DATA AND MAXIMUM APPLIED LOAD

Femur	Length	Height	BMI ^a	BW	F_{max}
2	508 mm	1 834 mm	31	104 kg	2 550 N
3	483 mm	1 734 mm	38	114 kg	2 800 N

BMI = BW / Height², BW: Body Weight, BMI: Body Mass Index

Three main steps of the load history are: 1) a preload from 0 to 50 N with a speed of 0.5 mm/min; 2) 100 cycles of dynamic load from $0.25F_{max}$ to $0.75F_{max}$ with a speed of 1 mm/min; 3) a quasi static load from $0.25F_{max}$ to F_{max} with a speed of 0.5 mm/min.

To measure the strains, 12 strain gauges were bonded to 2 horizontal sections with totally 6 locations on each femur, and oriented in the longitudinal and circumferential direction respectively. See Figure II for the locations. The longitudinal and circumferential strain results were acquired in separated tests due to the limits of the device.

B. Finite element models

Triangular surface meshes were generated by QCT image segmentation, and were remeshed to obtain proper size and quality. Tetrahedral meshes were converted from the triangular meshes. Each FE model was fixed at the distal end and loaded at the head of femur or prosthesis. Local

cylindrical coordinate systems were established for each section to extract the circumferential strains.

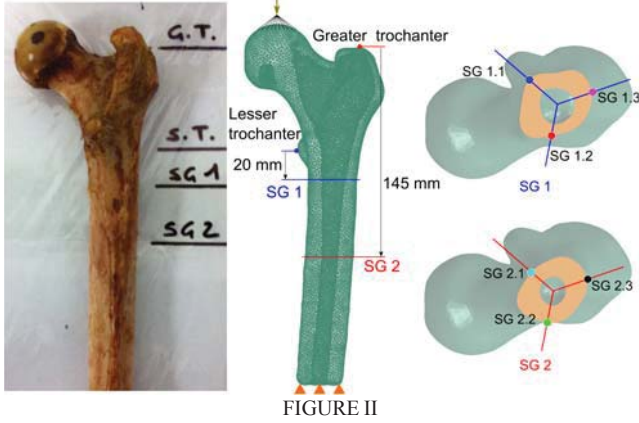


FIGURE II
FEMUR SAMPLE & FE MODEL WITH SLICED VIEW & STRAIN GAUGE POSITIONS.

For femora with prosthesis, the interaction between the prosthesis and femur is simplified by using tie constraints. The FE model with prosthesis is shown in Figure III.

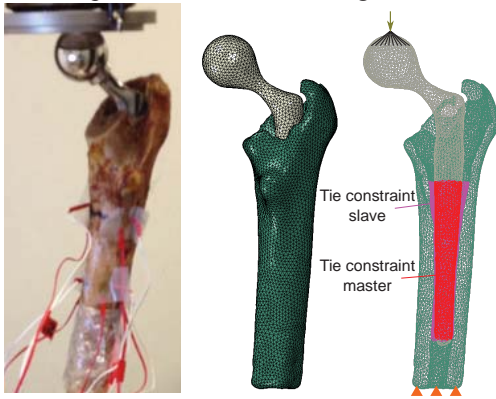


FIGURE III
FE MODEL OF FEMUR WITH PROSTHESIS & SLICED VIEW. MASTER SURFACE (RED) & SLAVE SURFACE (PURPLE) OF TIE CONSTRAINT ALSO ILLUSTRATED.

C. Calibration of material properties

With the isotropic and homogeneous assumption, the exact Young's Modulus E of the bone was unknown. For the intact femora, due to the linearity of the FE model, a preliminary analysis had been performed *a priori* with a presumed Young's Modulus $E_0 = 20$ GPa. Then, E was calibrated by comparing preliminary strain results with experimental strain results.

The calibrated results for the femora are listed in Table II. The material properties of the bone were set accordingly in the FEA. Although this calibration is only valid for the intact femur model, it is still reasonable to use the resultant modulus for the model with prosthesis. The Poisson's Ratio was set as $\nu = 0.3$. For the prosthesis, its Young's Modulus was 200 GPa.

TABLE II

RESULTS OF CALIBRATION FOR YOUNG'S MODULUS		
Femur	E_0	E
2	20 GPa	13.64 GPa
3	20 GPa	13.92 GPa

III. RESULTS AND ANALYSIS

The obtained load-strains results at the strain gauges in both experiment and simulation for Femur 2 are plotted in Figure

IV. Fairly good agreements are demonstrated.

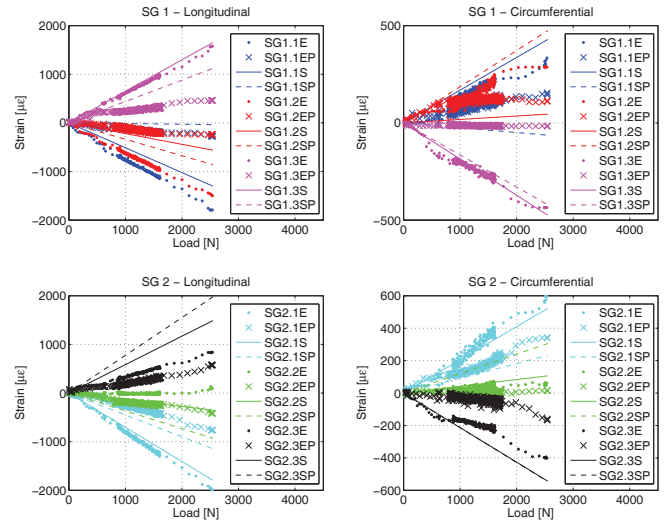


FIGURE IV
PLOT OF EXPERIMENT (E) AND SIMULATION (S) LOAD-STRAIN RESULTS FOR FEMUR 2 BOTH BEFORE AND AFTER (P) THA

Comparing experiment and the simulation results, better agreements achieve before THA. After THA, SG2 obtains better agreements than SG1, because SG1 locates more close to the upper end of the clipped femur, thus suffers more influence from stress shielding. It is clearly demonstrated that after THA the strains have significantly reduced while the tensile/compressive trends remain the same.

ACKNOWLEDGEMENT

The authors would like to acknowledge the collaborative work of the following partner:

Clinica Ortopedica e Traumatologia, University of Pavia, IRCCS San Matteo Hospital, 27100 Pavia, Italy.

REFERENCES

- [1] J. S. Siopack, and H. E. Jergesen, "Total hip arthroplasty," in *The Western Journal of Medicine*, 162(3):243-249, 1995.
- [2] R. Nareliya and V. Kumar, "Biomechanical Analysis of Human Femur: A Review," in *Journal of Biomedical and Bioengineering*, 3(1):67-70, 2012.
- [3] J. H. Keyak, S. A. Rossi, K. A. Jones, and H. B. Skinner, "Prediction of femoral fracture load using automated finite element modeling," in *Journal of Biomechanics*, 31(2):125-133, May 1997.
- [4] M. Bessho, I. Ohnishi, J. Matsuyama, T. Matsumoto, K. Imai, *et al*, "Prediction of strength and strain of the proximal femur by a CT-based finite element method," in *Journal of biomechanics*, 40(8):1745-1753, January 2007.
- [5] E. Dall'Ara, B. Luisier, R. Schmidt, F. Kainberger, P. Zysset, *et al*, "A nonlinear QCT-based finite element model validation study for the human femur tested in two configurations in vitro," in *Bone*, 52(1):27-38, January 2013.
- [6] Z. Yosibash, R. P. Mayo, G. Dahan, N. Trabelsi, G. Amir, *et al*, "Predicting the stiffness and strength of human femurs with real metastatic tumors," in *Bone*, 69(0):180-190, 2014.
- [7] M. Papini, R. Zdero, E. H. Schemitsch, and P. Zalzal, "The biomechanics of human femurs in axial and torsional loading: comparison of finite element analysis, human cadaveric femurs, and synthetic femurs," in *Journal of biomechanical engineering*, 129(1):12-19, February 2007.
- [8] B. Helgason, F. Taddei, H. Pålsson, E. Schileo, L. Cristofolini, *et al*, "A modified method for assigning material properties to FE models of bones," in *Medical engineering & physics*, 30(4):444-453, May 2008.
- [9] Z. Yosibash, A. Katz, and C. Milgrom, "Toward verified and validated FE simulations of a femur with a cemented hip prosthesis," in *Medical Engineering & Physics*, 35(7):978-987, 2013.